3-2022

# Verficiation and Validation of Unstructured Meshing Capabilities in MCNP6

Micah C. Jeroutek


# VERIFICATION AND VALIDATION OF UNSTRUCTURED MESHING CAPABILITIES IN MCNP6

THESIS

Micah C Jeroutek

AFIT-ENP-MS-22-M-097

**DEPARTMENT OF THE AIR FORCE**
**AIR UNIVERSITY**

***AIR FORCE INSTITUTE OF TECHNOLOGY***

**Wright-Patterson Air Force Base, Ohio**

AFIT-ENP-MS-22-M-097

# VERIFICATION AND VALIDATION OF UNSTRUCTURED MESHING CAPABILITIES IN MCNP6

THESIS

Presented to the Faculty

Department of Engineering Physics

Graduate School of Engineering and Management

Air Force Institute of Technology

Air University

Air Education and Training Command

in Partial Fulfillment of the Requirements for the

Degree of Master of Science in Nuclear Engineering

Micah C Jeroutek, B.S.N.E.

March 24, 2022

AFIT-ENP-MS-22-M-097

# VERIFICATION AND VALIDATION OF UNSTRUCTURED MESHING CAPABILITIES IN MCNP6

THESIS

Micah C Jeroutek, B.S.N.E.

Committee Membership:

Darren E Holland, Ph.D
Chair

Jerawan C Armstrong, Ph.D
Member

Karen C Kelley, Ph.D
Member

Maj. James E Bevins, Ph.D
Member

# Abstract

In the Monte Carlo N-Particle Transport Code (MCNP), a general-purpose radiation transport code developed by Los Alamos National Laboratory, problems have historically been modeled using constructive solid geometries (CSGs). While CSGs work well for modeling simple geometries, they can be difficult and time-consuming to use when modeling complicated geometry systems. To combat this issue, the code's development team introduced unstructured mesh (UM) capabilities with the release of MCNP6.

During initial testing, it was found that UM model results matched with that of CSG models for simple geometry systems. While CSGs are well-tested and documented for many different problem types and applications with many publicly available benchmarks, the same cannot be said for their UM counterparts. As such, verification and validation of UMs in MCNP must be conducted to assist in their further code development to increase user confidence in the UM capability. Currently, the MCNP test suite is lacking in UM benchmarks, and of the few that are present, their range in problem type is limited.

To address these issues, two preliminary test cases covering new applications of UMs were developed for future inclusion in the test suite. The first was a test case based on the ATHENA-I experiment, which involved the study of electronic devices' responses to neutron environments. For this case, agreement was found between CSG and UM models as well as experimental data using a two-sample Kolmogorov-Smirnov test that returned p-values of nearly 1 for every tally result. The second case involved modeling photon shielding capabilities for a deformed copper plate. While CSGs could not handle its geometric complexity, it was able to be modeled with UMs with

and without deformation-induced density variation. While the model results did not completely agree with the experimental data, a solid foundation was established for this test case to be elaborated upon. Through the procedures and results for both of these test cases, a repeatable methodology by which the UM functionality of MCNP6 can be continuously verified and validated across all future version releases of the code was developed. This methodology should serve as an expansion to preexisting UM benchmark development methods as well as a foundation for further exploration of the UM capabilities in MCNP across many new radiation transport applications beyond the current scope of the test suite.

# Acknowledgements

I would first like to thank my advisor Dr. Darren Holland for his invaluable guidance and patience with me throughout my research. Likewise, to the rest of my thesis committee members, Maj. James Bevins, Dr. Jerawan Armstrong, and Dr. Karen Kelley for helping me not only with my research, but also with my job search for after graduation. I could not have asked for a better advisor or committee.

Next, I would like to thank Maj. Ryan Kemnitz and Mike Ranft from the ENY Department for their assistance and guidance on deforming copper plates for my research. Next, to Brian Crabtree and the rest of the team at the AFIT Model Shop for their assistance in manufacturing my custom indenters and a detector raster assembly. Also, to Dr. Abigail Bickley, Connor Gautam, Capt. Brian Frandsen, and Ben Doane for helping me complete my radiation safety training and develop my experimental setup for the latter half of my research.

Finally, I would like to thank my fiancée and family for being such an amazing support system. Words cannot express my gratitude for all of the motivation and encouragement they have provided me.

Micah C Jeroutek

# Table of Contents

Page

# List of Figures

# List of Tables

VERIFICATION AND VALIDATION OF UNSTRUCTURED MESHING CAPABILITIES IN MCNP6

# I. Introduction

With each production code comes certain assumptions and limitations that users must understand in order to use the code to its fullest potential. Beyond having an awareness of these assumptions and limitations, however, users must also be able to trust that a code functions properly. To maintain this user confidence, codes must be thoroughly tested over the course of their development by way of verification and validation (V&V). This process is essential for ensuring that codes function properly as they develop and that they adequately meet the needs of their user bases.

In the case of the Monte Carlo N-Particle Transport Code (MCNP) [1], a general-purpose radiation transport code developed by Los Alamos National Laboratory (LANL), V&V ensures that with each version release, legacy content still functions properly and all new additions to the code are developed with the same level of fidelity and are able to accurately capture the intended physics of interest in their simulations. One such addition to MCNP that is currently in need of V&V is its ability to use unstructured mesh (UM) geometries in its radiation transport simulations. Inspired by finite element analysis (FEA) tools and methods, these geometries serve as an alternative to the historically used constructive solid geometries (CSGs) [2]. While using CSGs to model complex and nonstandard geometries can be difficult or even impossible, UMs do not struggle with the same geometric limitations. Despite this, UMs introduce several other limitations of their own. MCNP was originally developed in 1977, but the MCNP UM feature was developed in 2006; thus, the UM

capability does not have a long history of V&V. During initial testing of these new capabilities, it was found that results from UM models did not entirely align with the results of corresponding CSG models for some test problems.

In order to properly model radiation transport for increasingly complex geometries, fully functional UMs capabilities are needed in MCNP. To reach this goal and bridge the gap between UMs and CSGs, thorough V&V must be conducted across various problem types to add sufficient robustness to the current MCNP test suite. As it currently stands, the test suite is fairly sparse and will need many more parameter studies, test cases, and benchmarks. Without further V&V efforts and development of the test suite, UMs can never properly serve as replacements or alternatives for the legacy CSGs in MCNP models, and progress cannot be made towards accurately modeling problems of interest within the MCNP user community.

# II. Background and Literature Review

## 2.1 Preamble

This chapter seeks to provide insight into the fundamental differences between CSG and UM models in MCNP in order to illustrate the sources of discrepancies observed in previous V&V efforts. Beyond analyzing these differences, however, this chapter also serves to highlight the process of benchmarking UM models in the MCNP test suite. This review demonstrates the breadth of problem types spanned by the current test suite and provide general guidelines for future UM V&V analyses. Additionally, possible additions to this suite will be discussed based on several non-benchmark applications of UMs from various different industries and communities of MCNP users.

## 2.2 Background

In order to understand the V&V process for UM capabilities in MCNP, it is first important to understand what V&V means in a more general sense. While the two terms are often mistakenly used synonymously, they actually describe two separate, but complementary processes. Regarding computational modeling specifically, verification refers to whether or not models are built correctly while validation refers to whether or not the models are built for the correct purpose [3]. When this terminology is applied to UM models in MCNP, verification refers to comparisons between the simulated results of CSGs and UMs to determine how comparable they are. Furthermore, validation would refer to comparisons with empirical data to show that UM model results are physically realistic and accurate.

V&V efforts with multiple models and experimental data respectively are necessary to develop benchmarks. Generally speaking, a benchmark is intended to establish

an extensive base of knowledge with regards to a tool or model's performance so that others may further apply and/or optimize that tool or model [4]. Given that it is meant to serve as a starting point for others, it is important to make sure that the experiment involved in the validation portion is replicable. When benchmarking, it is also important to consider what resources go into the associated computational model(s) for the verification portion. In order to ensure replicability for computational models in addition to the experiment, the usage of computational resources (e.g., processing time, memory consumption) should be tailored to accommodate modeling on as many different machines as possible [5].

Another vital piece to understanding UM V&V is the nuances of meshing and how they are used with regards to MCNP. Generally speaking, meshes represent the discretization of geometries into elements, which can be further broken down into vertices, or nodes [6]. In a 2D mesh, an element corresponds to an area contained within a set of nodes, while in a 3D mesh, an element would instead be a volume. Volumetric elements can take on many shapes with various numbers and patterns of nodes, and given that MCNP is a 3D radiation transport code, it can only interpret meshes with tetrahedral (TET), pentahedral (PENT), or hexahedral (HEX) elements [7]. These classifications correspond to elements with four, five, and six faces respectively. If they are first-order, TET, PENT, and HEX elements are comprised of four nodes, six nodes, and eight nodes respectively with a linear interpolation scheme for the edges between them [8]. Second-order elements, on the other hand, feature extra nodes along each of an element's edges and a quadratic interpolation scheme; thus, a second-order TET element would be made up of 10 nodes, a second-order PENT element would be made up of 15 nodes, and a second-order HEX element would be made up of 20 nodes.

As a whole, meshes can be divided into two categories: structured and unstruc-

tured. While structured meshes feature orthogonal elements with implicit connectivity, unstructured meshes make use of arbitrarily sized elements which have to have their connectivity explicitly defined and stored [6]. UMs also find more use when meshing geometries that require certain regions to be more finely discretized than others for subsequent analyses. With this in mind, it is understandable that UMs were adapted from FEA tools to improve and expand upon geometry definition within MCNP as well as enable multi-physics coupling.

For UMs in this work, the process of creating and processing UMs is not handled entirely within MCNP. Separate software such as Abaqus/CAE [9] or CUBIT [10] is required to generate and export meshes in a specific format so that they may be embedded within an input deck and read properly by MCNP [7]. In versions leading up to the most recent development version of MCNP, UMs could only be embedded as Abaqus input decks [11]. These Abaqus inputs require meshed blocks or parts to correspond to their own separately defined materials so that they may be linked to cell cards within MCNP. In addition to Abaqus input decks, the most recent version of MCNP UMs introduced the ability to embed UM geometries in MCNP input decks as HDF5 files. Regardless of file type, however, the MCNP cells that correspond to parts or materials of UMs are always referred to as inferred cells or pseudo cells. In both pure UM models and hybrid geometry models comprised of CSG and UM regions, pseudo cells, along with an inferred background cell, are all contained within a mesh universe that is subsequently applied to a CSG fill cell.

With these details of V&V and unstructured meshing in MCNP in mind, the next step in the V&V process involves the combination of these two elements to establish benchmarks and test cases for the MCNP test suite. While there are several benchmarks that are currently available in the test suite, more must be developed to accommodate a wider range of problem types and the interests of the MCNP user base.

As it stands, the test suite features many CSG models that could be readily adapted into UM models as part of an initial verification effort, but the vast majority of these models are only intended to test how quickly MCNP can process different data cards rather than to produce well-converged, physically realistic results [12, 7]. In order to establish more physically accurate models within the test suite and validate UM capabilities in MCNP as a whole, new UMs need to be constructed in correspondence to experimental data. Assuming the experiments are geometrically simple enough to model with CSGs as well, the UMs could also be verified and subsequently, new benchmarks could be established within the MCNP V&V test suite.

Ideally, the test cases and benchmarks found within this test suite should span a broad range of radiation transport problems to accommodate as much of MCNP's vast user base as possible and inform future developments of the UM capabilities. With more benchmarks and problem diversity, the V&V test suite could instill user confidence in MCNP's UM capabilities around the world and promote progressively more advanced applications of it down the line. In order to catalyze the creation of new benchmarks and test cases to achieve these goals for the test suite, a systematic methodology detailing the process of MCNP UM V&V should be established.

### 2.3 Processing of UMs in MCNP6

To properly quantitatively and qualitatively evaluate the differences in CSG and UM models, it is important to understand the fundamental differences in how MCNP6 treats UMs as opposed to CSGs. One of the biggest differences lies in how user inputs are handled. Unlike CSGs, UMs make use of pseudo cells which exist in mesh universes, do not reference any surface cards, and cannot be filled by other universes or lattices [7]. These mesh universes are the same as any other MCNP universe with the exception that they are filled with UM geometries rather than CSGs. Given the

flexibility of the universe and lattice fill features, MCNP6 determines whether or not a cell is a pseudo cell entirely based on the presence of a null surface entry on the corresponding cell card.

Many of the other differences between CSG and UM input decks primarily fall under the category of data cards. The foremost addition to the data cards is the EMBED card which handles filling mesh universes with pseudo cells [7]. This card also handles the inferred background that accounts for everything not found within pseudo cells in the mesh universe through its BACKGROUND argument. This background also includes gaps found in the embedded mesh. In addition to specifying the inferred background cell, the EMBED card requires that the type of mesh (typically, an Abaqus input deck) and its name be entered using MESHGEO and MGEOIN respectively. While most other cards in MCNP are not case-sensitive, this MGEOIN argument requires that UM filenames must be entirely lowercase. Once this mesh file is embedded, the EMBED card will also handle the material-cell linking between the materials present in the mesh file and the pseudo cells in the MCNP input deck through the MATCELL argument.

While these four arguments are the only ones that must be explicitly stated for the EMBED card, several other optional arguments may be used as well. The FILETYPE argument refers to the type of file that the Elemental Edit Output (EEOUT) will be written as (defaults to ASCII but can also be binary) [7]. An EEOUT is a file in which results from the simulated transport through the mesh are returned alongside a description of the mesh. Other arguments to the EMBED card that involve EEOUTs are the MEEOUT card, which is used to name the EEOUT file and the MEEIN which is used during continued runs to read in the EEOUT from the initial runs. Another optional argument of EMBED is LENGTH, which ensures a multiplicative conversion of the mesh's dimensions to centimeters. The default key value

for LENGTH is 1, which assumes that the arbitrary units used to mesh a geometry were already considered centimeters. Finally, the OVERLAP argument calls several different models for particle treatment in regions of overlapping pseudo cells which can be referenced altogether or individually. The default treatment for OVERLAP is to use results from the cell in the overlapping region that it exits, but a preference can also be given to the cell in the overlapping region the particle enters through or the results can simply be averaged between the two.

While the EMBED card is fundamental to running UM model inputs, several other optional data cards are typically used alongside them to evaluate UM models. One such card is the EMBEE card which simulates volumetric flux or energy deposition edits (essentially tallies for UMs) for any specified particle type within the mesh universe [7]. The edits provided by the EMBEE card can be binned across multiple energy groups and multiplied with the EMBEB and EMBEM cards respectively. The same binning and multiplication can be done for the EMBEE card(s) over time rather than energy using the EMBTB and EMBTM cards. When evaluating dose response in mesh universes, EMBDE and EMBDF can be used to bin according to dose energy and apply dose function multipliers respectively. All of the edit results corresponding to each of these data card inputs can be found in the EEOUT file associated with the input deck.

Several other key differences between how the MCNP code handles CSG and UM models exist beyond the formatting of input decks. One major difference lies specifically in the particle-tracking methods employed by MCNP. Historically, MCNP has employed ray-tracing to track particles through geometries from their creation to their end [13]. In CSG cells, particles are transported based on their starting positions, energies, and directions. The code looks for an enclosing surface to the cell for the particles to exit through, and if they can make it to that exit without any collisions,

the particles will pass through to an adjacent cell. At every sample taken throughout this transport, the particles' starting positions, energies, directions, and cell numbers are updated accordingly. This tracking routine is known as Immediate Mode Tracking (IMT). There are caveats to this particle tracking method once particles travel into the mesh universe, however.

Particle tracking in UM geometries has changed over the iterations of MCNP6's releases, but it initially used the IMT routine just as was done for CSG models except for the fact that it subdivided tracking through individual mesh elements rather than through whole cells [13]. Due to the fact that MCNP6 allows for gaps and overlaps in UM geometries, however, IMT cannot be used alone to track particles in mesh universes. Thus, the Revised Extended Grid Library (REGL) algorithms and Look-Ahead Tracking (LAT) routines were implemented by developers in the more recent iterations of MCNP6 [14].

These particle tracking routines vary depending on the current particle's location within the mesh universe. If the particle is in the inferred background, the REGL hit-mesh algorithm determines whether the particle is moving towards or away from the UM geometry [15]. If the particle is headed away from the mesh, IMT is used to find the next cell along its path. Otherwise, if the particle is headed towards the mesh, the REGL hit-mesh method is employed to determine the pseudo cell and element within that pseudo cell that the particle will move into.

Once a particle is within a pseudo cell and not the inferred background, the REGL find-element method is instead used to find the current element that the particle is in and initialize tracking using both IMT and LAT [15, 13]. MCNP then samples the current position and direction to compute the distance to the next element and the total tracking distance from the position where the particle entered the current pseudo cell. If the particle succeeds in moving to the next pseudo cell, this process

is repeated. If the distance between element faces is too small ($10^{-6}$ cm) or the next element cannot be found, MCNP must use LAT which will analyze the current particle path and refer to the global UM model information to develop several possible paths for the particle to take through the mesh. If the next cell cannot be determined with LAT, MCNP deduces that the particle is in the inferred background and begins to use the aforementioned background tracking routines (IMT or REGL hit-mesh). See Fig. 1 for an illustration of the particle tracking methods used in UM models.

It is important to note that the use of LAT is not reserved for just pseudo cell boundaries, but rather throughout elements inside of pseudo cells [15]. When using IMT to find the particle's next element, the code searches for the current element's nearest neighbor. In meshes, neighbors are defined by nodal connectivities between elements. For example, two first-order TET elements would be considered neighbors if they share three nodes.

To test these new tracking algorithms and routines, they were applied to several benchmarks within the MCNP Test Suite by the developers at LANL.

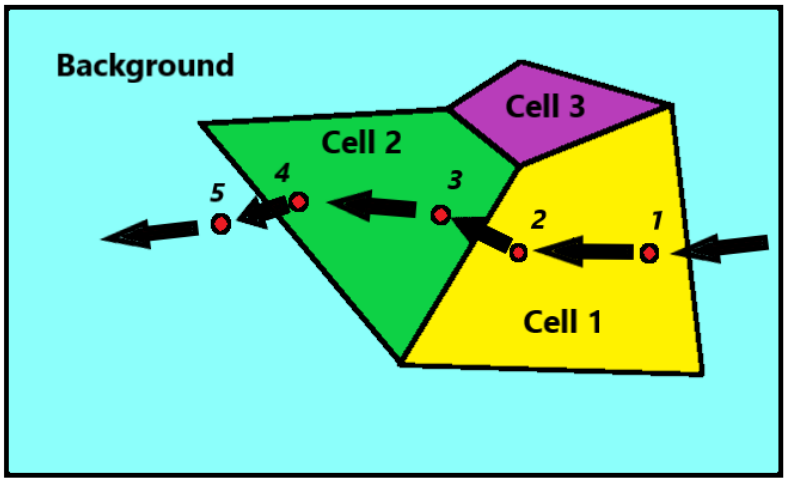


Figure 1: Visualization of the particle tracking methods used for UM geometries in MCNP6. The steps are as follows: (1) IMT is used to track the particle through the majority of the pseudo cell; (2) the particle has gotten close enough to the boundary of Cell 1 for MCNP to activate LAT; (3) MCNP checks to see whether the particle is in a cell or the background, finds it in Cell 2 and begins to track the particle with IMT once again; (4) the particle approaches the boundary of Cell 2 and LAT is activated; and (5) MCNP searches the mesh cells to determine the next element, finds that the current position is in the background cell, and uses the REGL hit-mesh method to determine the next position.

### 2.4 Benchmarks in the Current MCNP Test Suite

The current state of the MCNP test suite is fairly sparse. Many test cases (those found in the regression suite specifically) represent problems with simple geometries that are only intended to ensure that MCNP6 is running properly after installation. Aside from these regression cases, most of the benchmarks in the test suite are criticality-based models with a select few others falling under other categories of particle transport problems [12]. Several CSG problems have been taken from pre-existing MCNP benchmarks and converted to UM models, but these UM model test problems have not been publicly released.

### 2.4.1 Criticality Benchmarks

One of the most basic benchmark models regarding criticality is the HEU-MET-FAST-001, or Godiva benchmark [16]. The Godiva model represents a highly-enriched uranium sphere with a radius of 8.7407 cm and a density of 18.74 g/cm$^3$ in which k-effective was calculated using the KCODE feature of the MCNP code. This model was chosen specifically given its simplicity and curved surfaces, which could pose a challenge to MCNP6's UM capabilities at the time [17]. Both the CSG and UM inputs tracked neutrons and photons across a series of 1000 cycles with 100 of those being inactive. Several variations of the UM input were created to test the efficiency of multiple mesh element types including both first- and second-order elements of both TET and HEX varieties. While both inputs were able to converge to a value of k-effective near unity (see Table 1), the speed at which they did so differed greatly depending on how many elements were used. At lower element counts, the CSG was faster than the UM model, but as the element count reached approximately $10^4$, the UM overtook the CSG.

Another criticality benchmark featured in the test suite is the IEU-MET-FAST-007, or Big Ten model. This benchmark corresponds to an experiment conducted at the Los Alamos Critical Experiment Facility (LACEF) in which a critical assembly made with approximately ten metric tons of 10% enriched $^{235}$U was used to evaluate effective neutron cross sections [18]. In the context of meshing, this model geometry is much more complex than the aforementioned Godiva benchmark and as such, served as a greater challenge to MCNP's UM features. The UM Big Ten model makes use of first-order TET elements created using Attila4MC [19]. Both the CSG and UM inputs track neutrons and run KCODE simulations [18]. When run, the UM model resulted in a k-effective value of 1.0041 $\pm$ 0.00008. This matched well with both the CSG model and experimental results which yielded k-effective values of 1.00432 $\pm$

0.00007 and 1.0046 ± 0.0002, respectively.

In addition to these two models, several other preexisting CSG criticality benchmark problems were converted into UM models. One such benchmark was the HEU-MET-FAST-007-037, which modeled KCODE calculations for an assembly of highly-enriched uranium slabs moderated and reflected by slabs of polyethylene [20]. Another criticality benchmark is the PU-MET-FAST-022, a bare, fast spherical assembly similar to the Godiva model except for the fact that it was composed of delta-phase plutonium metal (98% $^{239}$Pu) instead of highly-enriched uranium. One other plutonium-based criticality benchmark was the PU-SOL-THERM-001-001, which represented a 11.5 inch diameter sphere of a plutonium nitrate solution with water being used as a reflector. When verifying and validating the results of the UM models for these benchmarks, great agreement was once again found with the CSG model and experimental results (see Table 1 for k-effective values and associated uncertainties). However, the UM models had higher uncertainty values than the CSG models in the cases of the plutonium-based benchmarks.

Table 1: Results of Criticality UM Benchmarks from [20].

| **Benchmarks** | **UM Model k-effective** | **CSG Model k-effective** | **Experiment k-effective** |
|---|---|---|---|
| HEU-MET-FAST-001 | 0.9984 ± 0.01% | 1.0000 ± 0.01% | 1.0000 ± 0.10% |
| HEU-MET-FAST-007-037 | 1.0017 ± 0.01% | 1.0018 ± 0.01% | 0.9988 ± 0.08% |
| IEU-MET-FAST-007 | 1.0040 ± 0.01% | 1.0044 ± 0.01% | 1.0045 ± 0.07% |
| PU-MET-FAST-022 | 0.9960 ± 0.06% | 0.9983 ± 0.01% | 1.0000 ± 0.21% |
| PU-SOL-THERM-001-001 | 1.0030 ± 0.08% | 1.0058 ± 0.01% | 1.0000 ± 0.50% |

### 2.4.2 Shielding Benchmarks

Another set of benchmarks found within the MCNP6 test suite that pertain to UMs correspond to shielding problems. These benchmarks can be broken down even further into two subcategories: time-of-flight experiments and neutron attenuation

experiments [21]. These experiments were used alongside legacy CSG models to verify and validate both pure UM models as well as hybrid CSG/UM models. For the pulsed-sphere time-of-flight test cases, quantitative comparisons between the model results and experimental data were made using $\chi^2$ goodness-of-fit tests while the neutron attenuation experiments quantified agreement via standard deviations.

One of the aforementioned time-of-flight benchmark corresponds to experiments conducted at Lawrence Livermore National Laboratory (LLNL) in the 1970s in which time-of-flight spectra were measured by pulsing spheres of differing material compositions with 14.1 MeV neutrons [21]. These various materials used to create spheres in this experiment were beryllium, carbon, concrete, iron, water, and lithium. In terms of V&V, this benchmark was specifically meant to challenge MCNP6's UM capabilities through its time-dependent calculations. When comparing the UM modeled spectra to that of the CSG models and experimental data, both normalized and unnormalized $\chi^2$ goodness-of-fit tests yielded p-values of 0.999 or higher. As such, the null hypothesis that both the modeled and observed time-of-flight spectra adhered to the same distribution was supported.

Another time-of-flight benchmark in the MCNP test suite was that of the OKTAVIAN experiments which studied time-of-flight spectra again for deuterium-tritium (D-T) 14.1 MeV fusion neutrons in spheres composed of various filler materials [22]. The eleven materials used in these experiments to surround the fusion source and fill the OKTAVIAN sphere were aluminum, cobalt, chromium, copper, lithium fluoride, molybdenum, manganese, silicon, titanium, tungsten, and zirconium. To simulate these experiments in MCNP, first-order TET UM models were adapted from legacy CSG models of the system. More specifically, the two versions of UMs for this geometry: one with all cells separate just like the CSG model, and one where all cells with the same material were combined into one. For each of these models, neutron leakage

was simulated using surface neutron current tallies on the outside of the OKTAVIAN sphere. When comparing the results from the various UM models to their CSG counterparts for each filler material, the tally results from them seemed to overlap each other. Uncertainties in these model results were not reported, but agreement was claimed to be found between each of the model variants nonetheless.

The other benchmark found in the shielding suite is the neutron attenuation, or Ueki benchmark that studied the responses of various shielding materials to spontaneous fission from a $^{252}$Cf source [21]. In this setup, the source was contained using a paraffin cube with a conical cutout that faced the shielding material(s) and detector. While many different materials were tested during experimentation, only the graphite shields with thicknesses varying between 2 and 35 cm have been used for MCNP V&V purposes. The UM models used for V&V had several different configurations: a pure UM geometry, a hybrid geometry with an UM shield/detector and a CSG paraffin cube, and a hybrid geometry with a CSG shield/detector and an UM paraffin cube. Each of these UM models, as well as the pure CSG model, make use of volumetric flux (F4) and point detector (F5) tallies to capture the experimental data. When compared, the results of most of these tallies across each geometric configuration and shielding material thickness agree with the experimental results within 1 standard deviation. The only exception to this trend, however, can be found for the F4 tally of the Attila4MC-meshed 25 cm shield geometry which instead fell within 2 standard deviations of the experimental data.

### 2.4.3 Other Transport Benchmarks

The last set of test cases in the suite that makes use of UM geometries is the Kobayashi Analytical suite, which is designed to validate 3D Monte Carlo particle transport with analytically-solvable one-group fixed source problems [23]. These

V&V test cases were originally run for MCNP5 and once again for the initial release of MCNP6. Now, three Kobayashi test cases have been extended to accommodate comparisons between the legacy CSG model results and that of UM models. For these three geometries, comparisons were made with multiple meshes using first- and second-order TET and HEX elements. Additionally, both Abaqus and Attila4MC were used to produce separate first-order TET UM models.

The first test case within the Kobayashi Analytical suite is that of a concentric series of hollow cubes with a cubic volumetric source in the center [23]. Both the shielding/detecting cubes and the source cube are composed of either pure absorbing material or 50% absorbing and 50% scattering material. The region surrounding the series of hollow cubes is a cubic void region. In the case of the pure absorbing material cubes, general agreement was found between the CSG, UM, and analytical results. More deviation was observed between the UM results and the analytical reference for the 50/50 absorber/scatterer composition, but due to the variance reduction scheme used in the UM model, this deviation was considered negligible.

The second test case is similar geometrically to the first with the exception of the cubic volumetric source in the center being contained by a square void duct through the model rather than concentric hollow cubes [23]. For the pure absorbing material composition, all of the UM model results matched well with the analytical results consistently falling within 1.1 standard deviations of it across the entire geometry. For the split absorbing and scattering material composition, the UM results were all within 2 standard deviations of the analytical results. Most of the differences between the two stemmed from what was detected further away from the central volumetric source. Just like the first test case, however, these discrepancies are negligible as they could be reduced with an altered variance reduction scheme. As such, general agreement was found between each of the models and the analytical solution for this

test case as well. The third and final case in the Kobayashi benchmark set is similar to the second case except that the square void duct, which contains the source, now branches off several times until it reaches the boundaries of the geometry [23]. Due to its shape, this branching duct is occasionally referred to as a dogleg duct. Given the challenge that this duct geometry poses to variance reduction, this test case had the worst agreement between results of the entire set. With that in mind, the UM and CSG results still fell within 2 standard deviations of the analytical solution across the board following the same trend as the previous test cases with more agreement closer to the source. Also similar to the comparisons for the other test cases, the challenges of variance reduction were once again used to justify the discrepancies between the UM, CSG, and analytical results.

## 2.5 Unstructured Mesh Applications Beyond Benchmarks

While the current iteration of the MCNP test suite features benchmarks that have been successful in verifying and validating the code's UM capabilities, its limited scope does not adequately capture the potential utility of UMs. Some of these gaps in benchmark problem types, however, have been addressed through other applications of UMs subsequent to the public release of MCNP6. While they may not be as robust as the MCNP UM test suite parameter studies, the following applications highlight areas of interest within the MCNP user community that demonstrate the breadth of the problem space that could benefit from having benchmarks in the future.

### 2.5.1 Space Applications

One of the communities of MCNP users that have looked into using UMs for radiation transport is the space industry. One study of MCNP6's UM capabilities with regards to space radiation dates back to version 6.1.1 Beta in which researchers

at Rensselaer Polytechnic Institute (RPI) attempted to simulate radiation transport through a realistic model of a space habitat [24]. This space habitat geometry was meshed with first- and second-order TET elements using Abaqus/CAE. The authors of this study wanted to simulate the transport of various types of baryons and mesons through this geometry but had to limit their scope to more commonly-used particles such as protons and photons to accommodate the limitations of UMs in this version of the code. To analyze and visualize proton and secondary photon flux through the geometry, the authors made use of EEOUT files. While they managed to obtain some tallies for the UM models with this method, most of their runs during this study were terminated prematurely due to lost particles and, as such, did not obtain appreciable results. If this study was conducted again with a newer version of MCNP6, the issue with lost particles would likely be resolved due to the most recent changes to the UM particle tracking algorithms. Other issues revolving around energy deposition of charged particles, however, would likely still pose a challenge to the UM models created during this study and hamper efforts to obtain realistic results.

This challenge of simulating charged particle transport with UMs was discussed during a presentation given by the Space Division of the Lockheed Martin Corporation during the 2021 MCNP User Symposium [25]. Here, the authors attempted to model electron energy deposition for plates, dishes, and assemblies on the other shells of spacecrafts using UMs in version 6.2 of the code. These geometries are much too complex to be adequately modeled with CSGs, so to more accurately model dose rates to the spacecrafts, UMs would have to be used. The results for the dish and plate models had fairly reasonable uncertainty values, but the assembly model had uncertainty values much larger in magnitude than their corresponding energy deposition results. None of the results were reasonable for any of the models, however, as they all featured negative minimum energy deposition values across most of their

electron energy bins. While there continues to be interest for UMs in the space radiation community of MCNP users, the charged particle tracking algorithms in UMs will likely have to be updated to begin achieving more reasonable results. This would, in turn, pave the way for more charged particle energy deposition V&V test cases that would boost user confidence in using UMs to model dose from space radiation environments.

### 2.5.2 Medical Applications

Among MCNP users, the medical community has also demonstrated interest in the new UM capabilities. With the release of MCNP6 in 2012, researchers at LANL explored using hybrid UM and CSG models in place of the legacy voxelized CSGs to simulate the accumulation of dose in computational human phantoms [26]. The specific human phantom models analyzed in this study were the Visible Photographic Man (VIP-Man), Snyder Head, and Zubal Head. In order to maintain consistency between the CSG and hybrid geometry versions of these models, all of the UMs were created using a Python script developed to convert MCNP lattice geometries to Abaqus/CAE input decks. After tallying particle flux, energy deposition, and dose in the models from an $^{131}$I thryroid treatment, the run times for the hybrid geometry models both with and without air voxels in the lungs were found to be much higher than their CSG counterparts (see Table 2).

Beyond run times, however, general agreement was found in the volumetric flux and energy deposition tally results between the different versions of the phantom models. More specifically, when 100 million source histories were run, the relative statistical errors for the VIP-Man and Snyder Head models were found to be 0.35% and 0.31%, respectively. While this statistical agreement was found for CSG and hybrid geometry models, the researchers suggested that future work should entail

Table 2: Processing and Transport Times in Minutes For Each Human Phantom MCNP Model [26]

| **Model** | **Processing Time (min)** | | | **Transport Time (min)** | | |
|---|---|---|---|---|---|---|
| | **CSG** | **Mesh** | **Mesh*** | **CSG** | **Mesh** | **Mesh*** |
| VIP-Man (Head/Torso) | 1.0 | 998.2 | 25.2 | 1551 | —— | 19006 |
| VIP-Man (Full Body) | 4.8 | —— | 605.5 | 1187 | —— | 36171 |
| Zubal Head | 0.9 | 411.1 | 18.7 | 2688 | —— | 19715 |
| Snyder Head (8mm Voxels) | 0.2 | 0.3 | 0.2 | 1204 | 78509 | 17804 |
| Snyder Head (4mm Voxels) | 0.5 | 0.6 | 0.5 | 5490 | —— | 64580 |
| Snyder Head (Analytic) | 0.1 | —— | 0.1 | 11930 | —— | 14847 |
| Lungs (4mm Voxels) | —— | —— | 2.7 | —— | —— | 1173 |
| Lungs (UM) | —— | —— | 0.3 | —— | —— | 539 |

developing pure UM models for each of the phantoms for further V&V.

Another study based around modeling computational human phantoms with UMs was conducted in 2015 by researchers at RPI [27] using MCNP6.1. Just like the aforementioned LANL study [26], this analysis focused on simulating dose response in the VIP-Man phantom model, but instead of modeling dose from an internal treatment, the dose response was simulated for external photon and electron beam treatments. In the MCNP inputs, these beams were given energies of 0.1, 1, and 10 MeV across several runs. Additionally, rather than comparing results for a hybrid geometry and a CSG model, this study verified legacy voxelized CSG models using a pure first-order TET UM model. When comparing the results for each individual target organ in the phantom, the UM model consistently provided dose values within 5% of the CSG model.

### 2.5.3 Fusion Applications

Another community of MCNP users that has expressed interest in the development of MCNP's UM capabilities is the nuclear fusion industry. More specifically, the scientists working on the International Thermonuclear Experimental Reactor (ITER) have been using UM models to simulate incident particle flux on plasma-facing parts

within the reactor [28]. One such part was the Electron Cyclotron Upper Launcher (ECUL), which was modeled with both an UM made using Hypermesh and a CSG model converted from a CAD model using SuperMC [29, 30]. Both of these models simulated neutron transport in MCNP 6.2 to determine the spatial distribution of neutron heating on the ECUL. While the tallied results and associated uncertainties for the CSG model were relatively consistent, the results and uncertainties of the UM model varied much more in accordance with how the mesh was generated and treated before its embedding in an MCNP input deck. Despite the variance in tally results for the UM model, however, it generally produced more realistic results than those seen using the CSG approach. Because of this, the UM approach ended up being the preferred method despite the increased amount of computational resources required to run. With the results obtained from the UM model, the team at ITER was able to determine a path forward for the ECUL with regards to the materials used to shield it from the plasma.

The team at ITER once again simulated nuclear heating in the ECUL using UMs a year later after taking several shielding design changes into consideration [31]. This time, however, they gave more focus to the M3 mirror of the ECUL, a curved sheet made of copper, chromium, and zirconium designed to redirect a portion of the incident neutrons from the plasma. This geometry features several splines that could not be adequately captured using CSGs, so more development time was spent constructing a more geometrically-accurate UM model with second-order TET elements in Hypermesh. While the neutron heating results for this iteration of the ECUL's UM model were found to be 9.3% higher than that of the previous model (albeit with a different spatial distribution), the new design for the part's shielding using the M3 mirror decreased neutron heating in that region by 69%. Aside from these results, the other key takeaway noted by the team was that for UMs with very small elements

(less than 1 $mm^3$ once scaled using the LENGTH argument), the associated MCNP input deck should be optimized for running very large numbers of source particles with variance reduction schemes.

While the scientists at ITER have found MCNP6's UM capabilities to be very useful for the development of plasma-facing materials, these studies have only touched upon the verification half of V&V. Since there is no definitive date for when ITER or any other fusion reactor will begin operating, these models likely will not be validated anytime soon and instead, only be used to inform design choices during development. As such, creating a test case for UMs based around fusion applications would have to be for problems other than reactor neutron heating in the meantime.

### 2.5.4 Deformed Geometry Applications

In addition to the previously discussed applications, deformed geometries offer another possible route for UM test case development. While no studies of using UMs to model deformed geometries in MCNP have been published or made publicly available yet, some interest has been expressed in this problem type across multiple applications. One possible application of modeling deformed geometries with UMs would be simulating radiation-driven ground shock for cratered regions in the event of subsequent nuclear engagements [32]. Another possible deformed geometry application is simulating criticality for space reactors following launch failure [15]. Both of these examples would likely be difficult to model with CSGs which would require the oversimplification of the complex geometries. This issue, however, could be handled by using UMs, thereby highlighting their strengths in MCNP6.

Beyond the complexity of their shapes, another challenge to modeling deformed geometries in MCNP stems from their heterogeneous material properties. More specifically, materials that undergo plastic deformation feature localized changes in density

throughout their volumes. The very nature of this phenomenon contradicts the inherent assumption of MCNP that all materials used in radiation transport simulations are homogeneous. To accurately account for the variable densities present within deformed geometry MCNP models, the geometries would have to be subdivided into smaller groups and assigned new density values through separate material cards.

Despite these challenges, however, plastically-deformed geometries provide an interesting, new opportunity for UM V&V. Modeling deformed geometries with UMs is not a radiation transport application that has been thoroughly explored, and given the lack of study for it, its uniqueness would serve it well as an addition to the MCNP test suite. Unlike the fusion, medical, and space applications discussed prior, a test case based around this type of problem could be readily validated with an experiment using the resources available at Air Force Institute of Technology (AFIT). As such, this research will focus on exploring this topic and developing an experiment and associated model for addition to the MCNP test suite.

## 2.6 Plastic Deformation

Before discussing the development of a test case for a deformed geometry experiment, it is important to first understand the mechanics of plastic deformation and how it affects materials both microscopically and macroscopically. Additionally, this section will also discuss the use of the finite element method (FEM) or FEA for simulating loading and subsequent material deformation.

### 2.6.1 Mechanics of Plastic Deformation

As mentioned previously, one of the most significant challenges of modeling plastically-deformed geometries in MCNP is accounting for the localized changes to density throughout their volumes. As geometries are deformed, changes are made to the

crystal lattices found throughout the material as the atoms that compose them are shifted and dislocated [33]. This dislocation of atoms results in the creation of voids throughout the deformed materials and, conversely, regions that are more tightly packed with atoms. From a macroscopic perspective, the atom-clustered regions correspond to increased density while the voids correspond to a lower density. As materials experience more deformation, they experience sharper variations in density throughout their composition.

The amount of deformation and, by extension, the changes in density experienced by materials is dependent on the magnitude of applied load, or stress, to the materials. Stress $\sigma$ is defined as

$$\sigma = \frac{F}{A}, \tag{1}$$

where $F$ is the intensity of a force applied over area $A$ [34]. When a stress is positive the material is in tension, but if the stress is negative the material is in compression. The deformation, or strain, corresponding to stress is typically defined relative to unit length. More specifically, normal strain $\epsilon$ measures a material's change in size $\delta$ during deformation as

$$\epsilon = \frac{\delta}{L} \tag{2}$$

relative to its original length $L$ in the direction of the applied stress $\sigma$. For positive stresses, strain describes the elongation of a material while for negative stresses, strain describes contraction instead.

It is a standard convention to relate stress to strain for individual materials via stress-strain curves (see example in Fig. 2) [34]. These curves are derived experimentally through various methods such as tensile tests and three-point bend tests. In these plots, materials initially exhibit a linear relationship between stress and strain throughout what is known as the elastic region. In this region, the slope of the curve

is known as Young's modulus $E$, or the modulus of elasticity (see Eq. 3). In this equation, $\sigma_y$ represents the yield stress, or the stress at which the material begins to experience a nonlinear relationship between stress and strain. The property of materials to withstand loads up to the yield stress is known as yield strength. Beyond this point on stress-strain curves lies the plastic region in which materials can never fully return to their original shape following deformation.

$$E = \frac{\sigma}{\epsilon}, \sigma < \sigma_y \tag{3}$$

### 2.6.2 Modeling and Simulating Deformation

The foremost method for modeling deformation in materials is the FEM. Like the finite difference method (FDM), FEM is based around the discretization of a body and the subsequent assignment of field variables to each piece to solve boundary condition problems [35]. While the FDM solves these boundary condition problems by making point-wise approximations to governing equations and assigning field variables only at nodes, FEM applies the field variables across the entirety of the elements between nodes through interpolation schemes or shape functions.

In the case of deformation modeling, meshes are generated to represent structures and field variables in the form of material properties are assigned to the elements of these meshes [35]. These elements and their respective interpolated field variables then participate in iteratively solved equations to determine the displacement of nodes based on predefined loads and boundary conditions. Following these analyses, nodal unknowns such as stresses and strains can be obtained for each element at each solution iteration.

Over the years, several commercially-available FEA software packages have been developed to handle these types of calculations with the most prevalent being NAS-

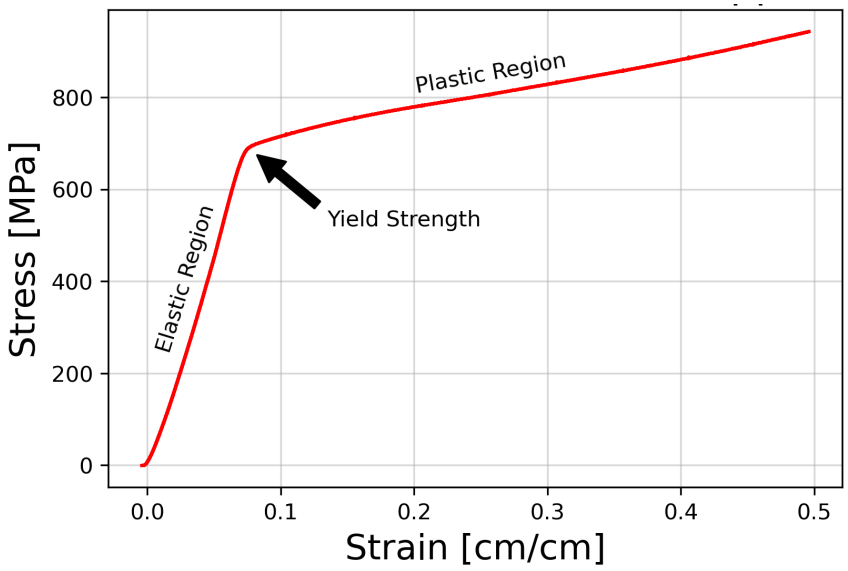


Figure 2: Experimentally derived stress-strain curve for 110 copper. As annotated in the plot, the linear region leading up to the yield strength is referred to as the elastic region, while the rest of the plot corresponds to the plastic region, which is of particular interest to this work.

TRAN, ANSYS, and Abaqus [35, 36]. These packages are capable of modeling static and dynamic loading as well as other problem types such as fluid flow, heat transfer, and electromagnetic field analyses. They also feature post-processors that allow for the governing equations' solutions to be visualized throughout each iteration and exported in various formats. In the case of Abaqus/CAE specifically, meshes may be loaded back into the graphical user interface as an output database file (ODB) following a static or dynamic analysis with the deformation from a selected solution iteration intact [37]. This allows for the deformed geometry mesh to either undergo a subsequent FEA or be exported in a form that is interpretable by MCNP.

# III. Methodology

## 3.1 Preamble

This chapter will serve to describe the approaches that have been taken to tackle the creation of MCNP V&V test cases. The first section will first cover the work that has been done to model the ATHENA-I experiment with UMs in MCNP 6.2 as well as the V&V process for that model. Beyond that, the deformed geometry experiment's design and procedure will be broken down alongside a discussion of the modeling efforts in both Abaqus and the development version of MCNP for its test case.

To create a benchmark-quality UM test case for the MCNP test suite, the process and nuances of the V&V process must be well understood. To gain familiarity with this process, an UM model for the ATHENA-I experiment was verified and validated with a CSG model and experimental data, respectively. While this test case did not feature as thorough of a parameter study as the benchmarks in the current test suite, it provided great insight into what would be needed for future MCNP UM V&V work and laid the foundation for the aforementioned repeatable methodology.

The next objective of this research entailed a much more in-depth V&V analysis for a deformed geometry shielding experiment and its associated MCNP models. Unlike the aforementioned ATHENA-I test case, this study featured V&V for UMs models of various element types and meshing schemes for greater parameterization. Additionally, the deformed geometry experiment was modeled and run using the most modern version of the MCNP code to highlight the optimization of UM processing over the course of development. Once the V&V analysis for this experiment and its models was completed, the process behind it was used to further inform the development of the repeatable UM V&V methodology. To further assist others working to verify and

validate UM capabilities in MCNP beyond the establishment of this methodology, the input decks and results for each of the test case's models are publicly available online at `https://github.com/mjeroutek/MCNP-UM-V-V-Research/`.

### 3.1.1 Assumptions and Limitations

Some of the general limitations associated with this research lie within the experimental design process. The deformed geometry experiment for the second proposed test case in this research project had to be completed using resources available on or near the AFIT campus. Therefore, the choice of radioactive sources was limited to the button sources available for use under the current, approved protocols while the deformation process was limited by access to the ENY department's MTS 810 110-kip hydraulic press. Among the radiation detectors on campus, none of the pixelated detectors were available for use, so the choice of detector was limited to smaller, portable detectors which could emulate the voxels of a pixelated detector by being moved in an array of positions between runs.

By itself, the choice of material to be deformed during the experiment provided many more limitations to the design process. It had to have material properties that would allow for the ENY department's hydraulic press to plastically deform it and achieve a deflection large enough to significantly impact density, and therefore the counts observed by the rasterized detector. The material also had to have an appreciable cross section so that the material's changes in density due to deformation would have an appreciable effect on features of measured spectra. Additionally, the material's cross sections had to be well-defined amongst nuclear data libraries in order to achieve reasonably precise results from MCNP models. By choosing a material with a simpler isotopic composition, fewer cross-sectional libraries would need to be referenced in an MCNP model's material cards thereby reducing the risk of using

less-defined nuclear data.

The creation of corresponding MCNP models (both CSG and UM) will also come with several limitations. Given the software available to AFIT students both on home computers and high performance computing (HPC) systems, the UM models for this research were created exclusively using CUBIT and Abaqus/CAE [8, 37]. Higher numbers of source particle histories were chosen to mitigate excessive statistical uncertainty and maintain consistency with the benchmarks found in the current test suite. While access to HPC systems was not available when developing the ATHENA-I test case, the deformed geometry test case did not suffer from this same issue. As such, the ATHENA-I model was limited to lower numbers of source histories to accommodate the long runtimes for UM models while the deformed geometry model was able to be run with a much higher particle count.

## 3.2 ATHENA-I Test Case

### 3.2.1 ATHENA-I Experimental Setup

A follow-on to the Energy Tuning Assembly (ETA) experiment (see Fig. 3) [38], ATHENA-I was conducted at the National Ignition Facility (NIF) in order to study the response of microelectronic devices to tailored neutron environments. More specifically, the NIF's high-density D-T fusion neutron source was used alongside a set of contiguous activation foils to separate the spectral and temporal dependencies of the device's response. Each of the activation foils used in this experiment with their corresponding thicknesses and densities can be found in Table 3.

The ATHENA-I assembly that housed these foils was made predominantly of stainless steel with most of its internal components serving to shape the spectrum of incident D-T neutrons into that of thermonuclear and prompt fission neutron sources (see Fig. 4) [39]. A layer of zirconium filled the bottom of the assembly while the

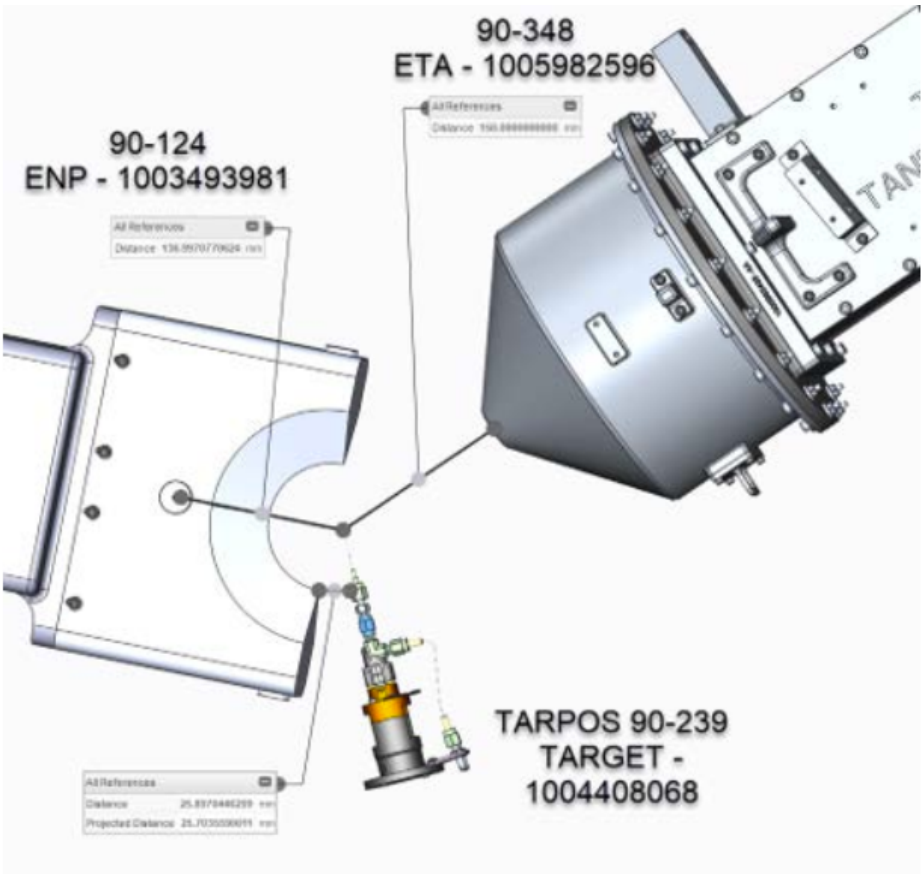


Figure 3: Experimental setup for the ETA experiment [38]. Here, the NIF's D-T neutron source is placed 15 cm away from the tip of the ETA geometry seen in the top-right portion of the diagram. The experimental setup remained relatively the same for the ATHENA-I experiment with the exception of the tuning assembly being changed to a more conical shape with a drawer for efficient replacement of activation foils and thermoluminescent dosimeters (TLDs). This new assembly geometry can be seen in Fig. 4.

central section surrounding the foil drawer was composed of tungsten instead. This stainless steel drawer built into the side of the assembly held the activation foil pack as well as an aluminum tray with eight slots for TLDs. Beyond this central region and towards the mount, carbon and delrin plastic were used to fill the upper portions of the ATHENA-I assembly.

In this experiment, four TLDs were used to measure prompt and delayed ionizing

Table 3: Thicknesses and Densities of Activation Foils Used in the ATHENA-I Experiment

| **Activation Foil** | **Density (g/cc)** | **Thickness (mm)** |
|---|---|---|
| Gold, $Au$ | 19.180 | 0.5 |
| Nickel, $Ni$ | 9.019 | 2.3 |
| Indium, $In$ | 6.913 | 2.7 |
| Aluminum, $Al$ | 2.646 | 7.3 |
| Titanium, $Ti$ | 4.303 | 2.5 |
| Tungsten, $W$ | 18.270 | 1.2 |
| Zirconium, $Zr$ | 5.815 | 2.7 |
| Magnesium, $Mg$ | 1.800 | 0.9 |
| Gold, $Au$ | 19.190 | 0.5 |

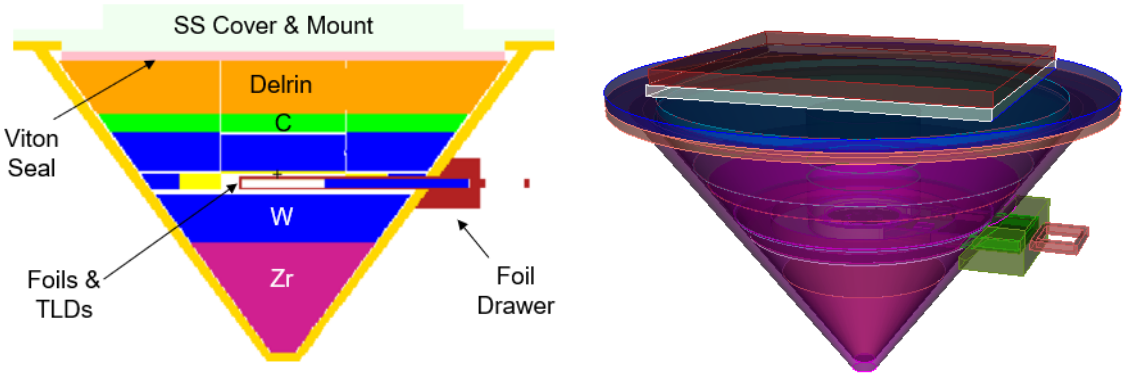


(a) Cross-sectional view of assembly (b) Visualization of assembly in CUBIT

Figure 4: (a) A cross-sectional view and (b) an isometric view of the ATHENA-I assembly geometry. The outer shell, foil drawer, cover, and mount of the assembly are made of stainless steel, while zirconium, tungsten, carbon, delrin, and viton are used within the outer shell for spectral shaping. Each of these materials are separated by thin aluminum spacers. Aluminum is also used within the foil drawer positioned on the side of the assembly to hold up to eight TLDs.

dose while the activation foils were used to unfold the neutron environment. This neutron energy spectrum unfolding process was completed using the STAYSL software suite developed by Pacific Northwest National Laboratory (PNNL) given the activa-

tion data from the foils via a least-squares fitting method across a 129 energy group structure [40]. Subsequently, this STAYSL-adjusted estimate of the neutron fluence distribution was compared to MCNP model outputs using a chi-squared goodness-of-fit test.

### 3.2.2 Development of MCNP 6.2 Models

The assembly geometry and the surrounding NIF chamber were originally modeled using CSGs by Captain Nick Quartemont (see Appendix A for the MCNP input deck) [41]. For this research, the geometry of the ATHENA-I energy tuning assembly was adapted into a first-order TET UM using CUBIT (see Fig. 5). In this mesh, a gradient of discretization was used to refine element size moving from the outer shell of the assembly to the foil chamber. Given that most of the physics of interest for the ATHENA-I MCNP model were focused in the foil drawer, this discretization strove to preserve as much of the drawer's shape as possible while reducing the features of the assembly's outer regions to reduce the amount of computational resources required to process the UM in MCNP.

Although this specific portion of the model was translated into an UM, the surrounding NIF experimental chamber and target positioning system were left as CSGs (see Appendix A for the hybrid model input deck). Given the sizes and shapes of the geometries surrounding the ATHENA-I tuning assembly, this was done in order to lower the number of mesh elements that MCNP would have to preprocess, thereby mitigating potentially exorbitant runtimes for less important aspects of the geometry. Although using a hybrid model for V&V of the ATHENA-I experiment lessened the thoroughness of meshing scheme parameterization, it did provide sufficient insight into the UM model development process that would be expanded upon later through the deformed geometry experiment.

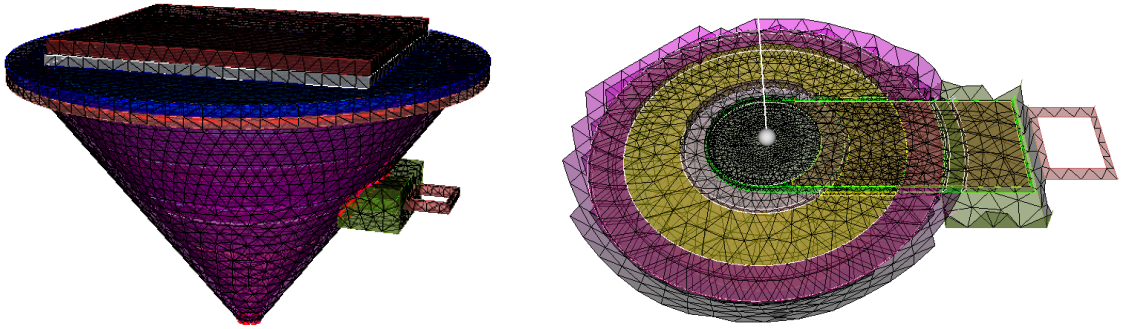

(a) Isometric view of UM

(b) Cross-sectional view of UM through foil drawer

Figure 5: (a) An isometric view and (b) an overhead cross-sectional view through the foil drawer of the ATHENA-I assembly's first-order TET UM model in CUBIT. As seen in the cross-sectional view, the mesh was intentionally made to be discretized more finely near the foil chamber given that most of the physics of interest for the MCNP model are focused there.

Despite the use of a hybrid model rather than a pure UM model, the experiment's physics of interest were relatively confined to the ATHENA-I energy tuning assembly itself, so the tally results from the hybrid model worked sufficiently for a verification study with the results of the corresponding CSG model. The specific tallies used in these models focused on volumetric neutron fluence through each the activation foils as well as the TLDs. In addition to energy-binned volumetric neutron fluence tallies for each of the activation foils individually, volumetric neutron fluence tallies for the entire foil pack as a whole were simulated in both models. Verification was conducted between these CSG and hybrid geometry results using the two-sample Kolmogorov-Smirnov Test (K-S test), a nonparametric alternative to the chi-squared test [42]. Following this verification process, the hybrid geometry model was also validated by using volumetric fluence tallies for the entire foil pack as inputs in STAYSL for the aforementioned chi-squared goodness of fit with the experimentally-determined

unfolded energy spectrum.

## 3.3 Deformed Geometry Test Case

### 3.3.1 Exploratory MCNP Simulations

As discussed in Chapter II, one facet of plastic deformation that poses potential issues for modeling deformed geometries in MCNP is the introduction of localized changes in density. Since the material properties of all cells in MCNP are treated as homogeneous, geometries must be subdivided into multiple smaller groups that are all assigned their own new density values in order to account for these changes. Subdividing CSG models can be computationally expensive for geometries with greater variation in density due to the increase in the number of surfaces that MCNP must parse through during particle transport; UM models, however, do not reference surfaces and rely on alternate tracking methods for radiation transport as discussed in Section 3 of Chapter II. As such, UM models should be more accurate and computationally efficient than CSG models for simulating deformed geometries in theory on account of both their complex shapes and their locally varying densities respectively. To test this, several exploratory models of a deformed geometry were created and analyzed.

In order to be able to subdivide UMs of deformed geometries and adjust their densities, a Python script known as *UM_vardens.py* was developed (see Appendix A). In this script, element volumes are imported from CUBIT-reported shape metrics of Abaqus input decks both before and after deformation is simulated in Abaqus. The Abaqus input decks for the geometries post-deformation were obtained by importing the ODB produced by the FEA Abaqus job as a model part at its final time step and then exporting that deformed part as a new Abaqus input deck. The matching pre- and post-deformation volumes retain the same mass resulting in the new density

corresponding to an element's volumetric ratio.

Given that UMs typically feature a large number of elements and that CUBIT reports shape metrics with a high degree of precision, this script would originally discretize deformed meshes into an exorbitant number of cells. To optimize this code's performance and decrease runtimes, a binning system was developed to separate the calculated densities into a user-defined number of bins with values ranging from the smallest to largest reported densities. These bins hold wider ranges of densities near the upper and lower bounds and become more finely discretized near the mode, or most common value, of the new densities.

While this binning system works well as is for discretizing UMs with relatively consistent element sizes, the bounds for the density bins can be dominated by changes in volume to either small or large elements if the input mesh features elements with greatly varying sizes. For example, if a mesh features mostly equally-sized elements with the exception of a few much smaller elements, those smaller elements could feature more drastic changes in volume than the average element, which the script would interpret as very large density changes. These new density values calculated for the smaller elements would raise the upper limit of the density bins, and as a result, many average-size elements would be binned incorrectly with their actual new densities not being accurately reflected in the final discretized version of the input mesh. To address this issue, the script assigns weighting factors to each element before the binning process. These weights are calculated based on the ratio of an element's volume to that of the average element in the mesh. As such, volume changes to small and large elements no longer have substantial impact on the upper and lower bounds of the density bins respectively due to their new weights.

Once all elements are properly weighted and assigned to bins by the script, the deformed iteration of the imported UM is discretized into a number of multiple parts

equivalent to how many bins are used. After this process, the newly subdivided UM is then written to an Abaqus input deck and formatted specifically for use in MCNP6 by renumbering elements and assigning them to *set-material* and *set-statistic* element sets. Additionally, a CUBIT journal file is written to allow for easy visualization of the density-adjusted UM before being processed in MCNP.

For this research, MCNP input decks corresponding to the UMs exported by this script were constructed partially using the *um_pre_op* tool included in public distributions of MCNP due to how finely they were discretized in terms of density. This tool automatically constructs a MCNP input deck skeleton with populated UM embedding cards based on an Abaqus input deck [7]. While this tool is not required for this process, it greatly expedites the creation of MCNP input decks for UM models, especially when those model assemblies are comprised of many separate parts.

Initial testing of this Python script was done on a UM model in MCNP 6.2 for a cratered 5 x 5 x 5 cm block model in order to inform future modeling and experimental development of a deformed geometry test case. This model was subdivided into 10 parts using the aforementioned script to account for localized changes to density from deformation (see Fig. 6).

In MCNP, both versions of the model were assigned to be made entirely of borated polyethylene, and a 5 x 5 cm plane source of Wattfission neutrons was placed to the side of the model extending slightly above the lip of the crater. Given the high neutron absorption cross sections of boron, the transmission of neutrons through the model was studied to see how it was affected by localized changes in density from the simulated deformation. On the opposite side of the block with the same vertical displacement as the plane source, a 5 x 5 cm FMESH4 tally with a 50 x 50 grid resolution was used to determine how many neutrons were able to pass through the geometry. The results from both the varied density and homogeneous versions of

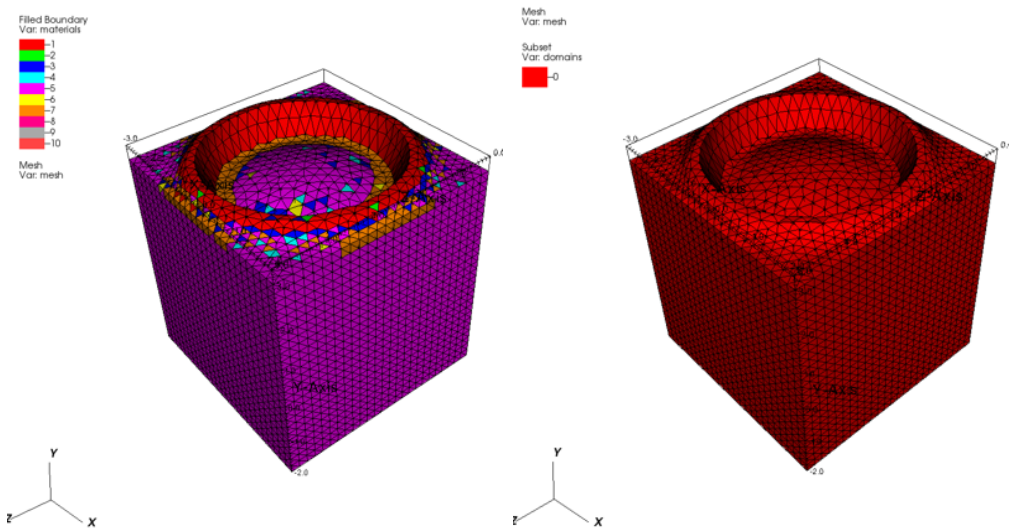


(a) Variable density model (b) Homogeneous model

Figure 6: Visualizations of the cratered block model in LLNL's VisIt software [43] (a) with and (b) without subdivisions to account for changes to density. The variable density version of the model is subdivided into 10 parts due to the number of bins used in the *UM_vardens.py* script.

the model were compared, and differences of up to 34.5% were found between the two relative to the latter model (see Fig. 7). The highest difference in relative error, on the other hand, was only about 1.1%. As such, these results demonstrated that accounting for changes in density does make a difference when modeling deformed geometries in MCNP.

### 3.3.2 Experimental Design and Procedure

While these results were promising for developing a test case and obtaining data in favor of this UM discretization methodology, several adjustments had to be made to the cratered model design in order to develop a more realistic experiment. As seen in Fig. 7, much of the model was not perturbed by the simulated deformation. To address this issue, the geometry for the experiment was changed to a 10 x 6 x 1.27 cm plate with a crater region taking up more of its overall volume. Additionally,

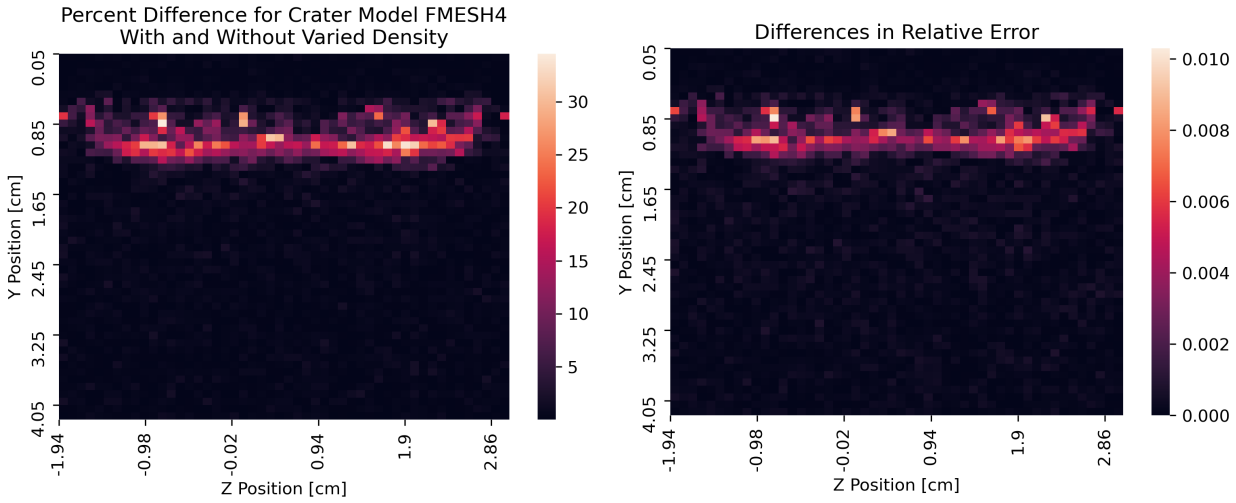


(a) Percent difference in results

(b) Difference in uncertainties of results

Figure 7: Differences in (a) FMESH4 tally results and (b) their respective uncertainties for the cratered borated polyethylene block model. Before this comparison, the FMESH4 tally results were reported in units of neutrons per square centimeter. The percent difference in Figure 10a was calculated relative to the homogeneous density version of the model. The highest percent difference found between the results was approximately 34.5% while the highest difference in relative errors was about 1.1%

the plate would be rotated to have the incident particles pass through the deformed face of the material rather than its side. With this change, more spatial information could be acquired from a set of rasterized measurements than what would have been possible with the previous design.

Another adjustment to this design involved the particles being transported. While the exploratory model made use of Watt fission neutrons, access to radioactive sources under active experiment protocols at AFIT limited the test case experiment to only using low-activity gamma sources. The specific source chosen to be used in this experiment was a 6.12 $\mu$Ci $^{137}$Cs button source. A direct byproduct of this adjustment was that the material of the deformed geometry also had to be changed. Instead of borated polyethylene, stainless steel 316 (SS 316) was originally chosen as a replacement material to attenuate photons rather than neutrons. While it would have functioned well to shield Compton scattered photons from the $^{137}$Cs source, this material selec-

tion featured a glaring issue. Due to SS 316's high yield strength of 29,732 psi [44], a material with a higher yield strength would have to be used for an indenter to achieve substantial deformation and a noticeable change in density. Given that steel was the strongest material that the AFIT model shop had available to manufacture a custom indenter, SS 316 would not be able to be deformed substantially using the AFIT ENY department's MTS 810 110-kip hydraulic press.

Thus, 110 copper was selected to replace SS 316 as the material to be deformed in this experiment due to its material properties. With an elemental composition of 99.96% copper and 0.04% oxygen, this variant of copper is highly ductile with a yield strength of 10,000 psi and an ultimate tensile strength of 32,000 psi [44]. Given these values, 110 copper could be deformed using the MTS 810 hydraulic press with relative ease. This press uses a 4"-diameter pad indenter by default and can apply up to 110 kips of force, or up to approximately 8,750 psi of stress with this specific indenter. While this maximum load is lower than the yield strength of 110 copper, a custom-made indenter with a smaller surface area than the 4"-diameter pad could increase the amount of stress applied to the plate and, by extension, cause significant plastic deformation. For this experiment, a steel cylindrical indenter with a 2 cm diameter was developed by the AFIT Model Shop, as its smaller area of contact would allow for a maximum load of approximately 225,900 psi, well beyond what is necessary to achieve substantial deformation in the plate. Given that the press would not be used to apply nearly that much pressure, scrap steel was chosen as the indenter material due to the generally higher yield strengths of steel variants relative to copper (these values range from around 20,000 psi all the way up to 360,000 psi) [45].

Beyond these mechanical properties, 110 copper can also attenuate an appreciable portion of incident gamma radiation at energies of less than 1 MeV (see Fig. 8 and 9) [46]. By focusing on photoelectric interactions from the $^{137}$Cs source's 662 keV

photon emissions, this property could highlight the changes to the plate's thickness and density via deformation. The number of uncollided photons after transiting 110 copper can be calculated as

$$\frac{I}{I_0} = e^{-\mu x}, \tag{4}$$

where $I$ is shielded intensity, $I_0$ is incident intensity, $x$ is the plate's thickness, and $\mu$ is the linear attenuation coefficient, or the mass attenuation coefficient multiplied by the density of the plate. With this, it was found that 43.9% of incident gammas would penetrate the full thickness of the copper plate (half of an inch) at its original density without interaction while in the quarter-inch-thick cratered region, 66.2% of them would make it through. When using the highest new density value of 10.55 $g/cm^3$ for the copper plate post-deformation (discussed later this chapter in Section 3.5), 61.4% of incident photons would transit the cratered region of the plate without losing energy instead.

Additionally, in terms of modeling, this material serves to simplify radiation transport calculations due to its straightforward elemental composition (99.96% copper and 0.04% oxygen) limiting the number of cross-sectional dependencies required and mitigating the effects of potential errors in nuclear data libraries. To gain a better understanding of the copper plate's material composition for both the deformation and radiation transport modeling processes, it was ordered from the local metal vendor Alro which provided certification of its composition.

Aside from the material and source selection, another major adjustment to the exploratory cratered model was the method of detecting transmitted particles. In the original model, an FMESH4 tally was used to simulate a 50 x 50 array of detectors with 1 $mm^2$ apertures. Given the lack of realism in this tally, a detector array with a lower resolution had to be selected. While a pixelated high-purity germanium detector

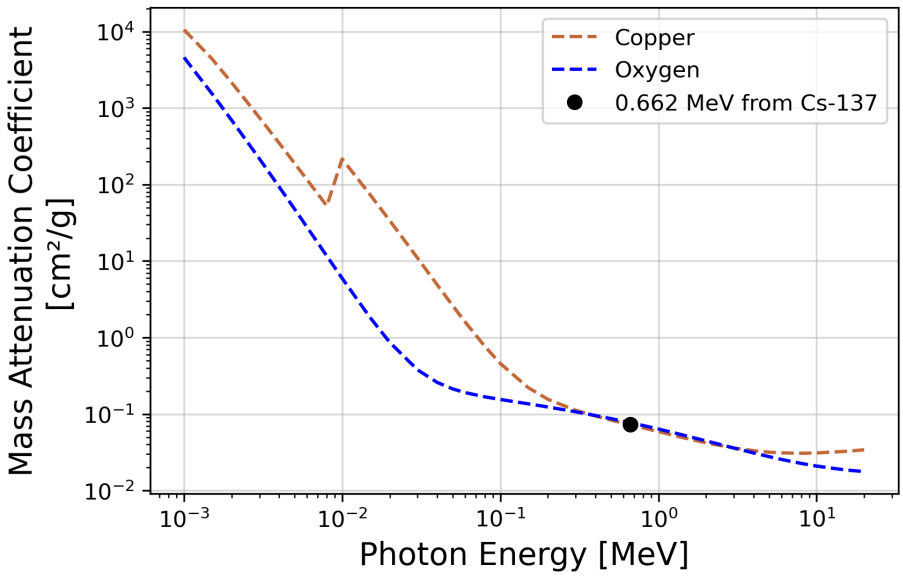


Figure 8: Mass attenuation coefficients for copper and oxygen as per the NIST database [46]. Given that 110 copper is 99.96% copper and 0.04% oxygen, the mass attenuation coefficient and linear attenuation coefficient for Cs-137's 0.662 MeV photon emission in 110 copper at its original density of 8.93 g/cm$^3$ are 0.0727 $cm^2/g$ and 0.649 $cm^{-1}$, respectively.

would have been able ideal to take measurements in a smaller array, one could not be procured for this experiment, and an alternative plan had to be devised. Instead of using a pixelated detector, a Kromek GR1-A cadmium zinc telluride (CZT) detector was chosen to be moved in an array of equally-spaced positions behind the plate for separate runs to emulate pixels. In addition to being able to operate at room temperature, this semiconductor detector features a small size with a 1 x 1 x 2.43 in. outer casing and a 1 cm$^3$ CZT crystal. Given this size and portability, the GR1-A was able to achieve a resolution fine enough to observe differences throughout the plate post-deformation due to density changes.

To ensure that this detector was able to move in precise increments of 1 x 1 cm behind the copper plate, the AFIT Model Shop developed a 6 x 6 cm detector-array assembly that could also hold the 110 copper plate in place (see Fig. 10). The plate nest and the saddle piece that held the detector in each position were 3D printed

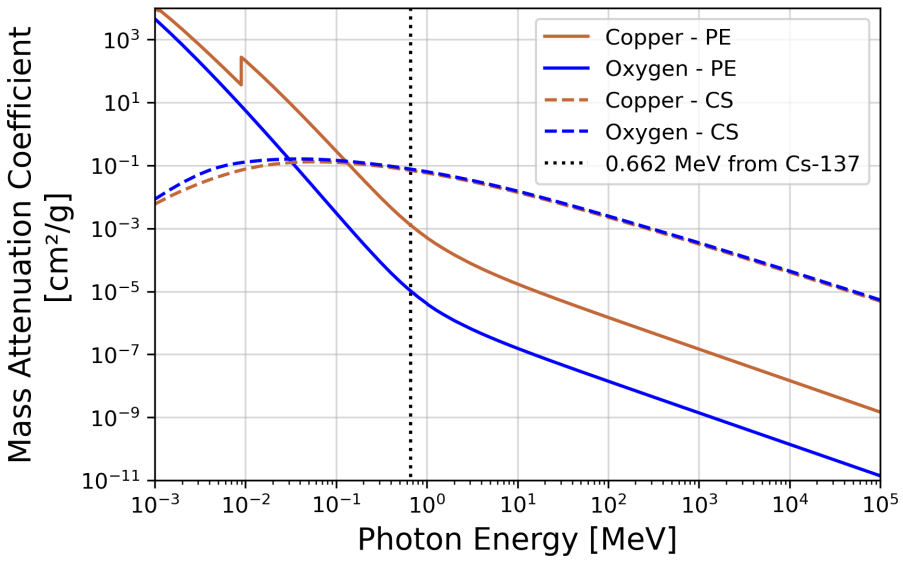


Figure 9: Mass attenuation coefficients for the photoelectric effect and Compton scattering in copper and oxygen as per the NIST database [46]. While the photoelectric effect dominates at lower energies, Compton scattering becomes the dominant photon interaction mechanism at energies of approximately 150 keV and 30 keV for copper and oxygen, respectively.

out of nylon 6, while the rest of the assembly was made using aluminum. The plate nest covered 2 cm worth of the copper plate on each side resulting in a 6 x 6 cm face to be used for the experiment. The saddle piece was able to be moved horizontally in increments of 1 cm and held in place via two screws that extended through a crossbeam above. This crossbeam was attached to two uprights with 6 holes each in order to move in 1 cm increments vertically as well.

With the assembly ready, the GR1-A detector was connected to a computer via USB connection for spectroscopic analysis using Kromek's MultiSpect software. With this tool, an energy calibration could be performed and saved permanently for the specific detector connected using the low-activity gamma button sources covered under the active protocol. For this, a $< 10\mu$Ci $^{60}$Co button source was used in addition to the aforementioned $^{137}$Cs source to ensure that the energy was calibrated to more than just a single point (661.67 keV). Additionally, as counts were taken in each po-

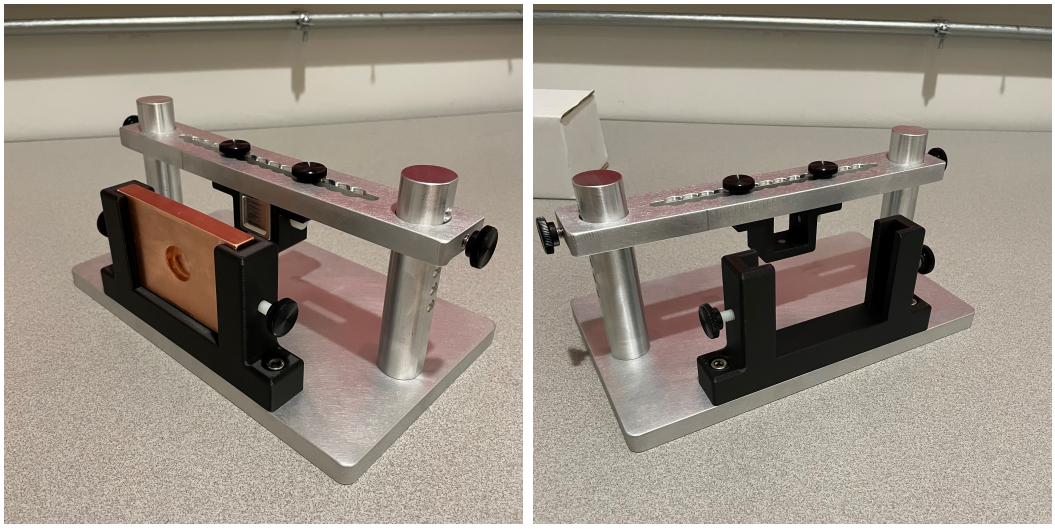

(a) With plate and detector (b) Without plate and detector

Figure 10: Detector-array and plate nest assembly constructed by the AFIT Model Shop (a) with and (b) without the detector and copper plate in place. The plate nest and saddle beneath the detector were 3D printed out of nylon 6 while the rest of the assembly was made out of aluminum.

sition behind the plate, the MultiSpect's automatic Gaussian fitting functions were used to determine the total gross and net counts, or counts without and with background counts subtracted, under the measured 661.67 keV photopeaks. These values would subsequently be exported alongside reported real and live times to a Python script for analysis and comparison to corresponding UM MCNP models.

With this experimental setup, several measurements were taken in 6 separate positions behind the copper plate. The raster assembly allowed for the detector to be moved in a 6 x 6 array of 1 $cm^2$ positions, so these 6 positions were aligned vertically in one of the two central columns behind the plate to observe the sharpest effects of altered density with the fewest possible runs. Measurements were taken twice in these positions with each run lasting for approximately 2 hours to observe approximately 10,000 net counts within the 662 keV photopeak thereby minimizing uncertainties in counting statistics.

### 3.3.3 Experimental Uncertainty Analysis

An important factor to consider throughout this experiment was the propagation of uncertainty through the multiple processes involved. In order to achieve high fidelity results inline with that of the aforementioned UM benchmarks in the MCNP test suite, these uncertainties had to be quantified and mitigated whenever possible. For this experiment, the primary sources of uncertainty stemmed from the tolerances of the 110 copper plate to plate sawing during manufacturing, the precision of the MTS 810 hydraulic press during the deformation of the plate, and the counting statistics during the actual runtime of the experiment. These sources can all be related by total counts $N$ by

$$N = \epsilon(E) A t e^{-\mu_p(E) t_p - \mu_w(E) t_w} \tag{5}$$

where $A$ is source activity, $t$ is the measurement time, $t_p$ is plate thickness, $\mu_p(E)$ is the the copper plate's linear attenuation coefficient, $t_w$ is detector window thickness, and $\mu_w(E)$ is the detector's window (aluminum) linear attenuation coefficient. Detector absolute efficiency is also represented in Equation 5 as $\epsilon$(E), which can be derived as

$$\epsilon(E) = \frac{r}{\Omega F(E) A} = \frac{N}{f_a A t} \tag{6}$$

where $r$, $\Omega$, $A$, and $F(E)$ correspond to net count rate, solid angle, source activity, and an energy-dependent correction factor for source self-absorption and backscattering, respectively [47]. Detector absolute efficiency $\epsilon$(E) can also be defined in terms of counts $C$, a self-absorption correction factor $f_a$, source activity $A$, and time $t$. This self-absorption correction factor was calculated as

$$F(E) = f_a = \frac{1}{\mu_s(E) t_s}(1 - e^{-\mu_s(E) t_s}) \tag{7}$$

using the source casing linear attenuation coefficient $\mu_s(E)$ and thickness $t_s$. When combined, all of these equations can instead be written as

$$N = \frac{A\ t\ e^{-\mu_p(E)t_p - \mu_w(E)t_w}\left(1 - e^{-\mu_s(E)t_s}\right)}{\mu_s(E)t_s}, \tag{8}$$

allowing for the total counts to be calculated if the measurement time and conditions are known. Alternatively, the measurement time to a given number of counts can be calculated as

$$t = N\ \frac{\mu_s(E)t_s}{A\ e^{-\mu_p(E)t_p - \mu_w(E)t_w}\left(1 - e^{-\mu_s(E)t_s}\right)}. \tag{9}$$

Using 10,000 as the desired number of counts, a time value of 6281 seconds per run was found using Eq. 9 and the values in Table 4. With this time and an estimated uncertainty of 30 seconds, the uncertainties in each of the terms in Equation 10 were calculated in order to find the uncertainty in the total measured counts $N$.

$$\begin{aligned}\delta_N = \Bigg[ &\left(\frac{\partial N}{\partial t}\right)^2 \delta_t^2 + \left(\frac{\partial N}{\partial \mu_p}\right)^2 {\delta_{\mu_p}}^2 + \left(\frac{\partial N}{\partial t_p}\right)^2 \delta_{t_p}^2 + \left(\frac{\partial N}{\partial \mu_w}\right)^2 {\delta_{\mu_w}}^2 \\ &+ \left(\frac{\partial N}{\partial t_w}\right)^2 {\delta_{t_w}}^2 + \left(\frac{\partial N}{\partial A}\right)^2 \delta_A^2 + \left(\frac{\partial N}{\partial \mu_s}\right)^2 {\delta_{\mu_s}}^2 + \left(\frac{\partial N}{\partial t_s}\right)^2 {\delta_{t_s}}^2 \Bigg]^{1/2}\end{aligned} \tag{10}$$

The uncertainties for each of the linear attenuation coefficients seen in Table 4 were determined by simulating the self-shielding of the button source casing in MCNP and applying the output photon values to the values seen in the NIST X-Ray Mass Attenuation Database [46]. In addition, the statistical uncertainty in the counts, $\delta_C$, can be approximated by taking the square root of the total measured counts as per Poisson statistics [47]. Thus, the total uncertainty, $U$, is

$$U = \sqrt{\delta_N^2 + \delta_C^2}. \tag{11}$$

Table 4: Terms Used Throughout Error Propagation

| Term | Value | Uncertainty |
|---|---|---|
| Activity, $A$ | $2.486 \times 10^5$ $Bq$ | 2717 $Bq$ |
| Time, $t$ | 6281 $sec$ | 30 $sec$ |
| Source Linear Attenuation Coefficient, $\mu_s$ | 0.141 $cm^{-1}$ | 0.003 $cm^{-1}$ |
| Plate Linear Attenuation Coefficient, $\mu_p$ | 0.649 $cm^{-1}$ | 0.007 $cm^{-1}$ |
| Detector Linear Attenuation Coefficient, $\mu_d$ | 0.217 $cm^{-1}$ | 0.003 $cm^{-1}$ |
| Source Thickness, $t_s$ | 1.270 $cm$ | 0.0127 $cm$ |
| Plate Thickness, $t_p$ | 1.270 $cm$ | $10^{-4}$ $cm$ |
| Detector Window Thickness, $t_w$ | 0.265 $cm$ | 0.003 $cm$ |

In Eq. 10, the linear attenuation coefficient terms, source thickness term, and detector window thickness term (not just the uncertainties $\delta_{\mu_s}$, $\delta_{\mu_p}$, $\delta_{\mu_w}$, $\delta_{t_s}$, and $\delta_{t_w}$) were all found to be negligible given that they contributed far less than 1% to the propagated uncertainty value. The activity term, on the other hand, contributed the most to the final term (73.8%) with the plate thickness and time terms contributing 20.2% and 6.04% respectively. For a runtime of $6280 \pm 30$ seconds, the uncertainty in counts $\delta_N$ was found to be 1.26%. When combining $\delta_N$ and a counting statistics uncertainty $\delta_C$ of 1% as per Eq. 11, a total uncertainty $U$ of 1.61% is found.

### 3.3.4 Plate Deformation Process

For this research project, the AFIT Model Shop provided a custom steel cylindrical indenter to be used with the hydraulic press to achieve significant deformation of the copper plate (see Fig. 11). The shape of the indenter was chosen to observe sharper changes in density between the affected and unaffected regions of a plate. To assist with properly aligning the indenter with the plate and providing visual indication of deformation, the Model Shop also etched the plate with a light ink in a 1 $\times$ 1 cm pattern.

With the custom indenter and the etching process completed, the copper plate

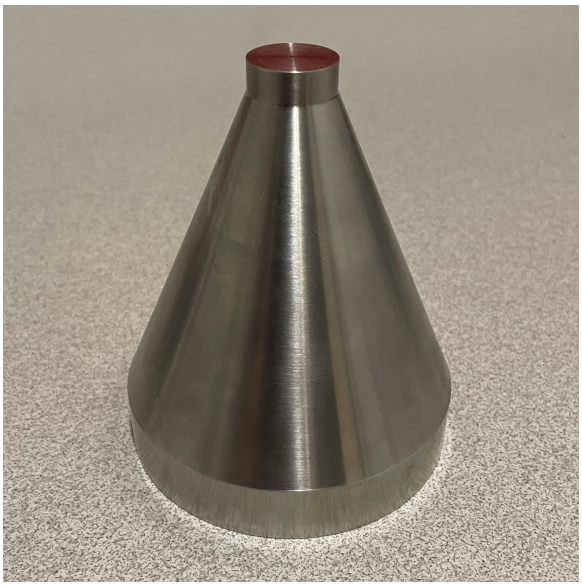

Figure 11: Manufactured steel cylindrical indenter with a 0.79 in. (2 cm) diameter face to indent the 110 copper plate. The back of the indenter featured a 3 in. (7.62 cm) diameter to maximize contact with the hydraulic press pad. To ensure that the crater in the plate would be cylindrical, the top of the indenter was extruded by half of the plate's thickness (0.25 in. or 1.27 cm).

was deformed at the AFIT ENY department's materials research laboratory using a Material Test System (MTS) 810 hydraulic press (see Fig. 12).

To operate this machine, it was connected to a computer with an installation of MultiPurpose TestWare Software (793), or MPT/793. Through this program, the pads of the press could be manually moved in increments or the press could be set to run automatically through the definition of loading ramp function procedures. To indent the copper plate with the custom steel indenter, the indenter was centered atop the plate before the upper pad of the press was manually moved downwards to make light contact with it. Once the upper pad was in this position, a procedure was defined in MPT/793 to move the indenter downwards at a rate of 0.01 mm per second until a deflection of a 0.25 in. or 1.27 cm (half the plate's thickness) was achieved. While no specific load was specified in this procedure, pressure data was still acquired by the software throughout the run and was subsequently exported


Figure 12: The MTS 810 hydraulic press workstation used to indent the copper plate for this experiment. This machine featured two 4"-diameter pads that the plate and custom steel indenter were placed between. This press connected to the computer on the right which allowed for the pads to be moved vertically via controls in the MultiPurpose TestWare Software (793), or MPT/793.

alongside the deflection data (see Fig. 13).

Based on this deflection and pressure data, a yield point for 110 copper was observed at an applied stress of about 684.52 MPa which is almost an entire order of magnitude higher than the expected value of 68.95 MPa [44]. While some materials feature different yield points depending on whether they are in tension or compression [32], this should not be the case for this copper alloy [48]. As such, it is likely that there was a calibration error in either the pressure sensors of the hydraulic press

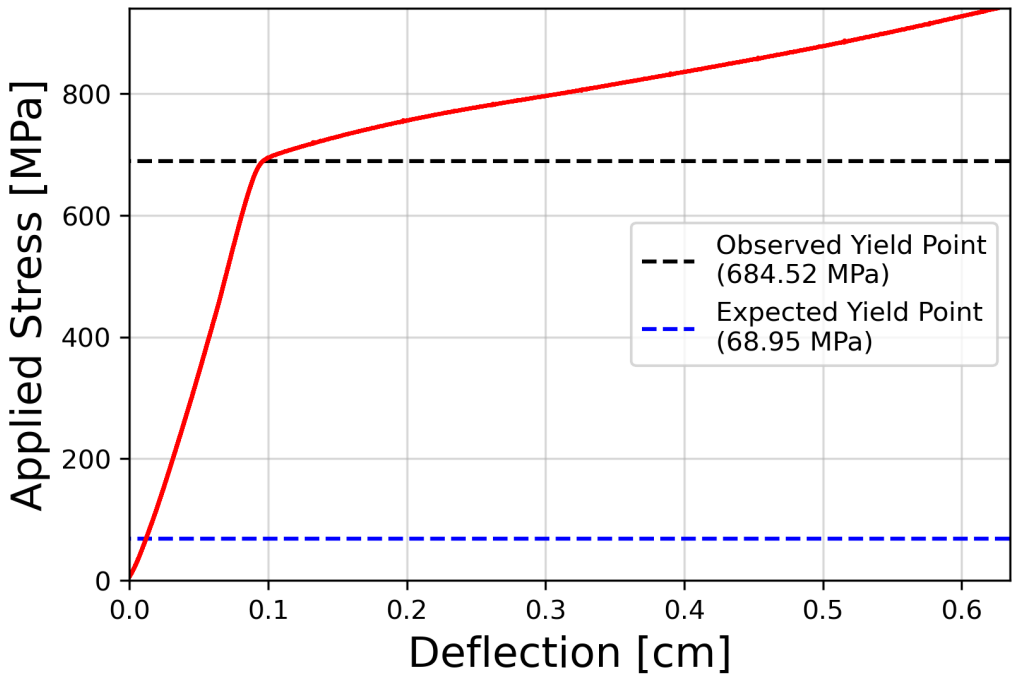


Figure 13: Pressure and deflection data from the plate deformation procedure exported from the MPT/793 software. The observed yield stress was approximately 684.52 MPa while the expected value was closer to 68.95 MPa.

or the data acquisition routines of the connected MPT/793 software.

Despite this discrepancy, the copper plate was successfully deformed to the desired deflection of half of its thickness. While this deflection was correct, however, the intended shape of the plate was not, as the sides of the plate began to curve upward near the end of the indentation procedure (see Fig. 14).To address this issue, the steel indenter was removed from the cratered plate, and the upper press pad was moved downwards incrementally to bend the plate back to its original shape (see Fig. 15). To ensure that the press was able to properly straighten the plate, it was placed into the 3D printed nylon 6 plate holder on the detector raster assembly seen in Fig. 10 where it fit snugly as intended.

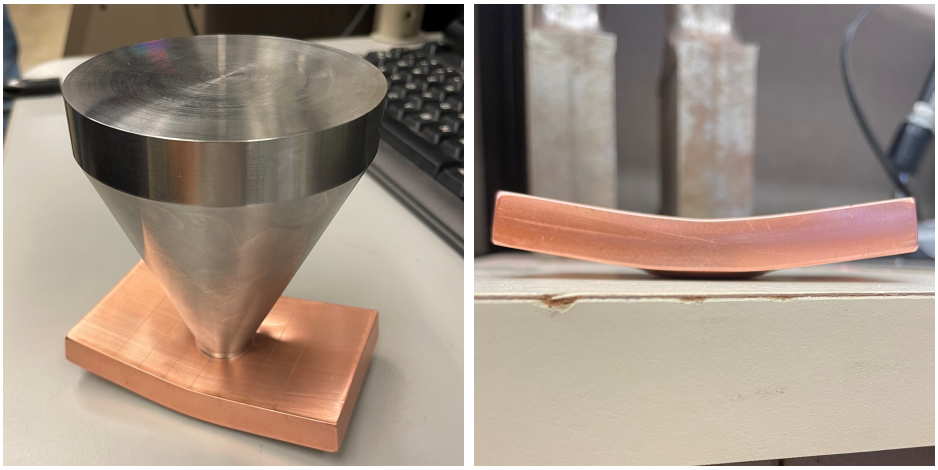

(a) Before indenter removal (b) After indenter removal

Figure 14: Bent copper plate (a) before and (b) after the removal of the steel indenter.

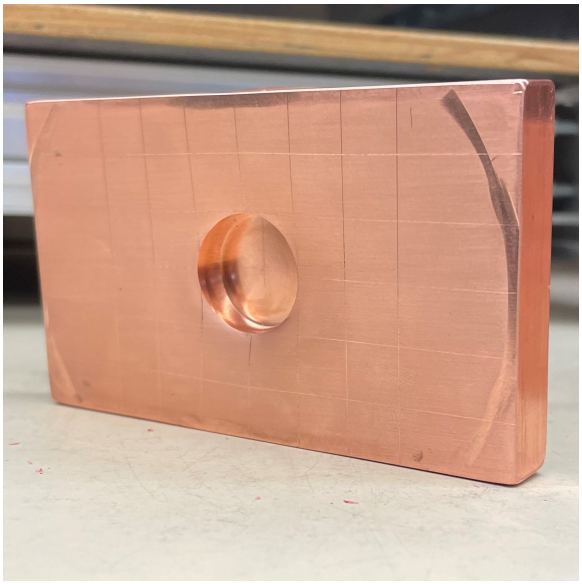

Figure 15: Copper plate after being bent back to its original shape by the MTS 810 hydraulic press.

### 3.3.5 Deformation and Radiation Transport Modeling

As with the UM model for the ATHENA-I test case, the mesh for this test case was also developed using CUBIT 15.6. While the plate and $^{137}$Cs button source were modeled using CUBIT's volume definition feature, the rest of the detector raster assembly was imported from SolidWorks instead (see Figure 16). Unlike the ATHENA-I

model, however, both first-order TET and HEX models were developed for this geometry. Since the deformation of these models could not be accomplished using only CUBIT, both plate meshes had to be exported alongside indenter models as Abaqus input decks and imported into Abaqus/CAE 2020 (see Fig. 17).

Before the plate model input decks could be used for FEA in Abaqus though, several more specifications had to be made to them. First, material properties had to be assigned to the 110 copper plate and steel indenter in each mesh. Additionally, master-slave relations had to be established for both models by allowing Abaqus to automatically detect contact regions between the plate node sets and that of their corresponding indenters. With the material properties and interactions established, separate time steps were created to allow for the iterative solutions to the nodal displacements within the meshes. To model the physical deformation process as closely as possible, boundary conditions were then propagated through each of these time steps. These conditions were used to specify that the sides of the plates should not move throughout the deformation process. They were also used to displace the indenter node sets towards the plates by a quarter inch over the course of 100 time steps before moving back for the final 100 and allowing the plates to relax.

With the plate meshes now deformed, they were both imported back into CUBIT. Here, they were exported once more to ensure that each of their Abaqus input decks were CUBIT-formatted for use in the *UM_vardens.py* script. With this, each plate model was then discretized by density into ten separate bin. Through this process, it was found that the density of the 110 copper plate models (originally 8.93 g/cm$^3$) varied by up to approximately 18.17%.

After being discretized, the plate models were then returned to CUBIT where they would be added back to their corresponding experimental setup meshes. Each subdivision of the plate as well as the rest of the parts in the assembly were then

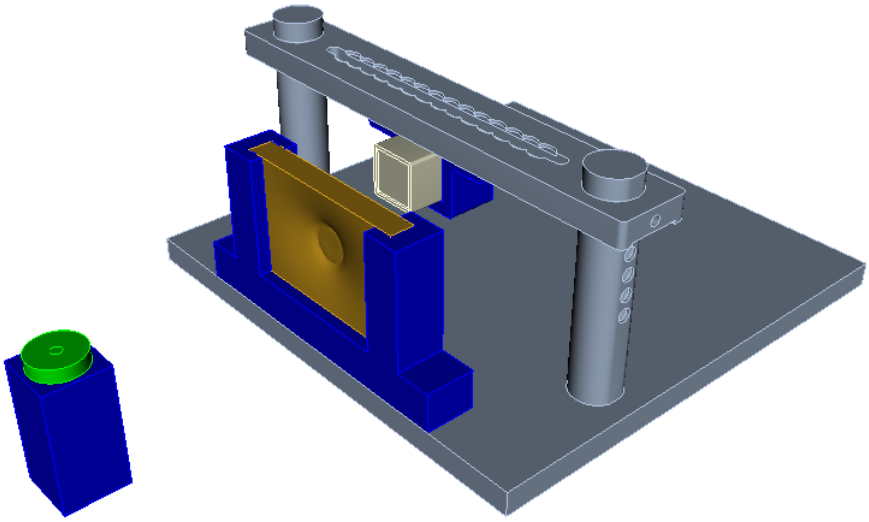

(a) Solid View

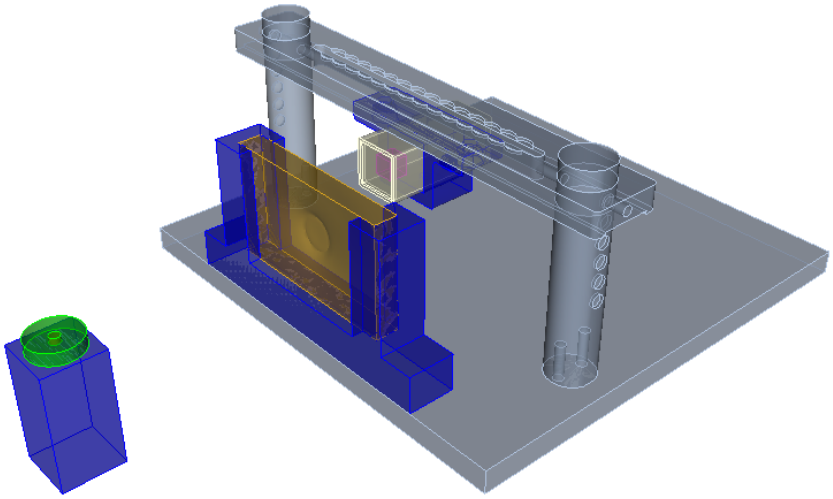

(b) Transparent View

Figure 16: (a) Solid and (b) transparent views of the experimental setup in CUBIT 15.6. The blue and grey volumes correspond to the assembly's 3D printed nylon 6 and aluminum parts respectively. The CZT crystal can be seen modeled in magenta inside the light yellow detector casing.

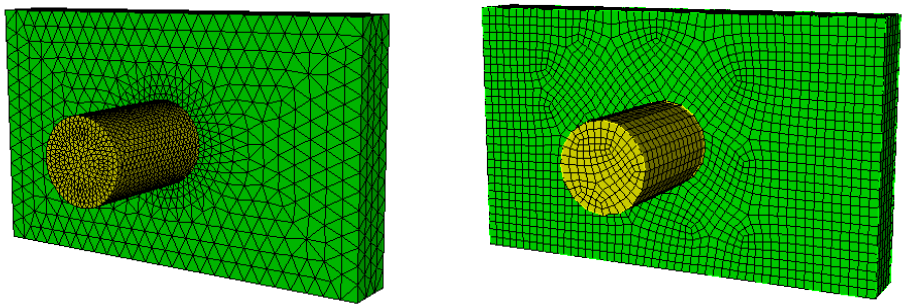

(a) TET Model (b) HEX Model

Figure 17: (a) TET and (b) HEX models for the 110 copper plate and 2 cm diameter cylindrical steel indenter. The TET mesh was generated using CUBIT's Tetmesh scheme while the HEX was meshed using the Pave scheme instead.

reformatted for MCNP by assigning them to material and statistic element sets. In addition to these sets, the button source parts were also assigned to source element sets to allow for MCNP to interpret their respective pseudo cells as volumetric sources through the VOLUMER argument in the SDEF, or source definition card. The TET and HEX model Abaqus input decks were then duplicated five times each to move the instances for the crossbeam and detector parts down vertically on the uprights and model the rest of the positions used throughout the experiment.

For each of these UM models, the *um_pre_op* tool was used to generate corresponding MCNP input deck skeleton files (see Appendix A for full input decks). With the cells and surface for the mesh universe bounds already made, only the data cards still needed to be written. For each of these inputs, an NPS of 100 million source particles was used while the SDEF card specified that the button source pseudo cells emitted 662 keV photons isotropically. The material cards for each of the pseudo cells were written based on material compositions provided by PNNL, the button source's manufacturer, and Alro [49, 50, 44]. In order to simulate the gamma spectroscopy done in the experiment using the GR1-A CZT detector, the tallies used in each of these inputs were F8 pulse-height tallies binned by energy to look for 662 keV photons

specifically. With these input decks completed, they were then run on AFIT's HPC systems using a developmental version of MCNP.

# IV. Results and Analysis

## 4.1 Preamble

This chapter will cover the results and their subsequent analyses for both the ATHENA-I and deformed plate test cases. Following this, the uncertainties in the results originating from the modeling and simulation processes described in Chapter III will also be discussed.

## 4.2 ATHENA-I Test Case Results

For the volumetric neutron flux in each of the activation foils individually, general agreement was found between the CSG and hybrid geometry models' results using the K-S test with a null hypothesis that the compared data set samples were drawn from the same distribution [42]. Through this test, low K-S test statistics and p-values of approximately 1 were calculated for all of the foil tallies across both models. The comparison of results for the first gold activation foil in the pack can be seen below in Fig. 18 (see Appendix B for the rest of the individual foil tally results).

For the volumetric flux tally across the entire foil pack, however, the results did not line up quite as well with the K-S test instead providing a slightly higher test statistic and a lower p-value of about 0.0769 and 0.838, respectively (see Figure 19). While this statistical test result did not suggest agreement between tally results as strongly as was seen for the results of the individual foil tallies, the test statistic and p-value were still low and high enough, respectively, that the null hypothesis cannot be rejected thereby indicating that the two distributions are indeed identical.

While the tally results for the entire foil pack over time did not come as close as the individual foil results, they provided closer results in the form of STAYSL-adjusted energy spectra once they were unfolded by that software suite. As seen in

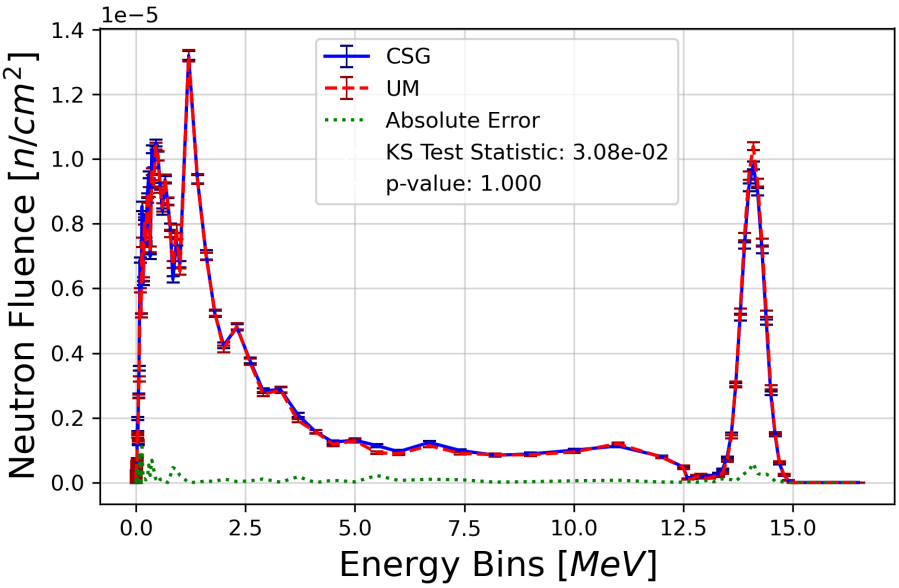


Figure 18: Comparison of the volumetric neutron flux tallies for the CSG and hybrid geometry models of the first gold foil in the ATHENA-I assembly. This foil is the one closest to the tip of the assembly where incident fusion neutrons enter. While this model did not focus on achieving acceptable relative tally errors, it did focus on maintaining consistency between the CSG and UM models instead. As determined by the two-sample K-S test, these results are in statistical agreement.

Figure 20, these spectra generally agree with each other, as the K-S test suggests that the distributions are the same via a p-value of approximately 1.

In addition to providing unfolded spectrum data using both model results as inputs, STAYSL also compared each model's unfolded spectrum to the experimentally-determined spectrum and found normalized $\chi^2$ values of about 1.445 and 1.438 for the CSG and hybrid geometry models respectively.

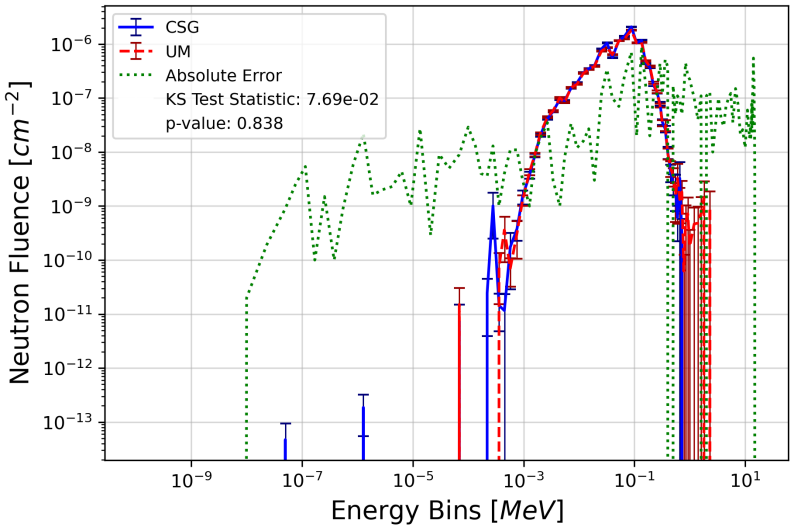


Figure 19: Comparison of volumetric neutron flux tallies for the CSG and hybrid geometry models of the entire ATHENA-I foil pack averaged over all time bins on a logarithmic scale. While not as close as the results for each of the foils individually, the K-S test still suggested that the distributions of the results for the CSG and hybrid geometry models were similar. For results from each individual time bin, see Appendix B.

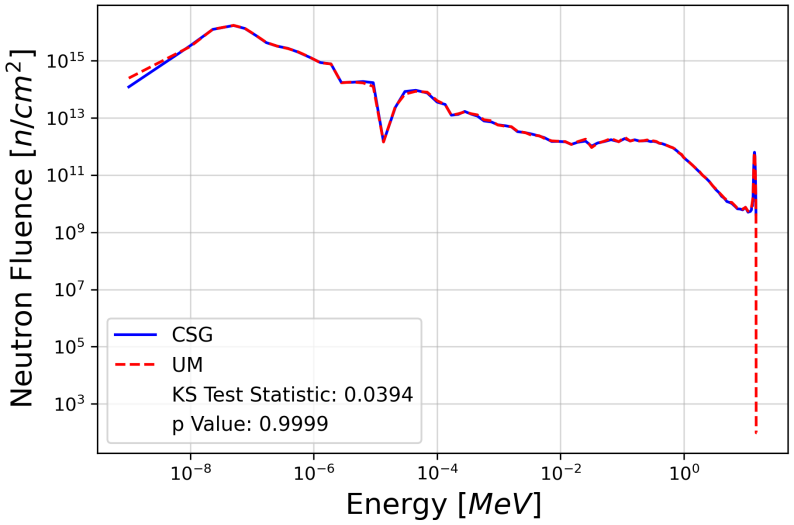


Figure 20: Comparison of the unfolded neutron energy spectra results in STAYSL using the foil pack tallies from both the CSG and hybrid geometry models. According to the K-S test with its p-value of approximately 1, there is general agreement between these sets of results.

### 4.3 Deformed Geometry Test Case Results

For the deformed geometry test case, the average runtime for the measurements was about 6640 seconds, a slightly larger value than the calculated time value (6280 seconds) from Chapter III. This calculated value, however, was determined without accounting for uncertainties of each variable in Eq. 9. When applying a combination of uncertainties from Table 4, a maximum calculated time of 6890 seconds results, a value larger than the aforementioned observed average runtime. Thus, the uncertainty model appears to be validated. Next, the measured experimental data was compared to the tally results of TET and HEX UM models with each having separate uniform density and varied density versions. The observed net count rates from the 662 keV photopeaks were compared to the F8 pulse height tally values from the MCNP outputs (see Fig. 21) as well as the same tally results normalized by the average net count rate (see Fig. 22.

Based on a two-sample K-S test that provided a test statistic and p-value of 0.333 and 0.931, respectively, the normalized model results and experimental data were found to feature the same distribution within a 95% confidence interval. Relative to the measured net count rates, the model results differed by 0.39 - 1.30% with the varied density models (both TET and HEX) being slightly closer to the measurements than their uniform density counterparts (see Table 5). These differences, however, were not statistically significant due to the relative errors of about 1% associated with these tallies.

Beyond validation, the tally results from each UM MCNP model were also compared to each other (see Fig. 23). When using the K-S test to determine whether the homogeneous TET and HEX models featured the same distribution of results, a test statistic and p-value of approximately 0.333 and 0.931, respectively, were again found. When comparing the varied density models with this statistical test, the same

Table 5: Relative Percent Differences between Model Results and Experimental Data

| **Detector Position** | **Homogeneous TET Model** | **Varied Density TET Model** | **Homogeneous HEX Model** | **Varied Density HEX Model** |
|---|---|---|---|---|
| 1 (Top) | 0.39 | 1.08 | 0.39 | 1.08 |
| 2 | 0.69 | 1.03 | 0.69 | 1.03 |
| 3 | 1.30 | 1.01 | 1.30 | 1.01 |
| 4 | 1.20 | 1.04 | 1.20 | 1.05 |
| 5 | 0.78 | 1.06 | 0.78 | 1.03 |
| 6 (Bottom) | 0.91 | 1.08 | 0.91 | 1.10 |

values of 0.333 and 0.931 were calculated. Given the low test statistics and p-values close to unity, statistical agreement was found between the TET and HEX model results.

Comparing the runtimes for the MCNP models, each of them processed relatively high numbers of particle histories per minute. The uniform density TET and HEX models ran $2.496 \times 10^5$ and $1.903 \times 10^5$ histories per minute respectively. This discrepancy makes sense, as the UM for the HEX model featured 447,361 elements rather than 219,310 like the TET model. These models were slightly slower than their varied density counterparts. While they featured the same number of elements, these TET and HEX models instead ran $2.655 \times 10^5$ and $2.051 \times 10^5$ histories per minute respectively.

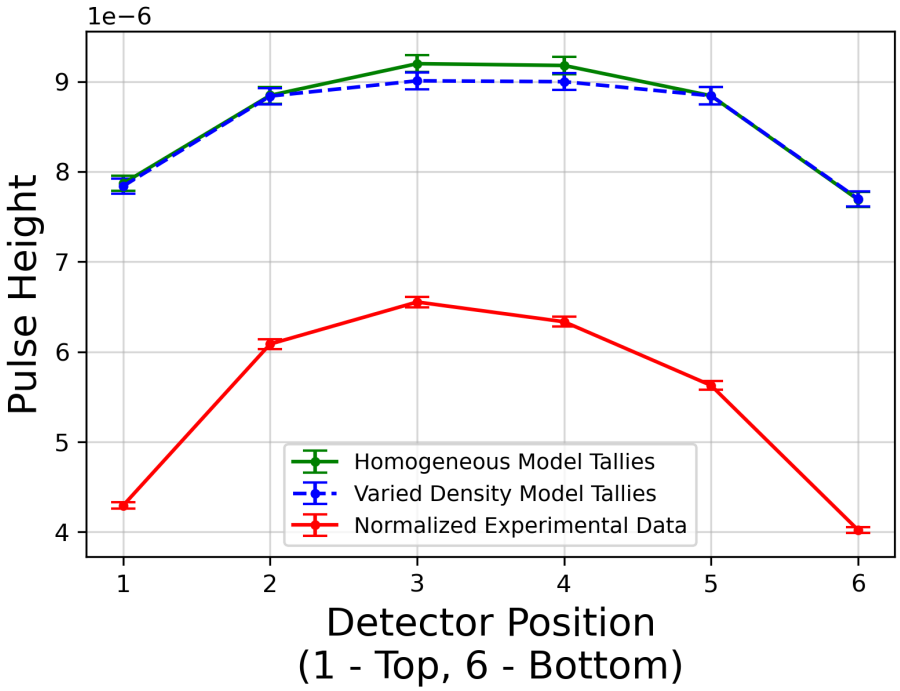


(a) TET model comparison

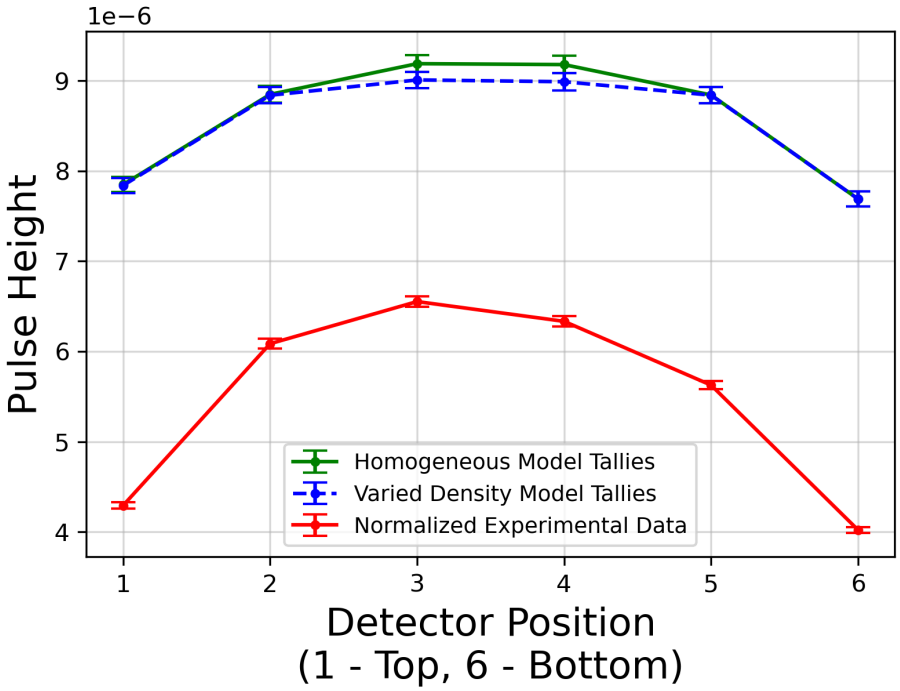


(b) HEX model comparison

Figure 21: Direct comparison of the measured net count rates to (a) TET and (b) HEX UM model F8 tallies. Detector positions, 1 and 6 correspond to the top and bottom of the plate, respectively.

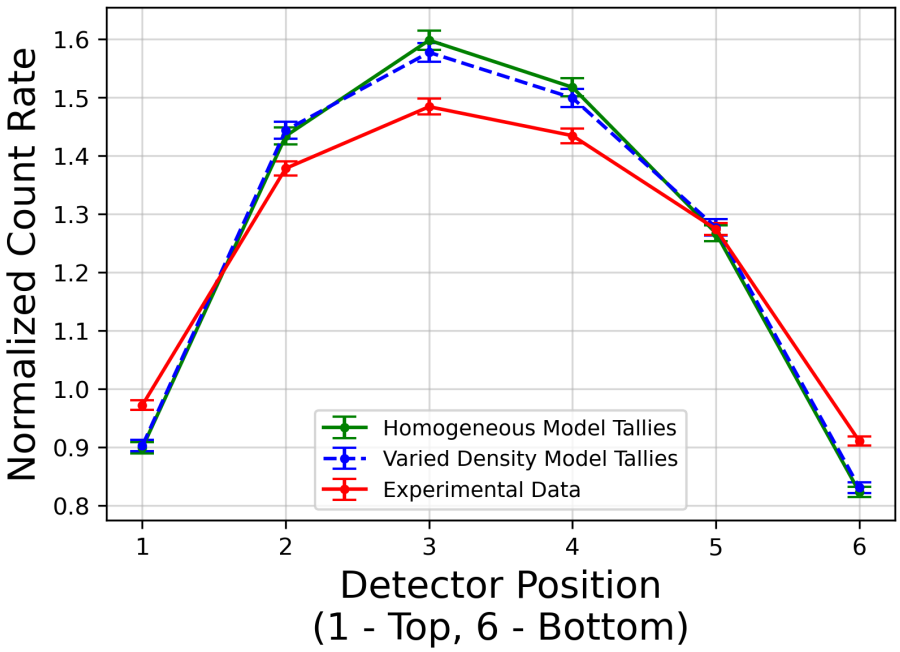


(a) TET model comparison

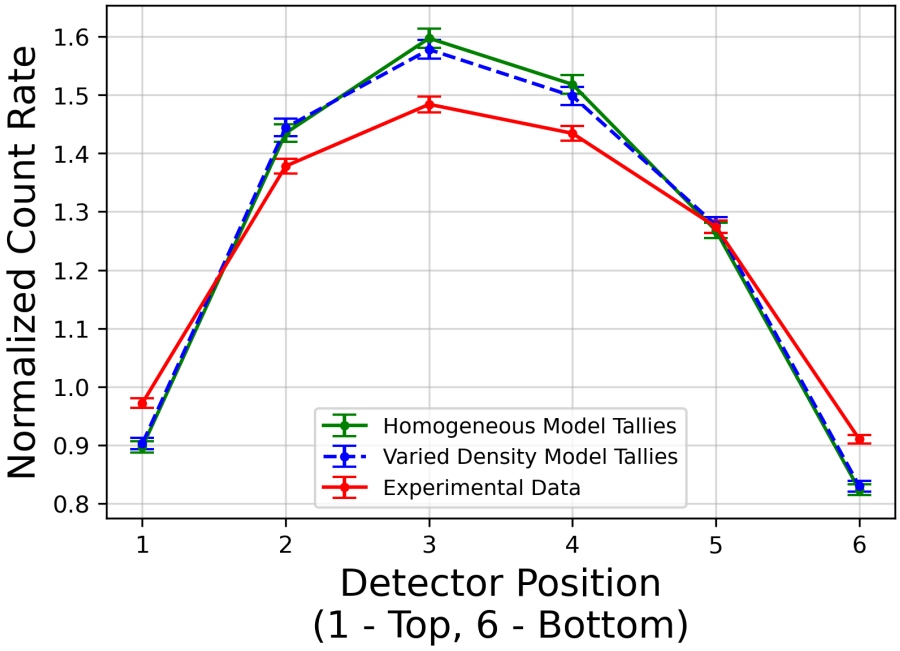


(b) HEX model comparison

Figure 22: Comparison of the measured net count rates to (a) TET and (b) HEX UM model F8 tallies normalized by the average net count rate. Detector positions, 1 and 6 correspond to the top and bottom of the plate, respectively.

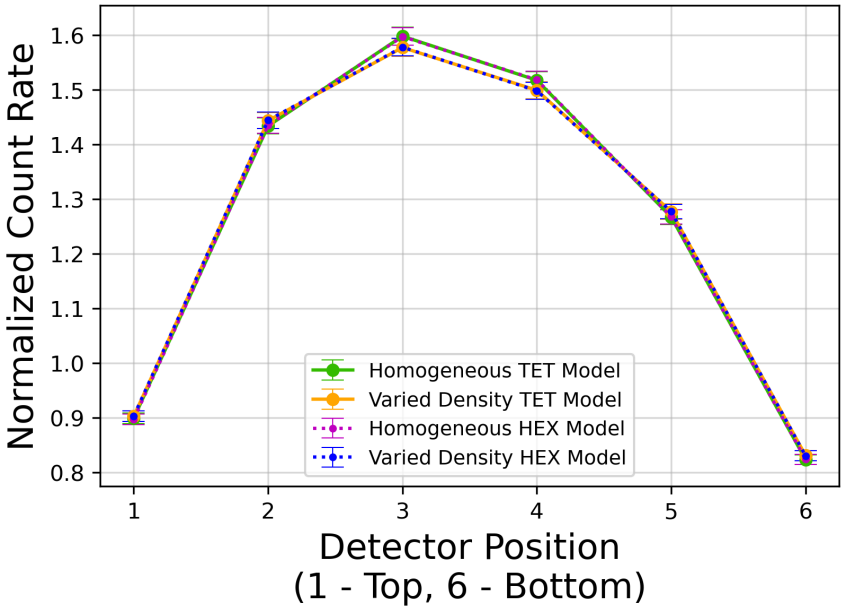


Figure 23: Comparison of the deformed plate MCNP model results with F8 pulse height tally relative errors.

## 4.4 Uncertainties in Modeling and Simulation

While not characterized as thoroughly as the uncertainties found throughout the experimental process, the computational models also have many sources of uncertainty. In the case of MCNP and Monte Carlo methods as a whole, all results feature inherent uncertainties that vary proportional to how many particles are simulated to achieve the results. In addition to this, more uncertainty can be caused by the interplay between MCNP and embedded UM models derived from other software such as CUBIT or Abaqus/CAE.

In terms of meshing, the approximation of problem geometry volumes can introduce additional uncertainty. This effect can be exacerbated if volumes that are key to simulating physics of interest are modeled too coarsely. This is the reason why the ATHENA-I UM model was developed using a biased meshing scheme that meshed the outer shell of the assembly more coarsely and strove to preserve the curvatures of the foils inside the assembly. This was also applied to the UM models for the deformed geometry test case by using finer meshes to represent the button source, plate, and CZT detector geometries.

The deformed geometry test case also featured yet another source of uncertainty in the FEA calculations of Abaqus 2020. While a mesh representation of the deformed copper plate used in this test case's experiment was successfully created with this software, there was no guarantee that the deformed model featured the exact same distribution of local density changes as the actual plate. To determine the exact changes throughout the model, cross-sectional analyses of nodal displacements could be studied, but this could not be done for a physical deformed material. As such, this uncertainty had to be mitigated by modeling the system from the actual plate's deformation as closely as possible.

# V. Conclusions

The ATHENA-I experiment and the deformed geometry shielding experiment test cases were designed to cover new ground and elaborate upon the current benchmarks seen within the MCNP test suite. These models provided insight into radiation transport problems of interest within the MCNP user community that have not been fully explored yet. For the deformed geometry test case, a Python script was written to discretize deformed UM models by density to achieve more accurate results in MCNP. Despite not achieving benchmark quality, this script and the models for the aforementioned test cases provide a foundation and a clear path forward for further V&V efforts of UMs in MCNP.

Regarding a repeatable methodology for V&V of UM capabilities, the development of these two test cases served to highlight several important steps in that process. To properly begin the V&V process, a test case or benchmark candidate must address an area of need or interest amongst the MCNP user community by either expanding the test suite with a new application of UM modeling or elaborating upon a preexisting benchmark. Furthermore, the process should feature models and an experiment with as few sources of uncertainty as possible to ensure a direct and definitive comparison of results. Lastly, the thorough parameterization of geometry types, meshing schemes, and possibly code version is vital for ensuring that a candidate test case achieves the same robustness and quality of previous UM benchmarks.

While tangential to the aforementioned research objectives, another novel contribution of this research was the development of a Notepad++ MCNP syntax highlighting tool [51]. This open-source tool serves to increase the ease of writing MCNP input decks on Windows-based machines, and by proxy, helps with the development of test cases throughout the V&V process.

## 5.1 Future Work for ATHENA-I Test Case

While the test case developed for the ATHENA-I experiment proved to be successful in demonstrating MCNP6's ability to accurately model neutron transport through UM geometries, it has plenty of potential to be expanded upon. The original CSG model of the ATHENA assembly that the UM model was adapted from featured tallies for photons and electrons in addition to neutrons, but these were removed from the UM model due to the amount of computational resources required to achieve statistically meaningful results for these tallies. Due to the longer runtimes of UM models than their CSG counterparts, the number of source histories had to be reduced from $10^{10}$ to $10^{7}$ to be run without access to HPC systems. As such, running the ATHENA-I UM model again with a higher number of source histories would allow for the verification of photon flux and electron energy deposition tallies, the latter has the potential to serve as the basis for a future test case or benchmark as discussed in Chapter II.

Beyond factoring in the transport of photons and electrons, another improvement to be made to the ATHENA-I test case is the use and subsequent analysis of other mesh variants in the assembly geometry. As it stands, the test case only uses a first-order TET mesh to represent the ATHENA assembly, but the inclusions of a first-order HEX mesh, second-order TET mesh, and second-order HEX mesh would allow for a higher-fidelity verification study that more closely resembles the UM benchmarks seen within the current MCNP test suite. Also, the current test case only uses an UM representation of the tuning assembly geometry rather than the entire NIF experimental chamber, so another possible expansion of the model would be to recreate the rest of the facility using UMs as well and produce pure UM models rather than just hybrid models. This change would likely not have a substantial impact on the tally results due to the physics of interest in the experiment being

focused on the activation foils and TLDs in the drawer of the assembly, but it would surely facilitate a more in-depth study of computational resource requirements for UM models relative to CSGs.

The model developed for this test case was run using version 6.2 of MCNP, but as of the writing of this document, the code's development team at LANL is now preparing for a new public release of MCNP. Running the model again in a newer version would add yet another layer to this test case's verification study. While all previous iterations of MCNP6 could only process UM geometries embedded as Abaqus input decks, the development version of MCNP would allow for alternative meshes for the ATHENA-I geometry to be embedded in an HDF5 format instead [11]. Given the model's various particle's of interest and its complex geometry, this change would allow for an ample comparison of MCNP's efficiency processing UMs in both file formats.

### 5.2 Future Work for Deformed Geometry Test Case

Like the ATHENA-I test case, the deformed geometry test case also has potential to be elaborated upon. One possible addition to this test case could be the use of the detector raster assembly to take measurements in the rest of the positions within its 6 x 6 array. This system would provide much more spatial information regarding the density changes' effects on the attenuation of incident photons. Another benefit is that the system would allow other plates with different shapes and deformation severity to be more easily measured. With various types of deformation, many different density gradients could be observed, and the assumption that densities in deformed geometries can be averaged out could be parameterized and studied.

Before taking more measurements with this same experimental configuration, however, simplifying the experiment to just a detector and source would help to root out

any potential issues with the measurements that could have led to the discrepancies in results seen previously in Chapter IV. From there, the experimental setup could be iterated upon by taking another set of measurements in each position now with an undeformed copper plate. This would provide a control in the experiment to consider relative to the deformed plate setup that was used here.

Regarding the simulation of this experiment, the *UM_vardens.py* density binning script used throughout this research could be expanded upon and improved greatly. Additionally, it could be used even in its current form to further discretize the plate models following deformation simulations in Abaqus. This would allow for more in-depth parameter study on the effects of the density binning process and its accuracy in reflecting physical results. In terms of meshing, other schemes and element types could be used for additional models of the plate and experimental setup. Aside from refining the meshes to raise or lower element counts, second order TET and HEX models could also be used to further analyze computational resource requirements.

Regarding the modeling of this test case in MCNP, several more changes could be made. One modification to models could be the increase of the number of source particles run. This would lower the uncertainties of the pulse height tally results and allow for a better comparison with the experimental data. Additionally, since these models were analog and did not utilize variance reduction techniques, the models could be adapted to actually use variance reduction in order to determine how that affects runtimes for UM models.

This test case's models could also be expanded to highlight new features within the most recent versions of MCNP. Like the ATHENA-I test case, these deformed geometry models made use of UMs formatted as Abaqus input decks, but the UMs could be recreated in the HDF5 format to facilitate verification of UM model runtimes based on file type in the development version of MCNP. Additionally, given the

prismatic shape of the detector mesh in these models, a comparison between the legacy FMESH4 tallies and the new but analogous EMBEE4 feature could be made readily.

# Appendix A. Repository of Models, Scripts, and Other Files

To maximize reproducibility, all of the MCNP models, Abaqus input decks, Python scripts and other miscellaneous files presented throughout this research can be found in a publicly available online repository at `https://github.com/mjeroutek/MCNP-UM-V-V-Research/`. These models and files are organized in folders based on the test case developed within this research that they are associated with.

# Appendix B. Additional ATHENA-I Model Figures

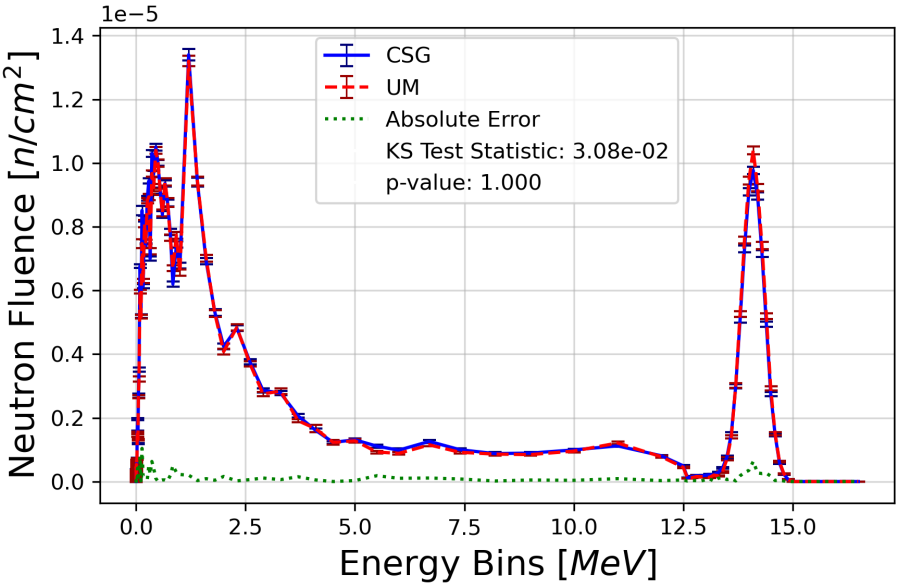


Figure 24: Comparison of the volumetric neutron fluence tallies for the CSG and hybrid geometry models of the nickel foil in the ATHENA-I assembly.

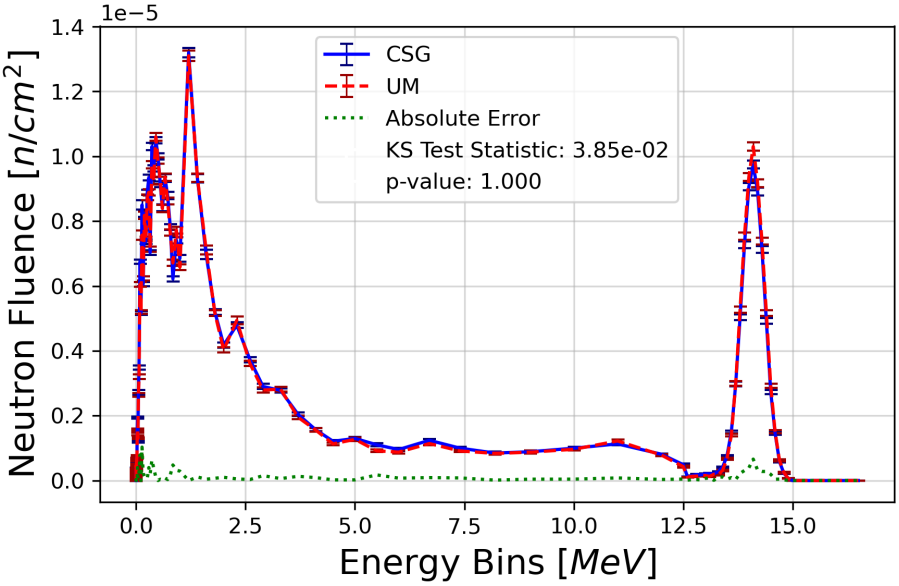


Figure 25: Comparison of the volumetric neutron fluence tallies for the CSG and hybrid geometry models of the indium foil in the ATHENA-I assembly.

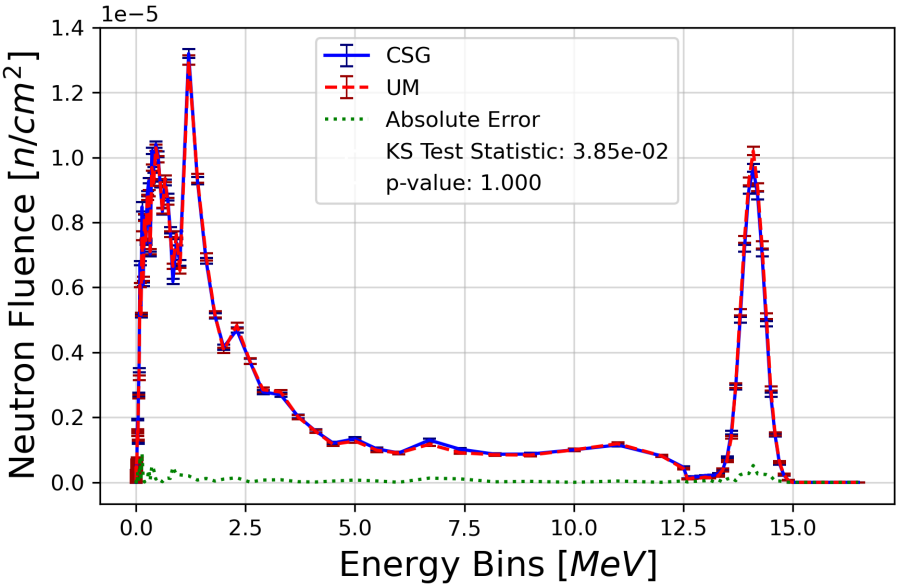


Figure 26: Comparison of the volumetric neutron fluence tallies for the CSG and hybrid geometry models of the aluminum foil in the ATHENA-I assembly.

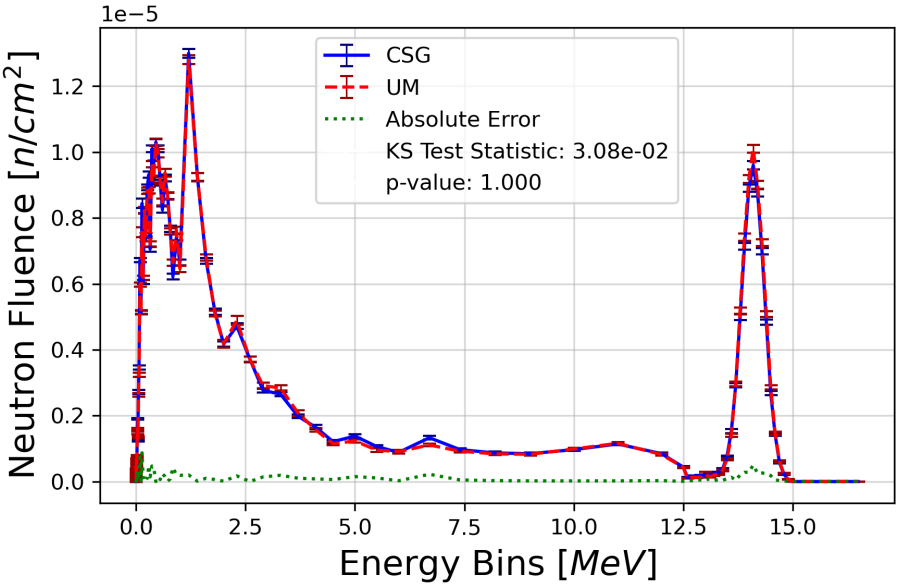


Figure 27: Comparison of the volumetric neutron fluence tallies for the CSG and hybrid geometry models of the titanium foil in the ATHENA-I assembly.

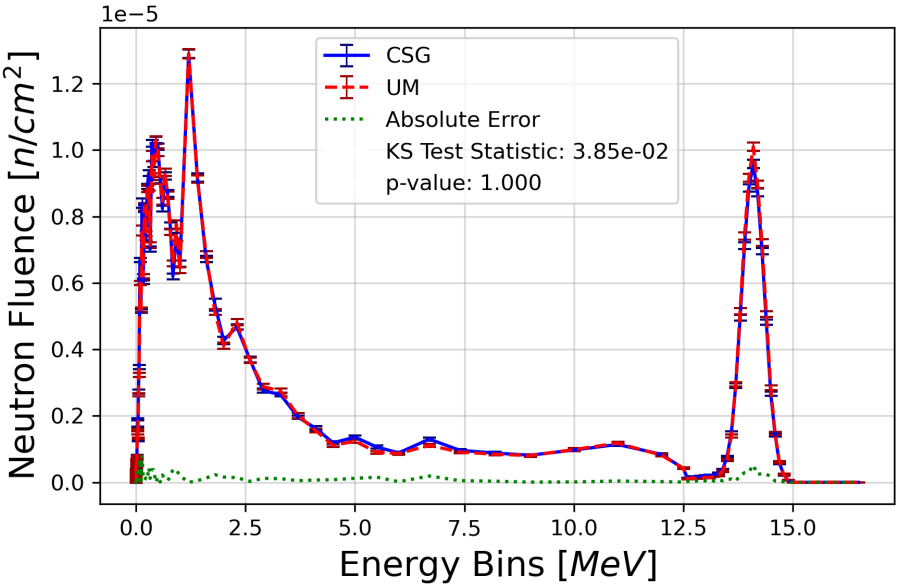


Figure 28: Comparison of the volumetric neutron fluence tallies for the CSG and hybrid geometry models of the tungsten foil in the ATHENA-I assembly.

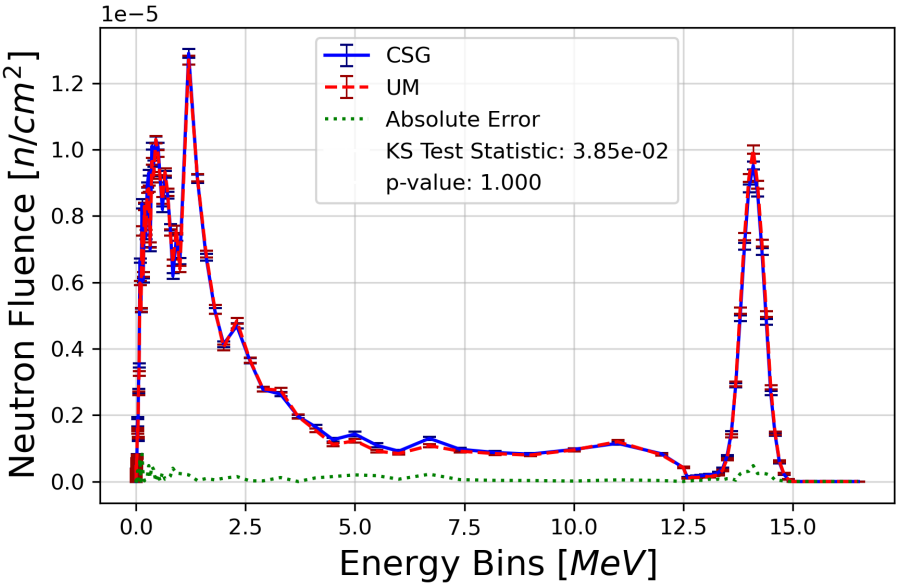


Figure 29: Comparison of the volumetric neutron fluence tallies for the CSG and hybrid geometry models of the zirconium foil in the ATHENA-I assembly.

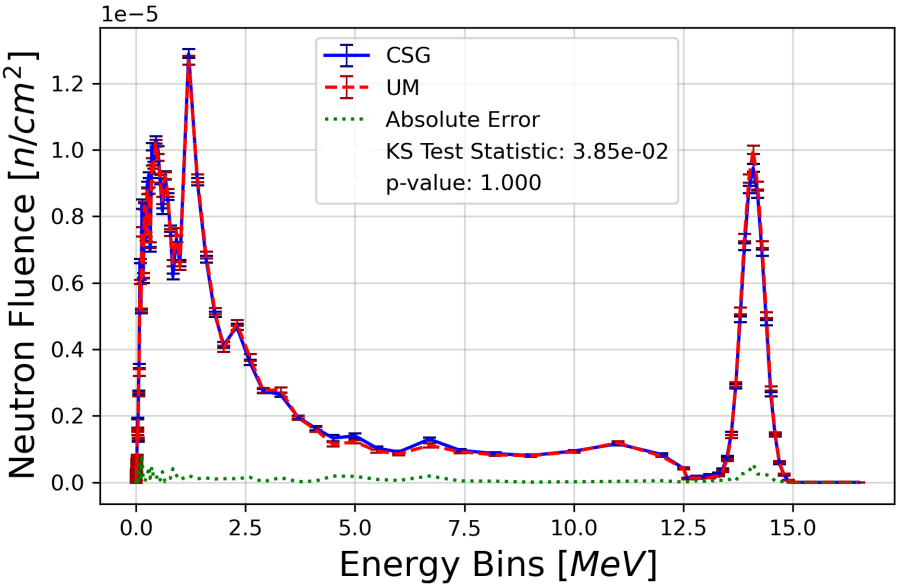


Figure 30: Comparison of the volumetric neutron fluence tallies for the CSG and hybrid geometry models of the magnesium foil in the ATHENA-I assembly.

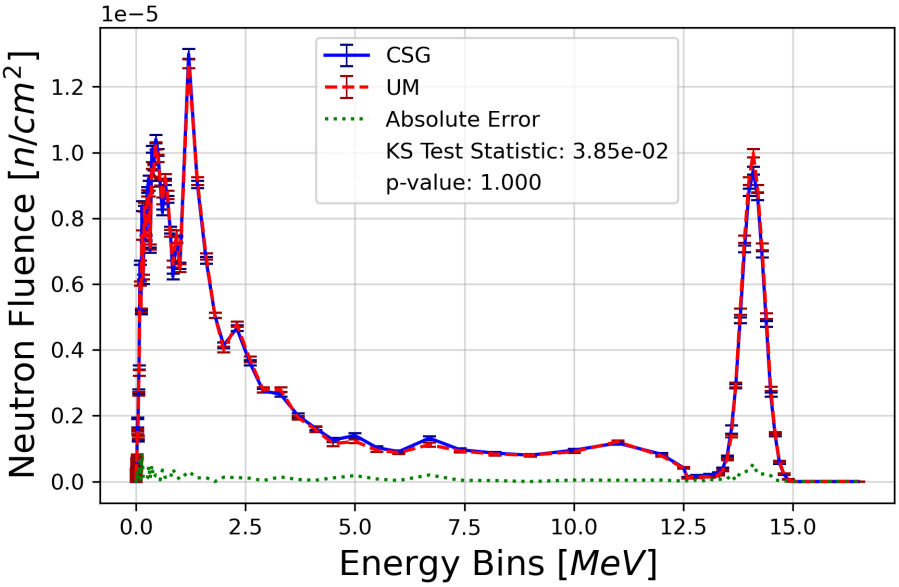


Figure 31: Comparison of the volumetric neutron fluence tallies for the CSG and hybrid geometry models of the second gold foil in the ATHENA-I assembly.

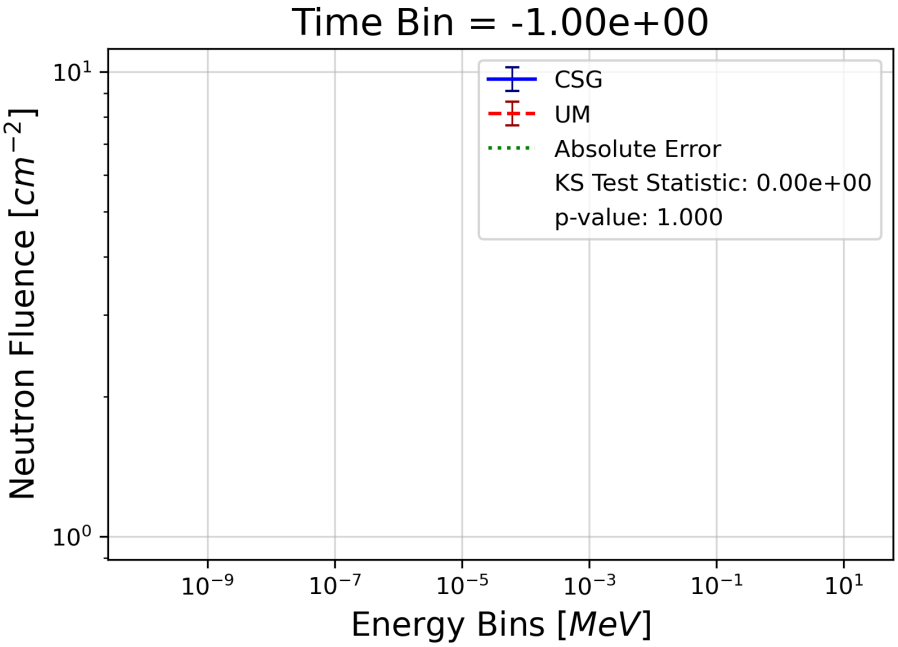


Figure 32: Comparison of the volumetric neutron fluence tallies for the CSG and hybrid geometry models of the entire ATHENA-I assembly during the initial time bin.

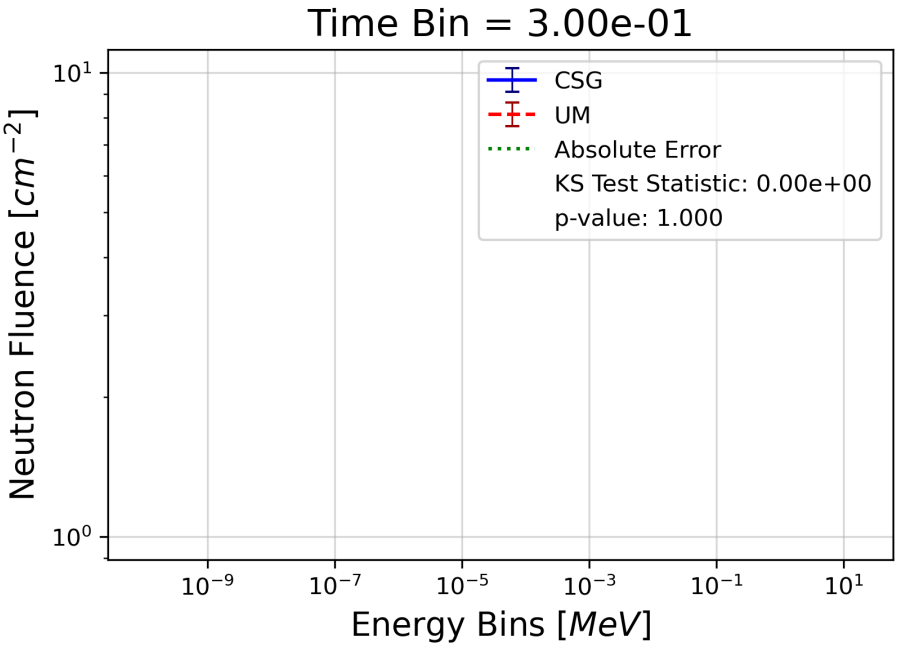


Figure 33: Comparison of the volumetric neutron fluence tallies for the CSG and hybrid geometry models of the entire ATHENA-I assembly during the 2nd time bin.

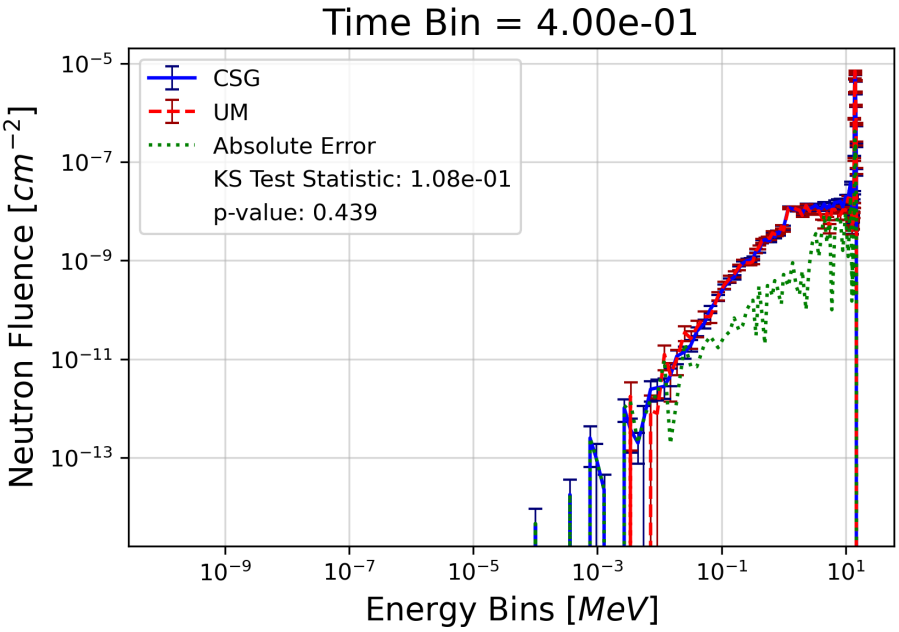


Figure 34: Comparison of the volumetric neutron fluence tallies for the CSG and hybrid geometry models of the entire ATHENA-I assembly during the 3rd time bin.

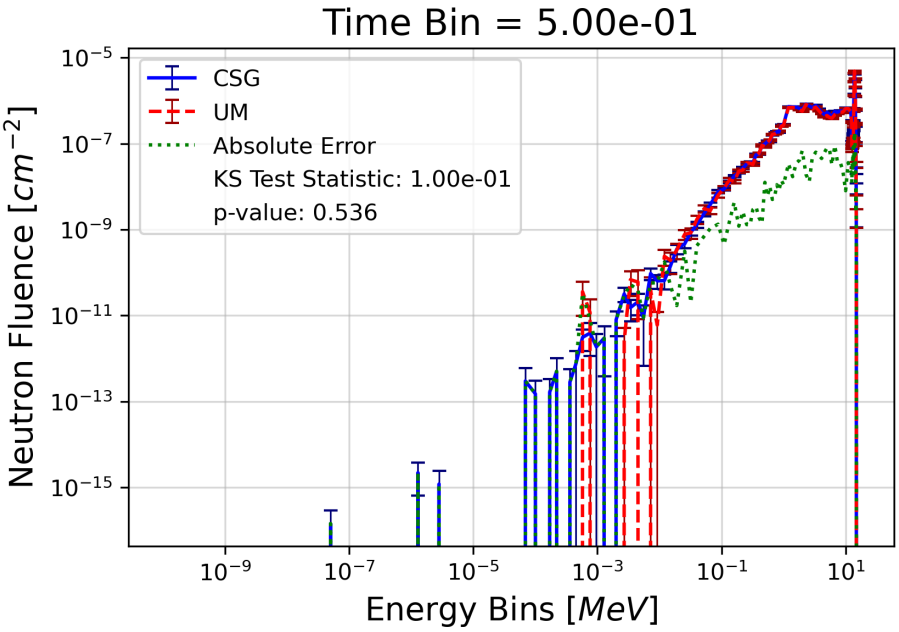


Figure 35: Comparison of the volumetric neutron fluence tallies for the CSG and hybrid geometry models of the entire ATHENA-I assembly during the 4th time bin.

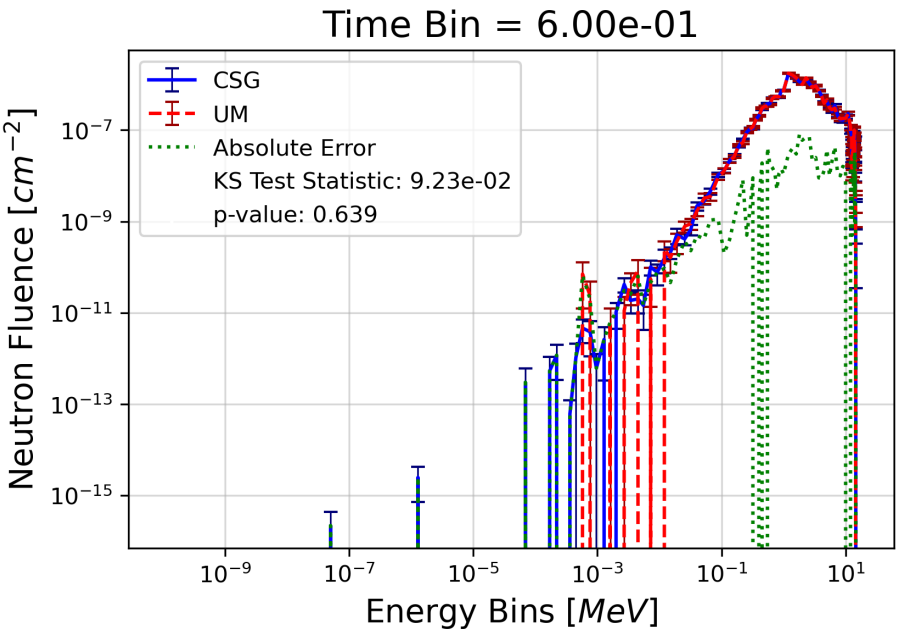


Figure 36: Comparison of the volumetric neutron fluence tallies for the CSG and hybrid geometry models of the entire ATHENA-I assembly during the 5th time bin.

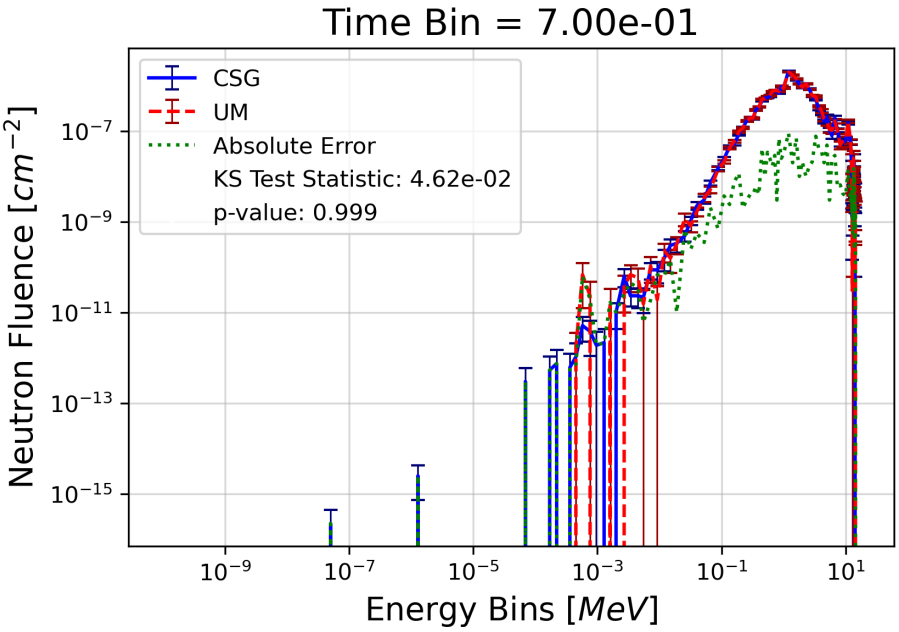


Figure 37: Comparison of the volumetric neutron fluence tallies for the CSG and hybrid geometry models of the entire ATHENA-I assembly during the 6th time bin.

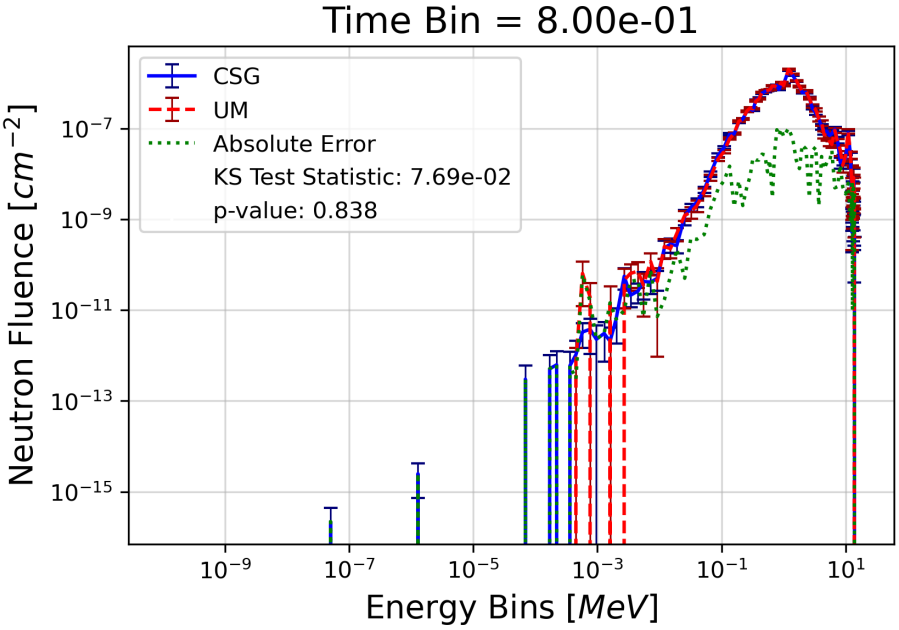


Figure 38: Comparison of the volumetric neutron fluence tallies for the CSG and hybrid geometry models of the entire ATHENA-I assembly during the 7th time bin.

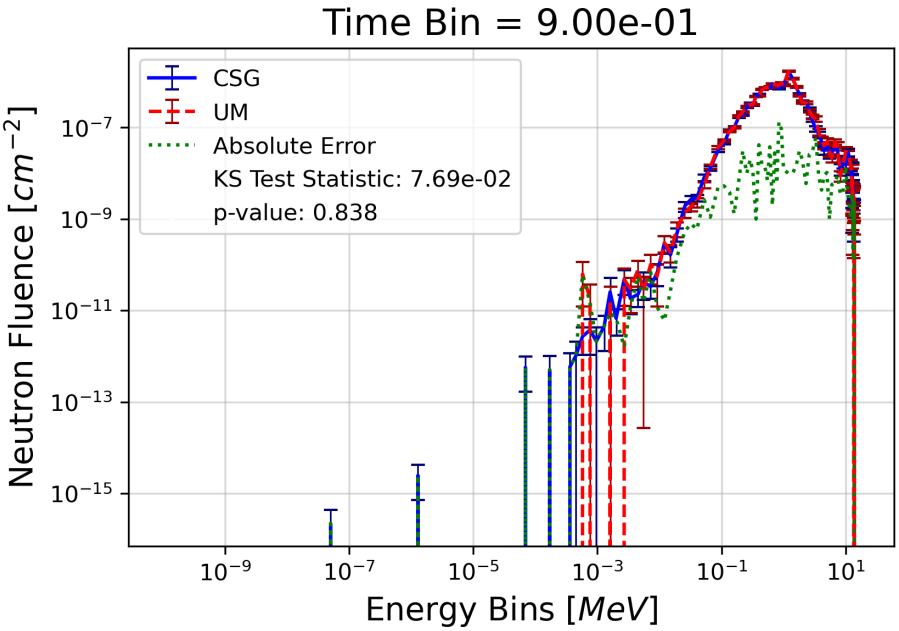


Figure 39: Comparison of the volumetric neutron fluence tallies for the CSG and hybrid geometry models of the entire ATHENA-I assembly during the 8th time bin.

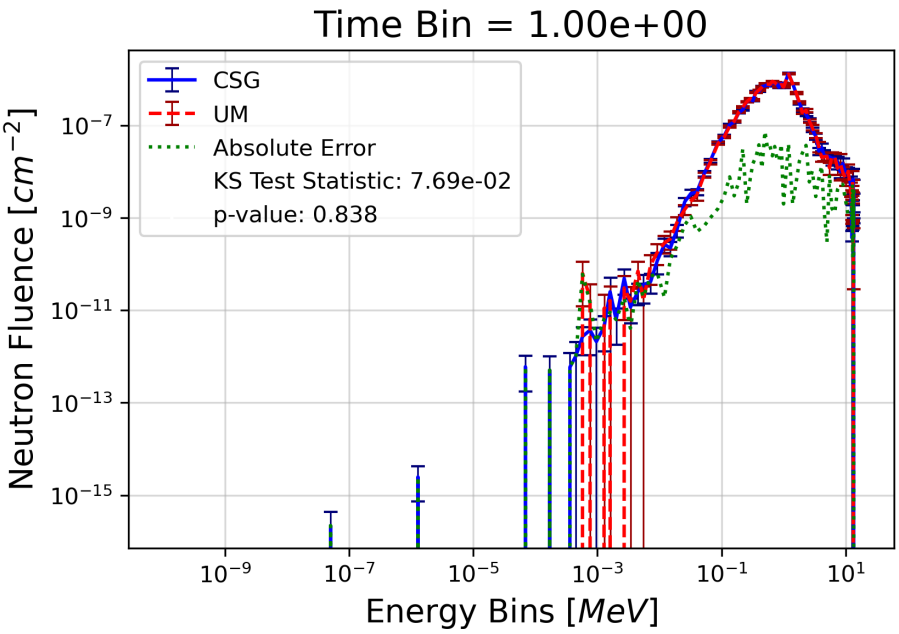


Figure 40: Comparison of the volumetric neutron fluence tallies for the CSG and hybrid geometry models of the entire ATHENA-I assembly during the 9th time bin.

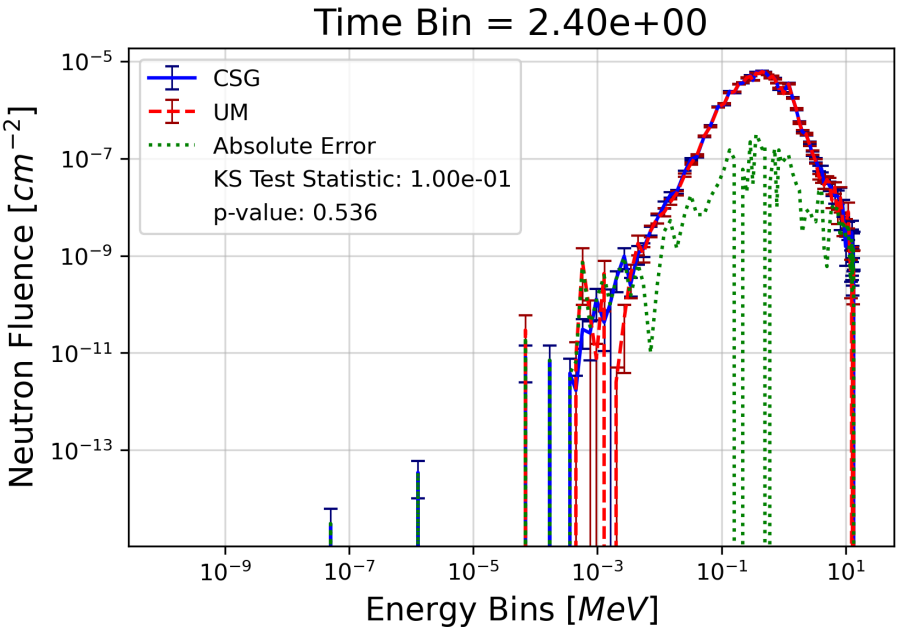


Figure 41: Comparison of the volumetric neutron fluence tallies for the CSG and hybrid geometry models of the entire ATHENA-I assembly during the 10th time bin.

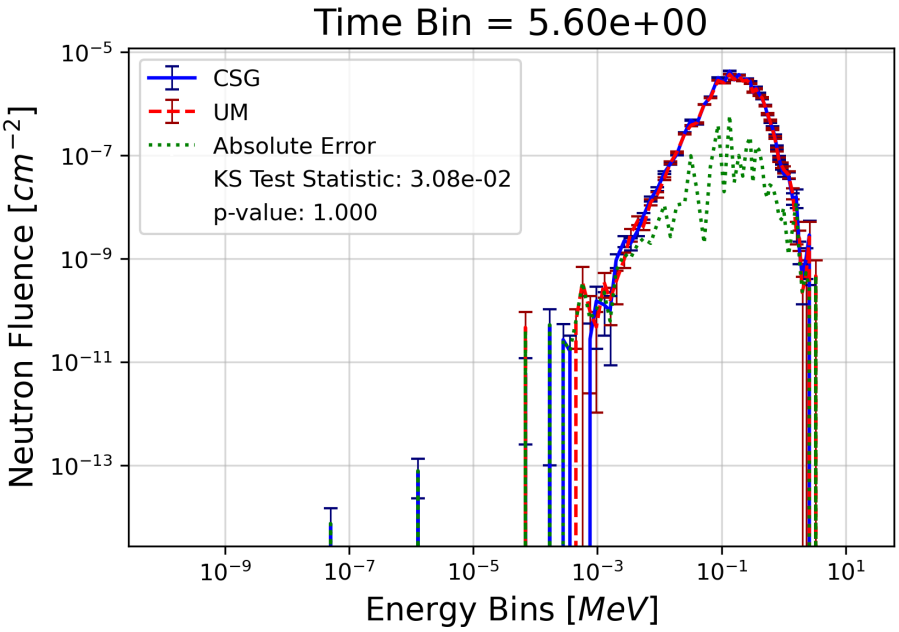


Figure 42: Comparison of the volumetric neutron fluence tallies for the CSG and hybrid geometry models of the entire ATHENA-I assembly during the 11th time bin.

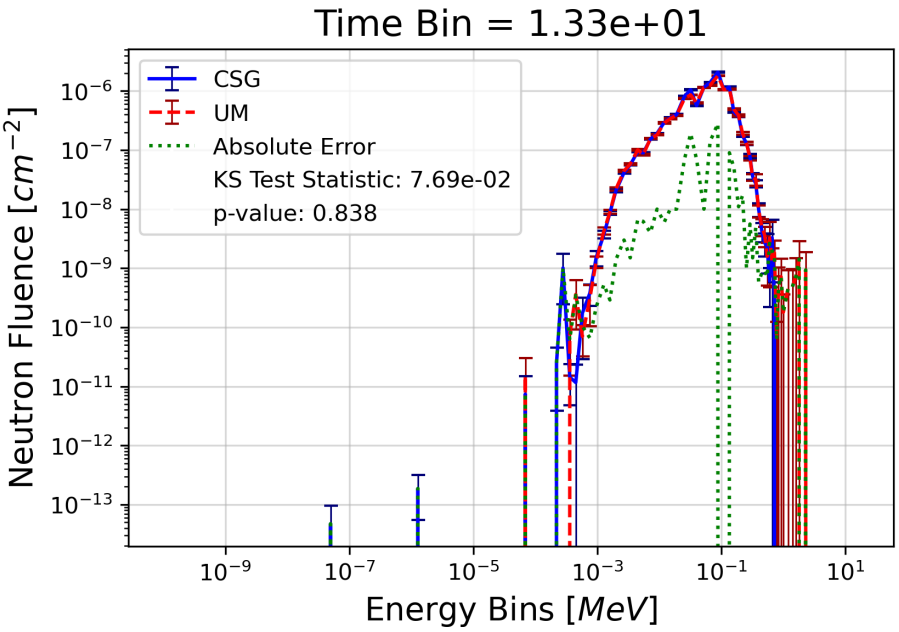


Figure 43: Comparison of the volumetric neutron fluence tallies for the CSG and hybrid geometry models of the entire ATHENA-I assembly during the 12th time bin.

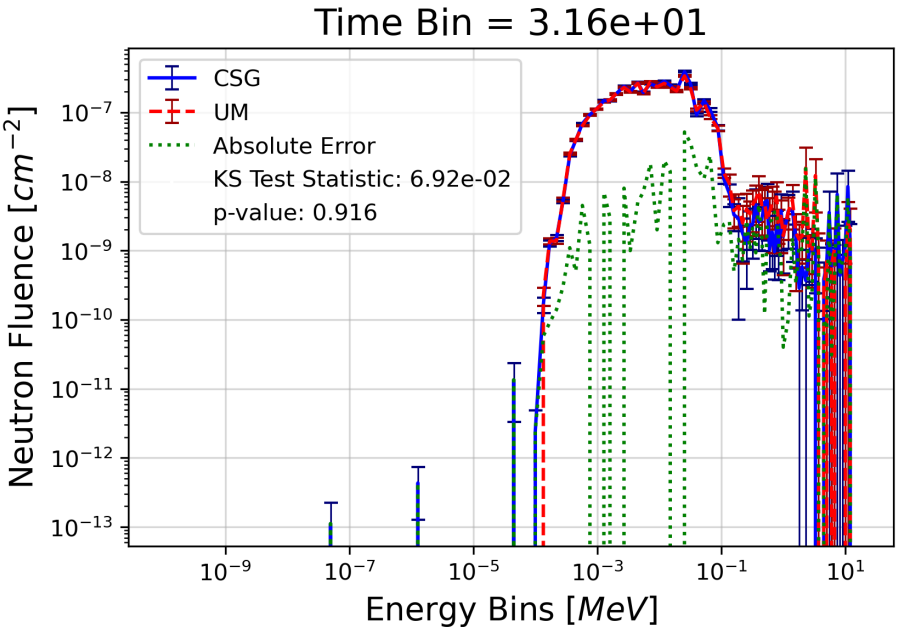


Figure 44: Comparison of the volumetric neutron fluence tallies for the CSG and hybrid geometry models of the entire ATHENA-I assembly during the 13th time bin.

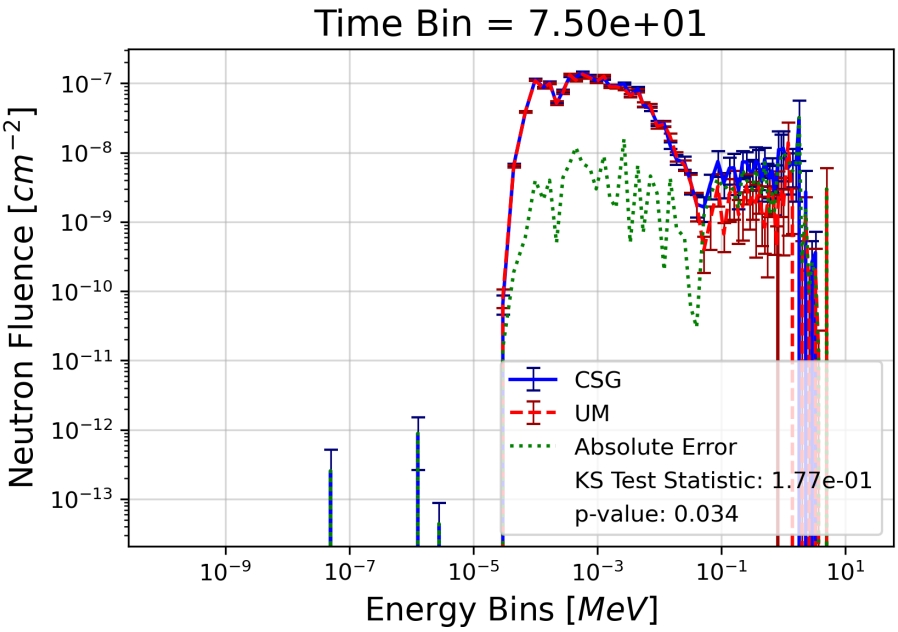


Figure 45: Comparison of the volumetric neutron fluence tallies for the CSG and hybrid geometry models of the entire ATHENA-I assembly during the 14th time bin.

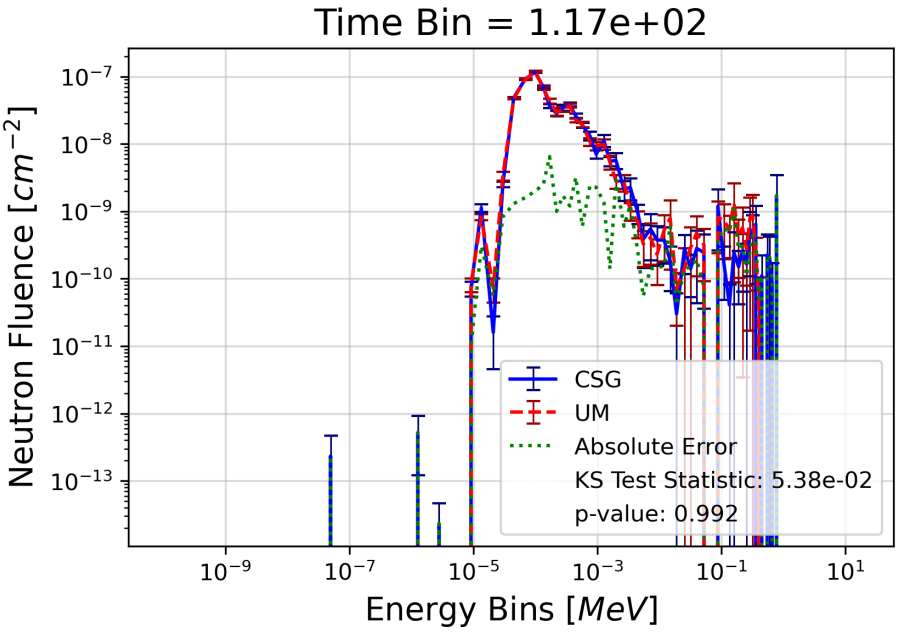


Figure 46: Comparison of the volumetric neutron fluence tallies for the CSG and hybrid geometry models of the entire ATHENA-I assembly during the 15th time bin.

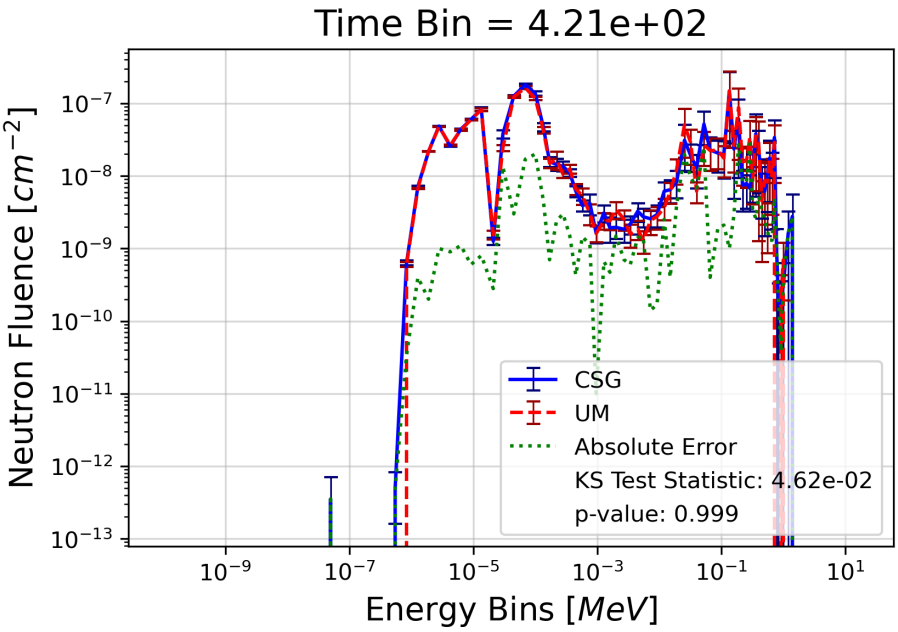


Figure 47: Comparison of the volumetric neutron fluence tallies for the CSG and hybrid geometry models of the entire ATHENA-I assembly during the 16th time bin.

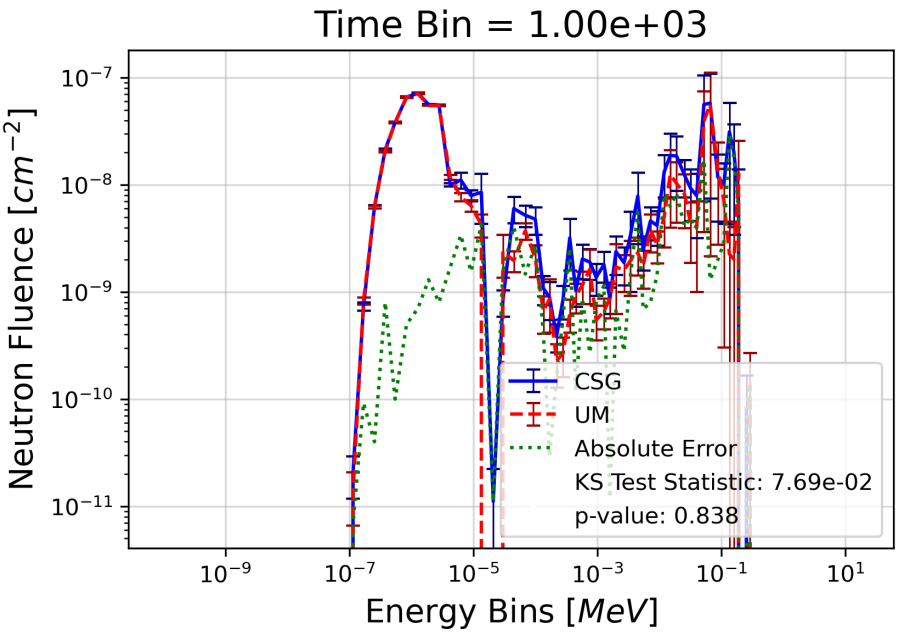


Figure 48: Comparison of the volumetric neutron fluence tallies for the CSG and hybrid geometry models of the entire ATHENA-I assembly during the 17th time bin.

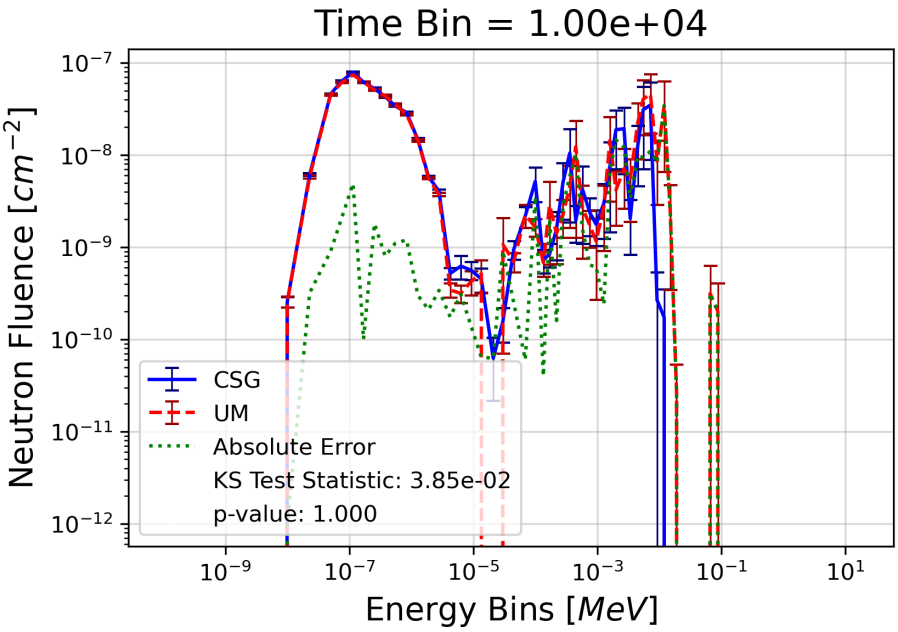


Figure 49: Comparison of the volumetric neutron fluence tallies for the CSG and hybrid geometry models of the entire ATHENA-I assembly during the 18th time bin.

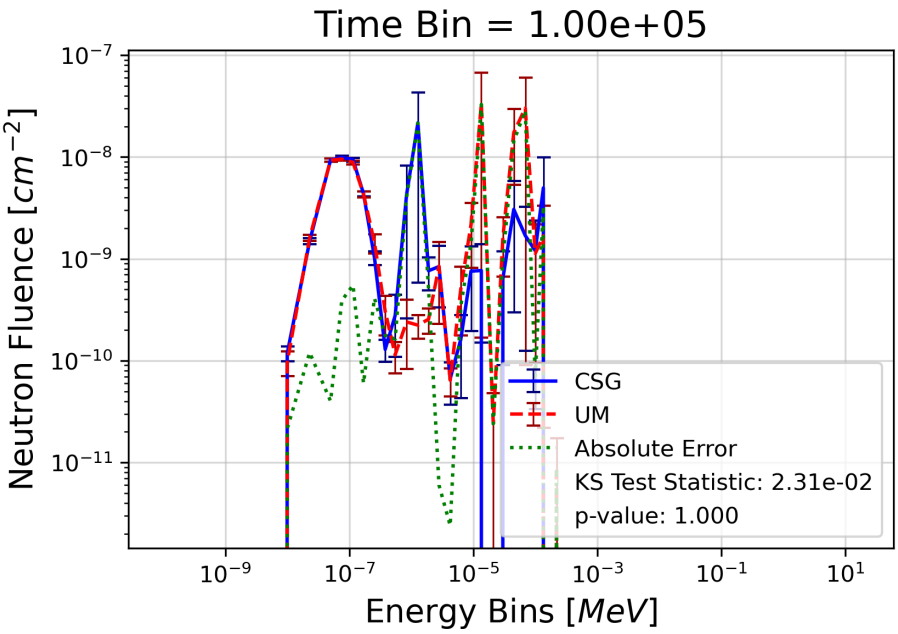


Figure 50: Comparison of the volumetric neutron fluence tallies for the CSG and hybrid geometry models of the entire ATHENA-I assembly during the 19th time bin.

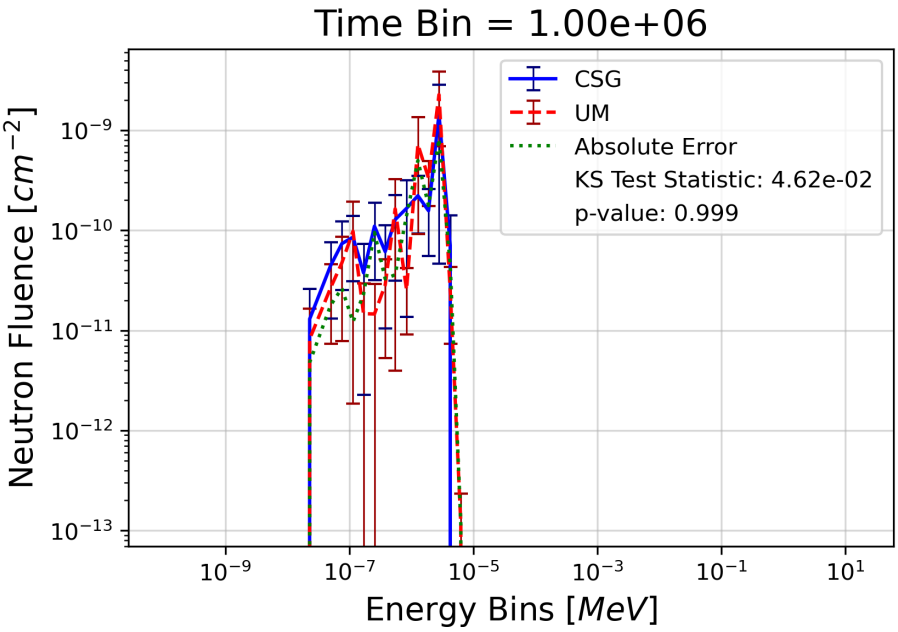


Figure 51: Comparison of the volumetric neutron fluence tallies for the CSG and hybrid geometry models of the entire ATHENA-I assembly during the 20th time bin.

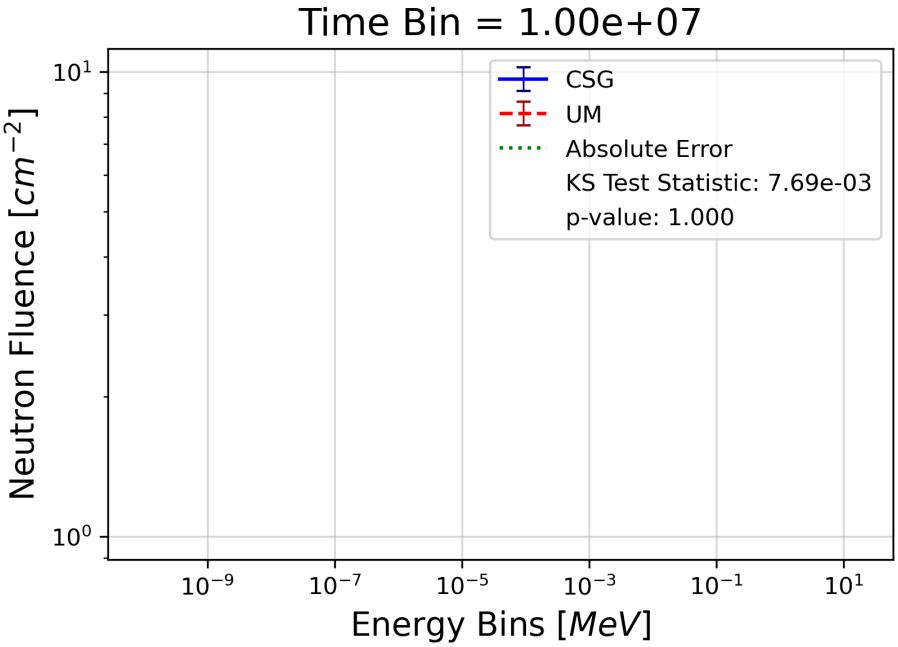


Figure 52: Comparison of the volumetric neutron fluence tallies for the CSG and hybrid geometry models of the entire ATHENA-I assembly during the 21st time bin.

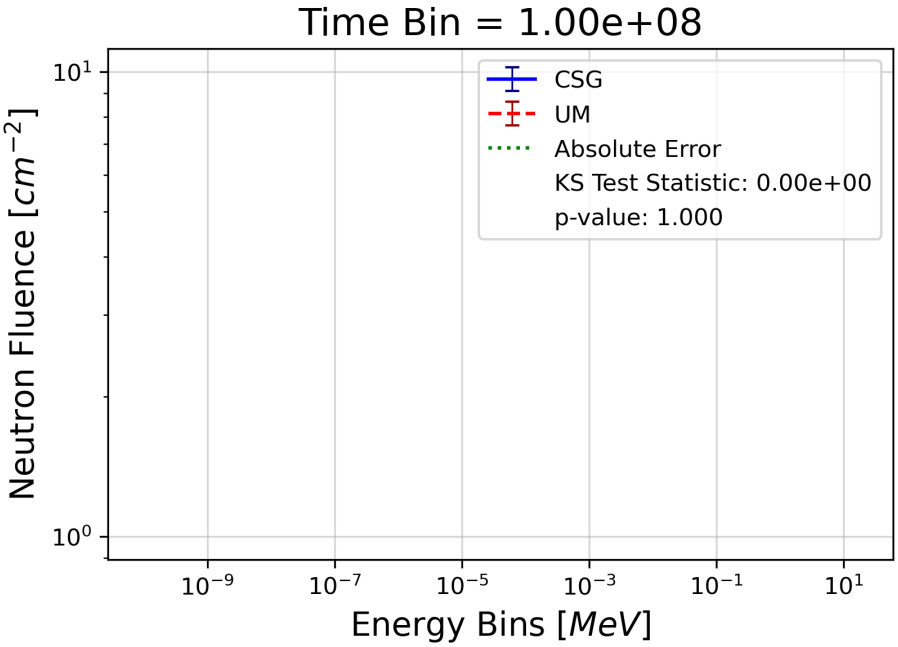


Figure 53: Comparison of the volumetric neutron fluence tallies for the CSG and hybrid geometry models of the entire ATHENA-I assembly during the 22nd and final time bin.

# Appendix C. ATHENA-I CSG Model MCNP Input Deck

```
Athena-I Experiment CSG Model
c ****************************************************************************
c  Cell Cards
c ****************************************************************************
c NIF Chamber
2   131  -0.17826   1 -2               imp:n,p=1 imp:e=0 $ 409 SS Wall
3   126  -0.28178   2 -3               imp:n,p=1 imp:e=0 $ Al Wall and Port Covers
4   136  -0.072047  3 -4               imp:n,p=1 imp:e=0 $ Al FW Wall
5   108  -0.048682  4 -5               imp:n,p=1 imp:e=0 $ I beam and flashing
6   101  -2.7       5 -7               imp:n,p=1 imp:e=0 $ Al Wall
7   102  -2.4249    7 -8               imp:n,p=1 imp:e=0 $ Gunite
8   0               8                  imp:n,p,e=0  $ Kill radius
c
c Athena Body
10  22   -7.87     -10 11 60        imp:n,p=1 imp:e=0 $ Cone
11  23   -7.87     (-12 17):(-18):
                           (-14 12) imp:n,p=1 imp:e=0 $ Cover top
12  22   -7.87     -12 -17 18       imp:n,p=1 imp:e=0 $ Cover bottom
13  23   -7.87     -15              imp:n,p=1 imp:e=0 $ Cover Adapter
14  23   -7.87     -16              imp:n,p=1 imp:e=0 $ Mount
15  8    -1.29e-9  -64              imp:n,p=1 imp:e=0 $ Air fill in drawer handle
19  8    -1.29e-9  -1 10 12 15 16 60 62 63
                   #210 #211 #212 #213 #250 #251 #252 #253
                                    imp:n,p=1 imp:e=0 $ Air fill around Athena
c
c Athena Components
20  3     -6.49   -20               imp:n,p=1 imp:e=0 $ Zr cone
21  4     -18.7   -21               imp:n,p=1 imp:e=0 $ W-1 Cone
22  6     -2.70   -22               imp:n,p=1 imp:e=0 $ Al spacer
23  6     -2.70   -24 23 60 67      imp:n,p=1 imp:e=0 $ Al-6061 ring
24  4     -18.7   -26 25 60 67      imp:n,p=1 imp:e=0 $ W-2
25  6     -2.70   -28 27 60 67      imp:n,p=1 imp:e=0 $ Al-6061 ring
26  6     -2.70   -29 30            imp:n,p=1 imp:e=0 $ Al spacer
27  6     -2.70   -31               imp:n,p=1 imp:e=0 $ Al spacer plug
28  4     -18.7   -32 33            imp:n,p=1 imp:e=0 $ W-3
29  4     -18.7   -34               imp:n,p=1 imp:e=0 $ W-3 plug
30  7     -2.260  -35 36            imp:n,p=1 imp:e=0 $ C
31  7     -2.260  -37               imp:n,p=1 imp:e=0 $ C plug
32  9     -1.400  -38 39            imp:n,p=1 imp:e=0 $ Delrin
33  9     -1.400  -40               imp:n,p=1 imp:e=0 $ Delrin plug
34  10    -1.800  -41               imp:n,p=1 imp:e=0 $ Viton seal
c
c Drawer
40  21    -7.8    (-60:-61) 65 66   imp:n,p=1 imp:e=0 $ Drawer case
41  21    -7.8    -62 10 60         imp:n,p=1 imp:e=0 $ Drawer handle mount
42  21    -7.8    -63 64            imp:n,p=1 imp:e=0 $ Drawer handle
43  4     -19.25  -68 66 69 70      imp:n,p=1 imp:e=0 $ W insert
44  21    -7.8    -69:-70           imp:n,p=1 imp:e=0 $ Screw mounts
45  8     -1.29e-9 (-65:-66) 500 501 502 503 504 505 506 507
                   508 509 #43 69 70  imp:n,p=1 imp:e=0  $ Air
c
c Activation Foils - Ordered closest to TCC
```

```
50  14  -2.70   -500 810 811 812 813 814 815 816 817
                                imp:n,p,e=1  $ Al spacer (Toad option), room for TLDs
51  11  -19.18  -501 502           imp:n,p,e=1        $ Au-1 foil
52  12  -9.019  -502 503           imp:n,p=1 imp:e=0  $ Ni foil
53  13  -6.913  -503 504           imp:n,p=1 imp:e=0  $ In foil
54  14  -2.646  -504 505           imp:n,p=1 imp:e=0  $ Al foil
55  15  -4.303  -505 506           imp:n,p=1 imp:e=0  $ Ti foil
56  16  -18.27  -506 507           imp:n,p=1 imp:e=0  $ W foil
57  17  -5.815  -507 508           imp:n,p=1 imp:e=0  $ Zr foil
58  18  -1.800  -508 509           imp:n,p=1 imp:e=0  $ Mg foil
59  11  -19.19  -509 508           imp:n,p=1 imp:e=0  $ Au-2 foil
c
c TLD 100s
70  8   -1.29e-9   -80             imp:n,p,e=1  $ TLD 100 void
701 8   -1.29e-9   -810 80         imp:n,p,e=1  $ TLD-100 air fill
71  8   -1.29e-9   -81             imp:n,p,e=1  $ TLD 100 void
711 8   -1.29e-9   -811 81         imp:n,p,e=1  $ TLD-100 air fill
72  8   -1.29e-9   -82             imp:n,p,e=1  $ TLD 100 void
721 8   -1.29e-9   -812 82         imp:n,p,e=1  $ TLD-100 air fill
73  8   -1.29e-9   -83             imp:n,p,e=1  $ TLD 100 void
731 8   -1.29e-9   -813 83         imp:n,p,e=1  $ TLD-100 air fill
c
c TLD 400s
74  20  -3.18      -84             imp:n,p,e=1  $ TLD 400
741 8   -1.29e-9   -814 84         imp:n,p,e=1  $ TLD-400 air fill
75  20  -3.18      -85             imp:n,p,e=1  $ TLD 400
751 8   -1.29e-9   -815 85         imp:n,p,e=1  $ TLD-400 air fill
76  20  -3.18      -86             imp:n,p,e=1  $ TLD 400
761 8   -1.29e-9   -816 86         imp:n,p,e=1  $ TLD-400 air fill
77  20  -3.18      -87             imp:n,p,e=1  $ TLD 400
771 8   -1.29e-9   -817 87         imp:n,p,e=1  $ TLD-400 air fill
c Air Fill inside Athena
100   8  -1.29e-9  -11 14 #20 #21 #22 #23 #24 #25 #26 #27 60 61 #28 #29
                 #30 #31 #32 #33 #34 imp:n=1 imp:p=1 imp:e=0 $ Internal air fill
c
c ATHENA Airbox and DIM 90-348
c
250 27  -2.7       -250 251          imp:n,p=1 imp:e=0  $ Airbox
251 27  -2.7       -252 253 257      imp:n,p=1 imp:e=0  $ Airbox Bracket
252 27  -2.7       -254              imp:n,p=1 imp:e=0  $ Bracket
253 27  -2.7       -1 -255 256       imp:n,p=1 imp:e=0  $ DIM
c
c TARPOS on 90-239
210 27  -2.7       -1 -220 221       imp:n,p=1 imp:e=0 $ TARPOS
211 27  -2.7       -222 223          imp:n,p=1 imp:e=0 $ TARPOS
212 27  -2.7       -224 225          imp:n,p=1 imp:e=0 $ TARPOS Snout
213 27  -2.7       -226:-227:-228    imp:n,p=1 imp:e=0 $ TARPOS Snout

c ******************************************************************************
c  Surface Cards
c ******************************************************************************
c NIF surfaces
1  SO    463.316
2  SO    478.416
```

```
3  SO    479.616
4  SO    489.84
5  SO    500
7  SO    510
8  SO    550
c
c Athena body surfaces
10 TRC  9.000 0 0 19.202 0 0 0.855 15.281     $ Outer body Athena
11 TRC  9.700 0 0 18.502 0 0 0.765 14.378     $ Inner body Athena
12 RCC  28.202 0 0 1.3 0 0 16.708             $ Cover
13 PX   28.016                                $ Cover plug
14 RCC  28.016 0 0 1.0 0 0 13.5               $ Cover plug fill
15 RPP  29.502 30.202 -9.1 9.1 -11 11         $ Mount
16 RPP  30.202 31.132 -8.7 8.7 -10.975 10.975 $ Mount
17 PX   28.802                                $ Cover front/back
18 RCC  28.202 0 0 0.6 0 0 13.500             $ Cover bottom mount
c
c Spectral shaping
c
20 TRC  9.700 0 0 6.7 0 0 0.715 5.615     $ Zr cone
21 TRC  16.400 0 0 2.980 0 0 5.605 7.795   $ W-1 cone
22 TRC  19.40 0 0 0.200 0 0 7.835 7.940   $ Al spacer
23 RCC  19.60 0 0 0.980 0 0 3.810         $ Al-6061 cylinder inner
24 RCC  19.60 0 0 0.980 0 0 6.340         $ Al-6061 cylinder outer
25 RCC  19.60 0 0 0.980 0 0 6.350         $ W-2 cylinder inner
26 TRC  19.60 0 0 0.980 0 0 7.952 8.655   $ W-2 cone outer
27 RCC  19.60 0 0 0.930 0 0 3.6           $ Al-6061 inner
28 RCC  19.60 0 0 0.930 0 0 3.8           $ Al-6061 outer
29 TRC  20.58 0 0 0.200 0 0 8.660 8.734   $ Al spacer
30 RCC  20.58 0 0 0.200 0 0 3.810         $ Al spacer
31 RCC  20.58 0 0 0.200 0 0 3.800         $ Al spacer
32 TRC  20.78 0 0 2.310 0 0 8.805 10.418  $ W-3
33 RCC  20.78 0 0 2.310 0 0 3.859         $ W-3 inner
34 RCC  20.78 0 0 2.260 0 0 3.775         $ W-3 plug
35 TRC  23.09 0 0 1.180 0 0 10.49 11.278  $ C
36 RCC  23.09 0 0 1.180 0 0 3.859         $ C inner
37 RCC  23.09 0 0 1.180 0 0 3.800         $ C plug
38 TRC  24.27 0 0 3.270 0 0 11.35 13.735  $ Delrin
39 RCC  24.27 0 0 3.270 0 0 3.835         $ Delrin inner
40 RCC  24.27 0 0 3.270 0 0 3.800         $ Delrin plug
41 RCC  27.54 0 0 0.476 0 0 13.50         $ Viton filler
c
c Drawer
60 RPP  19.65 20.53 -2.7 2.7 0 11.5     $ Outside drawer RPP
61 RCC  19.65 0 0 0.880 0 0 2.7          $ Drawer foils RCC
62 RPP  18.59 21.59 -3.75 3.75 7.8 12    $ Drawer handle mount
63 RPP  19.79 20.39 -2.1 2.1 12 15       $ Drawer handle outer
64 RPP  19.79 20.39 -1.5 1.5 12 14.4     $ Drawer handle inner
65 RPP  19.8 20.38 -2.55 2.55 0 11.35    $ Inner drawer area
66 RCC  19.8 0 0 0.58 0 0 2.55           $ Foil region
67 RPP  19.65 20.53 -2.9 2.9 0 11.5      $ Outside drawer RPP
68 RPP  19.8 20.35 -2.5 2.5 1.3 11.3     $ W insert
69 RPP  19.8 20.38 -2.55 -1.47 4.37 5.45 $ Screw hole 1
70 RPP  19.8 20.38 1.47 2.55 4.37 5.45      $ Screw hole 2
```

```
c
c TLDs
80 RPP 20.05 20.139 1.005 1.325 -0.16 0.16    $ TLD-100 #1
81 RPP 20.05 20.139 -0.16 0.16 1.005 1.325    $ TLD-100 #2
82 RPP 20.05 20.139 -1.325 -1.005 -0.16 0.16  $ TLD-100 #3
83 RPP 20.05 20.139 -0.16 0.16 -1.325 -1.005  $ TLD-100 #4
84 2 RPP 20.05 20.139 1.005 1.325 -0.16 0.16  $ TLD-400 #1
85 3 RPP 20.05 20.139 1.005 1.325 -0.16 0.16  $ TLD-400 #2
86 4 RPP 20.05 20.139 1.005 1.325 -0.16 0.16  $ TLD-400 #3
87 5 RPP 20.05 20.139 1.005 1.325 -0.16 0.16  $ TLD-400 #4
c
810 RPP 20.05 20.15 1.0 1.33 -0.165 0.165    $ TLD-100 #1 space
811 RPP 20.05 20.15 -0.165 0.165 1.0 1.33    $ TLD-100 #2 space
812 RPP 20.05 20.15 -1.33 -1.0 -0.165 0.165  $ TLD-100 #3 space
813 RPP 20.05 20.15 -0.165 0.165 -1.33 -1.0  $ TLD-100 #4 space
814 2 RPP 20.05 20.15 1.0 1.33 -0.165 0.165  $ TLD-400 #1 space
815 3 RPP 20.05 20.15 1.0 1.33 -0.165 0.165  $ TLD-400 #2 space
816 4 RPP 20.05 20.15 1.0 1.33 -0.165 0.165  $ TLD-400 #3 space
817 5 RPP 20.05 20.15 1.0 1.33 -0.165 0.165  $ TLD-400 #4 space
c
c Foils
500 RCC  19.800 0 0 0.350 0 0 2.5        $ Al spacer
501 RCC  20.150 0 0 0.005 0 0 2.5        $ Au-1
502 RCC  20.155 0 0 0.023 0 0 2.5        $ Ni
503 RCC  20.178 0 0 0.027 0 0 2.5        $ In
504 RCC  20.205 0 0 0.073 0 0 2.5        $ Al
505 RCC  20.278 0 0 0.025 0 0 2.5        $ Ti
506 RCC  20.303 0 0 0.012 0 0 2.5        $ W
507 RCC  20.315 0 0 0.027 0 0 2.5        $ Zr
508 RCC  20.342 0 0 0.009 0 0 2.5        $ Mg
509 RCC  20.351 0 0 0.005 0 0 2.5        $ Au-2
c
c ATHENA TARPOS and Airbox
250 RPP 31.132 86.6 -7.15 7.15 -7.16 7.15
251 RPP 31.132 86.6 -4.61 4.61 -4.61 4.61
252 RCC 87.6 0 0 183 0 0 15.9
253 RCC 87.6 0 0 183 0 0 13.3
254 RCC 86.6 0 0 1 0 0 16.7
255 RCC 270.6 0 0 270.4 0 0 17
256 RCC 270.6 0 0 270.4 0 0 14.46
257 PY 0
c
c DIM 90-124 ENP
200 6 RCC 346.6 0 0 108.4 0 0 20
201 6 RCC 346.6 0 0 108.4 0 0 19
202 6 TRC 60 0 0 286.6 0 0 16.7 20
203 6 TRC 60 0 0 286.6 0 0 15.7 19
204 6 RCC 58 0 0 2 0 0 16.7
205 6 RPP 1 27 -3.2 3.2 -14.15 14.15
206 6 RPP 1.5 26 -2.7 2.7 -13.65 13.65
207 6 TRC 1.5 0 0 18.5 0 0 13.65 5
208 SPH -0.8 0 -0.8 5
210 6 RPP 27 45 -6 6 -12.7 12.7
211 6 RPP 27 43 -5 5 -11 11
```

```
212 6 RPP 45 58 -6 6 -6 6
213 6 RPP 45 58 -5 5 -5 5
c
c DIM 90-239 TARPOS
220 7 RCC 346.6 0 0 108.4 0 0 17
221 7 RCC 346.6 0 0 108.4 0 0 14.46
222 7 TRC 130 0 0 216 0 0 16.7 20
223 7 TRC 130 0 0 216 0 0 15.7 19
224 7 TRC 30 0 0 100 0 0 4 16.7
225 7 TRC 30 0 0 100 0 0 3 15.7
226 7 RCC 29 0 0 1 0 0 4
227 7 RCC 16 0 0 13 0 0 1.5
228 7 TRC 1.5 0 0 14.5 0 0 0.1 1
c
c Universe (Used if we get full model of NIF)
156  1 RPP  0 22.133 -16.709 16.709 -16.709 16.709
9961 1 PX  -0.001
9962 1 PX   22.134
9963 1 PY  -16.71
9964 1 PY  16.71
9965 1 PZ  -16.71
9966 1 PZ  16.71

c ******************************************************************************
c  Data Cards
c ******************************************************************************
c  Physics
MODE n p e
NPS 1e6
fcl:n 0 35r 1 8r 0 24r
print -85 -86 -128 -130 -140 -161 -162
rand gen=2 stride= 1111152917
phys:n 100 0 0 J J J 0 -1 J J J 0 0
phys:p 100 0 0 0 0 J 0
phys:e 100 0 0 0 0 1 1 1 1 0 0 J J 0.917 1.0e-3
c Rotation for Athena
*tr1  9 0 0
*tr2  0 0 0  0 90 90  90 45 -45  90 135 45   $ rotate 45 about x
*tr3  0 0 0  0 90 90  90 135 45  90 225 135  $ rotate 135 about x
*tr4  0 0 0  0 90 90  90 225 135 90 315 225  $ rotate 225 about x
*tr5  0 0 0  0 90 90  90 315 225 90 45  315  $ rotate 315 about x
*tr6  0 0 0  136 90 226 90 0 90 46 90 136    $ ENP
*tr7  0 0 0 -109 90 -19 90 0 90 -199 90 -109 $ TARPOS
c
c ******************************************************************************
c  Materials
c ******************************************************************************
c Zr shaping
m3
     40090 -5.1450e-01
     40091 -1.1220e-01
     40092 -1.7150e-01
     40094 -1.7380e-01
     40096 -2.8000e-02
```

```
C W shaping
m4
     74182 -2.6500e-01
     74183 -1.4310e-01
     74184 -3.0640e-01
     74186 -2.8430e-01
C Al shaping
m6
     13027 -1
C Carbon shaping
m7
     6012 -9.8930e-01
     6013 -1.0700e-02
C Air/Vacuum
m8
     7014 -9.9610e-01
     7015 -3.8982e-03
C Delrin
m9
     1001 0.4999
     1002 0.0001
     6012 0.24725
     6013 0.00275
     8016 0.2494
     8017 0.0001
     8018 0.0005
C Viton
m10
     1001 -0.009417
     6012 -0.277469
     6013 -0.003086
     9019 -0.710028
c
c Activation Foils
c
C Au
m11
     79197 -1
C Ni
m12
     28058 -6.8077e-01
     28060 -2.6223e-01
     28061 -1.1399e-02
     28062 -3.6346e-02
     28064 -9.2550e-03
C In
m13
     49113 -4.2900e-02
     49115 -9.5710e-01
C Al
m14
     13027 -1
C Ti
m15
```

```
     22046 0.0825
     22047 0.0744
     22048 0.7372
     22049 0.0541
     22050 0.0518
C W
m16
     74182 -2.6500e-01
     74183 -1.4310e-01
     74184 -3.0640e-01
     74186 -2.8430e-01
C Zr
m17
     40090 -5.1450e-01
     40091 -1.1220e-01
     40092 -1.7150e-01
     40094 -1.7380e-01
     40096 -2.8000e-02
C Mg
m18
     12024  0.79
     12025  0.10
     12026  0.11
c
c CaF2:Mn
m20
     9019  6.380E-01
     20040  3.092E-01
     20042  2.064E-03
     20043  4.307E-04
     20044  6.654E-03
     20046  1.276E-05
     20048  5.965E-04
     25055  4.300E-02
C name: 316 SS
c density = 8 g/cc
m21     6012  -8.0000E-04  14028  -9.1874E-03
        14029  -4.8182E-04  14030  -3.3084E-04
        15031  -4.5000E-04  16032  -2.8415E-04
        16033  -2.3136E-06  16034   -1.3506E-05
        16036  -3.3651E-08  24050  -7.1035E-03
        24052  -1.4229E-01  24053  -1.6443E-02
        24054  -4.1619E-03  25055  -2.0000E-02
        26054  -3.6923E-02  26056  -6.0051E-01
        26057  -1.4124E-02  26058  -1.8981E-03
        28058  -8.0641E-02  28060  -3.2127E-02
        28061  -1.4202E-03  28062  -4.5961E-03
        28064  -1.2155E-03  42092  -3.5540E-03
        42094  -2.2635E-03  42095  -3.9371E-03
        42096  -4.1685E-03  42097  -2.4115E-03
        42098  -6.1561E-03  42100  -2.5071E-03
c
c name: 304 SS
c Density 8.0 g/cc
```

```
m22   6012 -0.0004   14028 -0.00461 14029 -0.00024
      14030 -0.00016
      15031 -0.00023 16032 -0.00014 16033 -1.1E-6
      16034 -6.4E-6 16036 -1.5E-8
      24050 -0.00826 24052 -0.1592 24053 -0.01805
      24054 -0.00449 25055 -0.01
      26054 -0.04105 26056 -0.64384
      26057 -0.01488 26058 -0.00196  28058 -0.06297
      28060 -0.02426 28061 -0.00105  28062 -0.00336
      28064 -0.0086
c
c c name: 17-4PH SS
c Density   7.75 g/cc
c not in PNNL lib
c from https://core.ac.uk/download/pdf/188225908.pdf
m23   26054 -0.0409  26056 -0.64142
      26057 -0.01482 26058 -0.00196  24050 -0.0076
      24052 -0.14663 24053 -0.01663  24054 -0.00414
      28058 -0.03404 28060 -0.01311 28061 -0.00057
      28062 -0.00182 28064 -0.00046 29000 -0.05
      14028 -0.00922  14029 -0.00047  14030 -0.00031
      25055 -0.01
      41093 -0.00225 73181 -0.00225
      6012  -0.0007  15031 -0.0004
      16032 -0.000028 16033 -2.3E-7
      16034 -1.3E-6 16036 -3E-8
c Materials for TARPOS and ENP on 90-124
c
c 409 SS rho=7.8 g/cm3
m27  6012  -7.8085e-02  6013  -9.1516e-04   14028 -9.0305e-01
     14029 -4.7515e-02  14030 -3.2438e-02   15031 -4.4000e-02
     16032 -4.1675e-02  16033 -3.3933e-04   16034 -1.9810e-03
     16036 -4.9355e-06  22046 -5.8371e-02   22047 -5.3785e-02
     22048 -5.4424e-01  22049 -4.0772e-02   22050 -3.9834e-02
     24050 -4.6453e-01  24052 -9.3157e-00   24053 -1.0767e-00
     24054 -2.7306e-01  25055 -9.8300e-01   26054 -4.8552e-00
     26056 -7.9035e+1   26057 -1.8579
     26058 -2.5159e-01
c NIF chamber
c
c    As-Built Al-5083 for Chamber
m101 6012  -4.9172E-04  7014  -1.8992E-05
     7015  -6.9765E-08  8016  -4.4624E-04
     12024 -3.4682E-02  12025  -4.5740E-03
     12026 -5.2248E-03  13027 -9.4652E-01
     14028 -9.2970E-04  14029 -4.7075E-05
     14030 -3.1249E-05  22046 -8.2624E-06
     22047 -7.5395E-06  22048 -7.6221E-05
     22049 -5.6804E-06  22050 -5.5771E-06
     23050 -8.4754E-08
     23051 -4.3092E-05  24050 -2.6669E-05
     24052 -5.1429E-04  24053 -5.8310E-05
     24054 -1.4516E-05  25055 -2.9764E-03
     26054 -1.0778E-04  26056 -1.6905E-03
```

```
      26057 -3.9060E-05  26058 -5.1589E-06
      28058 -1.7841E-04  28060 -6.8207E-05
      28061 -2.9530E-06  28062 -9.3817E-06
      28064 -2.6933E-04  29063 -3.3476E-04
      29065 -1.4921E-04  30066 -1.5664E-04
      30064 -5.6017E-04  30067 -2.3167E-05
      30068 -1.0738E-04  30070 -3.6547E-06
      31069 -5.7142E-05  31070 -3.8939E-05
      40090 -9.6392E-06  40091 -2.1255E-06
      40090 -3.2846E-06  40090 -3.4011E-06
      40090 -5.5961E-07
c
c     As-Built Gunite with 1 vol% A-615 steel rebar
m102 1001  -2.5091E-04  1002  -3.7642E-08
      3006  -1.0994E-06  3007  -1.3521E-05
      5010  -2.8718E-04  5011  -1.1559E-03
      6012  -4.2352E-05  7014  -1.1578E-05
      7015  -4.2532E-08  8016  -5.5987E-01
      9019  -2.7112E-05  11023 -5.6754E-03
      12024 -6.3061E-03  12025 -8.3165E-04
      12026 -9.4999E-04  13027 -4.3344E-02
      14028 -2.0919E-01  14029 -1.0592E-02
      14030 -7.0313E-03  15031 -3.8947E-04
      16032 -1.0850E-03  16033 -8.8341E-06
      16034 -5.1572E-05  16036 -1.2849E-07
      19039 -2.7490E-03  19040 -3.5373E-07
      19041 -2.0856E-04
      20040 -1.0239E-01  20041 -7.1747E-04
      20042 -1.5324E-04  20043 -2.4221E-03
      20046 -4.8580E-06  20048 -2.3699E-04
      22046 -1.2950E-04
      22047 -1.1817E-04  22048 -1.1946E-03
      22049 -8.9029E-05  22050 -8.7410E-05
      23050 -1.3618E-07  23051 -6.9239E-05
      24050 -1.9066E-05
      24052 -3.6767E-04  24053 -4.1686E-05
      24054 -1.0378E-05  25055 -3.0447E-04
      26054 -2.3809E-03  26056 -3.7342E-02
      26057 -8.6282E-04  26058 -1.1396E-04
      27059 -1.6865E-05  28058 -9.1495E-05
      28060 -3.4979E-05  28061 -1.5144E-06
      28062 -4.8113E-06  28064 -1.2196E-06
      29063 -7.1485E-05  29065 -3.1862E-05
      30064 -7.2433E-06  30066 -4.2126E-06
      30067 -6.2305E-07  30068 -2.8878E-06
      30070 -9.8289E-08  40090 -1.3828E-05
      40091 -3.0492E-06  40092 -4.7121E-06
      40094 -4.8792E-06  40096 -8.0282E-07
      42092 -9.8903E-06  42094 -6.1648E-06
      42095 -1.0610E-05  42096 -1.1117E-05
      42097 -6.3647E-06  42098 -1.6082E-05
      42100 -6.4180E-06  56138 -2.3182E-04
      74182 -9.6064E-06  74183 -5.2160E-06
      74184 -1.1214E-05  74186 -1.0447E-05
```

```
c
c    I-Beam and Flashing (SS-409 & Al-6061 mix)
m108 6012 -3.1819E-04   12024 -5.3005E-03
     12025 -6.9903E-04  12026 -7.9850E-04
     13027 -5.4786E-01  14028 -3.8774E-02
     14029 -1.9633E-03  14030 -1.3032E-03
     15031 -1.7898E-04  16032 -1.1301E-04
     16033 -9.2019E-07  16034 -5.3720E-06
     16036 -1.3384E-08
     22046 -3.1410E-04  22047 -2.8397E-04
     22048 -2.8262E-03  22049 -2.0814E-04
     22050 -2.0041E-04  24050 -2.0423E-03
     24052 -3.9368E-02  24053 -4.3967E-03
     24054 -1.1083E-03  25055 -4.8272E-03
     26054 -1.9960E-02  26056 -3.1328E-01
     26057 -7.2434E-03  26058 -9.5614E-04
     28058 -1.3523E-03  28060 -5.1707E-04
     28061 -2.2671E-05  28062 -7.2190E-05
     28064 -1.8495E-05  29063 -1.5674E-03
     29065 -6.9861E-04  30064 -6.8097E-04
     30066 -3.9603E-04  30067 -5.8575E-05
     30068 -2.7149E-04  30070 -9.2404E-06
c
c    Al-6061 for FW and Port Covers-den 0.28178
m126 12024 -9.3565E-03  12025 -1.2340E-03
     12026 -1.4095E-03  13027 -9.6710E-01
     14028 -3.6892E-03  14029 -1.8680E-04
     14030 -1.2400E-04  22046 -1.2000E-04
     22047 -1.0950E-04  22048 -1.1070E-03
     22049 -8.2500E-05  22050 -8.1000E-05
     24050 -1.7380E-05  24052 -3.3516E-04
     24053 -3.8000E-05  24054 -9.4600E-06
     25055 -1.5000E-03  26054 -4.0950E-04
     26056 -6.4225E-03  26057 -1.4840E-04
     26058 -1.9600E-05  29063 -2.7668E-03
     29065 -1.2332E-03  30064 -1.2020E-03
     30066 -6.9907E-04  30067 -1.0339E-04
     30068 -4.7922E-04  30070 -1.6311E-05
c
c    Pure SS-409 for FW-0.17826 g/cc
m131 6012  -0.0008   14028 -0.09223
     14029 -0.00467  14030 -0.0031
     15031 -0.00045  16032 -2.8415E-04
     16033 -2.3136E-06  16034 -1.3506E-05
     16036 -3.3651E-08
     22046 -6.188e-4 22047 -5.58e-4
     22048 -5.529e-3 22049 -4.058e-4
     22050 -3.885e-4 24050 -5.11e-3
     24052 -0.0985   24053 -0.011
     24054 -2.773e-3 25055 -0.01
     26054 -0.0496   26056 -0.7785
     26057 -0.018    26058 -2.376e-3
     28058 -0.0034   28060 -0.0013
     28061 -5.7e-5
```

```
     28062 -1.815e-4 28064 -4.65e-5
c
c    Al-6061 for FW and Port Covers-density 0.072047
m136 12024 -9.3565E-03  12025 -1.2340E-03
     12026 -1.4095E-03  13027 -9.6710E-01
     14028 -3.6892E-03  14029 -1.8680E-04
     14030 -1.2400E-04  22046 -1.2000E-04
     22047 -1.0950E-04  22048 -1.1070E-03
     22049 -8.2500E-05  22050 -8.1000E-05
     24050 -1.7380E-05  24052 -3.3516E-04
     24053 -3.8000E-05  24054 -9.4600E-06
     25055 -1.5000E-03  26054 -4.0950E-04
     26056 -6.4225E-03  26057 -1.4840E-04
     26058 -1.9600E-05  29063 -2.7668E-03
     29065 -1.2332E-03  30064 -1.2020E-03
     30066 -6.9907E-04  30067 -1.0339E-04
     30068 -4.7922E-04  30070 -1.6311E-05
c
c ******************************************************************************
c  Tallies
c ******************************************************************************
c
c The 129 STAYSL structure is used to bin tallies by energy
c
FC4 Neutron flux in each foil
F4:n 51 52 53 54 55 56 57 58 59
c
FC14 Foil pack neutron flux
F14:n (51 52 53 54 55 56 57 58 59)
T14 -1 0.3 0.4 0.5 0.6 0.7 0.8 0.9 1 2.4
       5.6 13.3 31.6 75 117 421 1E3 1E4 1E5 1E6 1E7 1E8 T
c
c  TLD Dose environment
c
FC194 Neutron Flux in TLDs
F194:n (70 71 72 73 74 75 76 77)
c
FC204 Gamma flux in TLDs
F204:p (70 71 72 73 74 75 76 77)
T204 -1 0.3 0.4 0.5 0.6 0.7 0.8 0.9 1 2.4
       5.6 13.3 31.6 75 117 421 1E3 1E4 1E5 1E6 1E7 1E8 T
c
FC6 TLD-100s Rads
F6:e (70 71 72 73)
FM6 1.6E-8 $ 1.6E-13 (J/MeV)*1000 (g/kg) * 100 Rad/(J/kg)
E6 0.001 0.01 0.1 0.3 0.5 1 3 6 10 T
T6 -1 0.3 0.4 0.5 0.6 0.7 0.8 0.9 1 2.4
       5.6 13.3 31.6 75 117 421 1E3 1E4 1E5 1E6 1E7 1E8 T
FC16 TLD-400s Rads
F16:e (74 75 76 77)
E16 0.001 0.01 0.1 0.3 0.5 1 3 6 10 T
FM16 1.6E-8 $ 1.6E-13 (J/MeV)*1000 (g/kg) * 100 Rad/(J/kg)
T16 -1 0.3 0.4 0.5 0.6 0.7 0.8 0.9 1 2.4
       5.6 13.3 31.6 75 117 421 1E3 1E4 1E5 1E6 1E7 1E8 T
```

```
E0    1.00E-10 1.00E-09 1.00E-08 2.30E-08 5.00E-08 7.60E-08 1.15E-07
      1.70E-07 2.55E-07 3.80E-07 5.50E-07 8.40E-07 1.28E-06 1.90E-06
      2.80E-06 4.25E-06 6.30E-06 9.20E-06 1.35E-05 2.10E-05 3.00E-05
      4.50E-05 6.90E-05 1.00E-04 1.35E-04 1.70E-04 2.20E-04 2.80E-04
      3.60E-04 4.50E-04 5.75E-04 7.60E-04 9.60E-04 1.28E-03 1.60E-03
      2.00E-03 2.70E-03 3.40E-03 4.50E-03 5.50E-03 7.20E-03 9.20E-03
      1.20E-02 1.50E-02 1.90E-02 2.55E-02 3.20E-02 4.00E-02 5.25E-02
      6.60E-02 8.80E-02 1.10E-01 1.35E-01 1.60E-01 1.90E-01 2.20E-01
      2.55E-01 2.90E-01 3.20E-01 3.60E-01 4.00E-01 4.50E-01 5.00E-01
      5.50E-01 6.00E-01 6.60E-01 7.20E-01 7.80E-01 8.40E-01 9.20E-01
      1.00E+00 1.20E+00 1.40E+00 1.60E+00 1.80E+00 2.00E+00 2.30E+00
      2.60E+00 2.90E+00 3.30E+00 3.70E+00 4.10E+00 4.50E+00 5.00E+00
      5.50E+00 6.00E+00 6.70E+00 7.40E+00 8.20E+00 9.00E+00 1.00E+01
      1.10E+01 1.20E+01 1.25E+01 1.26E+01 1.27E+01 1.28E+01 1.29E+01
      1.30E+01 1.31E+01 1.32E+01 1.33E+01 1.34E+01 1.35E+01 1.36E+01
      1.37E+01 1.38E+01 1.39E+01 1.40E+01 1.41E+01 1.42E+01 1.43E+01
      1.44E+01 1.45E+01 1.46E+01 1.47E+01 1.48E+01 1.49E+01 1.50E+01
      1.51E+01 1.52E+01 1.53E+01 1.54E+01 1.55E+01 1.56E+01 1.57E+01
      1.58E+01 1.59E+01 1.60E+01 1.65E+01
c ***************************************************************************
c  Source
c ***************************************************************************
SDEF PAR=n ERG=d2 POS=0.0 0.0 0.0 VEC=0 0 1
#   SI2           SP2      $ Source Spectrum at 8.8 keV
     12 0
     13.293734   0.002595846
     13.300679   0.003143204
     13.307623   0.002889355
     13.314679   0.002759715
     13.321623   0.002483202
     13.32868    0.003331836
     13.335624   0.003136216
     13.342681   0.003876888
     13.349737   0.004195655
     13.356681   0.005649322
     13.363737   0.005300441
     13.370794   0.006930848
     13.37785    0.007653055
     13.384906   0.00851353
     13.391963   0.009769057
     13.399019   0.010848302
     13.406075   0.012312101
     13.413131   0.013816193
     13.420188   0.016330301
     13.427244   0.017058896
     13.434413   0.020332808
     13.441469   0.021960488
     13.448525   0.024317447
     13.455693   0.02767652
     13.462749   0.030190186
     13.469918   0.033245179
     13.476974   0.037478468
     13.484143   0.040225076
     13.491199   0.045002486
```

```
13.498367   0.048312375
13.505536   0.053851827
13.512704   0.057794339
13.519872   0.062981459
13.52704    0.068019167
13.534096   0.072999321
13.541265   0.079126902
13.548433   0.084435887
13.555602   0.090912806
13.562882   0.09726935
13.57005    0.103931106
13.577219   0.111946124
13.584499   0.118574191
13.591667   0.126535885
13.598836   0.135553155
13.606116   0.144238874
13.613284   0.153834737
13.620564   0.163638024
13.627733   0.174292174
13.635013   0.1849865
13.642294   0.196753888
13.649574   0.208705504
13.656742   0.220375206
13.664022   0.234296088
13.671302   0.246205409
13.678583   0.260060475
13.685863   0.273628735
13.693143   0.286661812
13.700424   0.301668064
13.707704   0.315797348
13.715097   0.3309202
13.722377   0.345761666
13.729657   0.361859544
13.73705    0.375991736
13.74433    0.39370984
13.75161    0.408915836
13.759002   0.426673092
13.766395   0.444122663
13.773676   0.461266708
13.781067   0.479402036
13.788459   0.497768413
13.795852   0.516483686
13.803133   0.535692132
13.810525   0.553330984
13.817917   0.574804199
13.825309   0.591414318
13.832702   0.612693771
13.840094   0.629757256
13.847599   0.647931278
13.854991   0.667136746
13.862383   0.686153621
13.869887   0.702200377
13.87728    0.718374858
13.884672   0.736399535
```

```
13.892176   0.751940461
13.899569   0.769925528
13.907073   0.783763805
13.914577   0.801664257
13.92197    0.814040877
13.929474   0.831758654
13.936978   0.846252302
13.944482   0.861173281
13.951875   0.876988988
13.95938    0.891525385
13.966883   0.905805581
13.974388   0.918552129
13.982005   0.932538345
13.989508   0.942551909
13.997013   0.956277605
14.004517   0.96244804
14.012022   0.973337133
14.019638   0.978880392
14.027142   0.985519206
14.034759   0.98989348
14.042263   0.992173132
14.04988    0.996759419
14.057496   0.997497018
14.065  1
14.072616   0.996662734
14.080232   0.996470346
14.087849   0.993580199
14.095465   0.990116876
14.103081   0.986994992
14.110698   0.980789396
14.118314   0.97693289
14.12593    0.969654208
14.133547   0.963141516
14.141163   0.955640158
14.148892   0.94741036
14.156508   0.938571636
14.164237   0.930606511
14.171853   0.919773513
14.179469   0.90987253
14.187197   0.898443951
14.194926   0.887038367
14.202542   0.873846335
14.210271   0.860616688
14.217999   0.846330475
14.225727   0.831016542
14.233455   0.81601533
14.241184   0.799979335
14.248912   0.783495796
14.25664    0.767566069
14.264369   0.75204166
14.272097   0.735017162
14.279826   0.717840638
14.287666   0.701943946
14.295395   0.684070446
```

```
14.303122   0.666239467
14.310963   0.647928236
14.318803   0.629289106
14.326531   0.610350437
14.334372   0.591796708
14.3421 0.572979287
14.349941   0.554141195
14.357781   0.535963543
14.365621   0.517752954
14.373461   0.4997812
14.381302   0.48231606
14.389143   0.465155529
14.396983   0.447876531
14.404823   0.431848287
14.412663   0.415109298
14.420503   0.399173684
14.428456   0.383147141
14.436296   0.367503511
14.444249   0.351596026
14.452089   0.336258053
14.459929   0.320678066
14.467882   0.30564627
14.475834   0.290574556
14.483786   0.276366443
14.491626   0.262220589
14.499579   0.249067777
14.507532   0.235978288
14.515483   0.223374951
14.523436   0.211437616
14.531389   0.199795447
14.539341   0.188815822
14.547293   0.178120231
14.555358   0.167967573
14.56331    0.158189867
14.571262   0.148721641
14.579326   0.139713503
14.587279   0.131114934
14.595343   0.122845385
14.603296   0.115100811
14.61136    0.107690306
14.619424   0.100738963
14.627377   0.094133932
14.635441   0.087902156
14.643506   0.081992162
14.65157    0.076393198
14.659634   0.071127009
14.667699   0.066164418
14.675763   0.06145838
14.683827   0.057066199
14.692004   0.052886633
14.700068   0.048967563
14.708132   0.045290071
14.716308   0.041805197
14.724373   0.038540419
```

```
      14.732549   0.035480531
      14.740614   0.032626086
      14.74879    0.029955985
      14.756966   0.027492629
      14.765031   0.0251978
      14.773207   0.023092789
      14.781383   0.021151086
      14.78956    0.019392379
      14.797736   0.017770848
      14.805913   0.016316756
      14.814089   0.014966334
      14.822378   0.013754329
      14.830554   0.012646631
      14.83873    0.011642544
      14.846906   0.010734519
      14.855195   0.009914765
      14.863483   0.009159488
      14.87166    0.008461644
      14.879836   0.007811633
      14.888124   0.007239409
c ADVANTG
sb2    0.00000e+00 2.78870e-05 3.54303e-05 3.25689e-05 3.11076e-05 2.79907e-05
       3.75566e-05 3.53515e-05 4.37004e-05 4.72936e-05 6.36794e-05 5.97468e-05
       7.81248e-05 8.62655e-05 9.59648e-05 1.10117e-04 1.22282e-04 1.38782e-04
       1.55737e-04 1.84076e-04 1.92288e-04 2.29192e-04 2.47539e-04 2.74107e-04
       3.11971e-04 3.40305e-04 3.74741e-04 4.22459e-04 4.53418e-04 5.07270e-04
       5.44579e-04 6.07020e-04 6.51460e-04 7.09929e-04 7.66714e-04 8.22851e-04
       8.91921e-04 9.51764e-04 1.02477e-03 1.09642e-03 1.17152e-03 1.26186e-03
       1.33657e-03 1.42632e-03 1.52796e-03 1.62587e-03 1.73403e-03 1.84453e-03
       1.96463e-03 2.08517e-03 2.21782e-03 2.35254e-03 2.48408e-03 2.64099e-03
       2.77524e-03 2.93141e-03 3.08435e-03 3.23126e-03 3.40041e-03 3.55968e-03
       3.73014e-03 3.89744e-03 4.07889e-03 4.23819e-03 4.43791e-03 4.60931e-03
       4.80947e-03 5.00617e-03 5.19941e-03 5.40384e-03 5.61086e-03 5.82182e-03
       6.03834e-03 6.23717e-03 6.47921e-03 6.66644e-03 6.90631e-03 7.10677e-03
       7.95845e-03 8.19435e-03 8.42793e-03 8.62503e-03 8.82370e-03 9.04510e-03
       9.23598e-03 9.45689e-03 9.62686e-03 9.84673e-03 9.99875e-03 1.02164e-02
       1.03944e-02 1.05777e-02 1.07719e-02 1.09505e-02 1.11259e-02 1.12825e-02
       1.14542e-02 1.15772e-02 1.17458e-02 1.18216e-02 1.19554e-02 1.20235e-02
       1.21050e-02 1.21587e-02 1.21867e-02 1.22431e-02 1.22521e-02 1.22829e-02
       1.22419e-02 1.22395e-02 1.22040e-02 1.21615e-02 1.21231e-02 1.20469e-02
       1.19995e-02 1.19101e-02 1.18301e-02 1.17380e-02 1.16369e-02 1.15283e-02
       1.14305e-02 1.12975e-02 1.11758e-02 1.10355e-02 1.11788e-02 1.12924e-02
       1.11214e-02 1.09368e-02 1.07389e-02 1.05451e-02 1.03378e-02 1.01248e-02
       9.91897e-03 9.71835e-03 9.49835e-03 9.27638e-03 9.07096e-03 8.83998e-03
       8.60956e-03 8.37293e-03 8.13207e-03 7.88733e-03 7.64757e-03 7.40439e-03
       7.16096e-03 6.92605e-03 6.69073e-03 6.45848e-03 6.23279e-03 6.01103e-03
       5.78774e-03 5.58061e-03 5.36430e-03 5.15837e-03 4.95127e-03 4.74911e-03
       4.54354e-03 4.34534e-03 4.14400e-03 3.94975e-03 3.75499e-03 3.57138e-03
       3.38858e-03 3.21861e-03 3.04946e-03 2.88659e-03 2.73233e-03 2.58188e-03
       2.44000e-03 2.30178e-03 2.17058e-03 2.04423e-03 1.92187e-03 1.80546e-03
       1.69435e-03 1.58748e-03 1.48740e-03 1.39164e-03 1.30181e-03 1.21646e-03
       1.13593e-03 1.05955e-03 9.87200e-04 9.19147e-04 8.55018e-04 7.94203e-04
       7.37445e-04 6.83434e-04 6.32789e-04 5.85266e-04 5.40233e-04 4.98043e-04
       4.58501e-04 4.21615e-04 3.87110e-04 3.55277e-04 3.25622e-04 2.98419e-04
```

```
       2.73327e-04 2.50600e-04 2.29646e-04 2.10855e-04 1.93404e-04 1.77742e-04
       1.63428e-04 1.50452e-04 1.38718e-04 1.28125e-04 1.18365e-04 1.09347e-04
       1.00947e-04 9.35521e-05
wwp:n 5.0 j 100 j -1 0 2.741987751e-06
```

# Appendix D. ATHENA-I Hybrid Model MCNP Input Deck

```
Athena experiment
c ****************************************************************************
c  Cell Cards
c ****************************************************************************
c NIF Chamber
2   131  -0.17826   1 -2              imp:n,p=1 imp:e=0 $ 409 SS Wall
3   126  -0.28178   2 -3              imp:n,p=1 imp:e=0 $ Al Wall and Port Covers
4   136  -0.072047  3 -4              imp:n,p=1 imp:e=0 $ Al FW Wall
5   108  -0.048682  4 -5              imp:n,p=1 imp:e=0 $ I beam and flashing
6   101  -2.7       5 -7              imp:n,p=1 imp:e=0 $ Al Wall
7   102  -2.4249    7 -8              imp:n,p=1 imp:e=0 $ Gunite
8   0               8                 imp:n,p,e=0       $ Kill radius
c
c ############################################################################
c                               PSEUDO CELLS
c ############################################################################
c
c FCL = 0
c
10   3  -6.490  0  u=9    imp:n,p=1 imp:e=0 $ Zr shaping
11   4  -18.70  0  u=9    imp:n,p=1 imp:e=0 $ W shaping
12   6  -2.700  0  u=9    imp:n,p=1 imp:e=0 $ Al shaping
13   7  -2.260  0  u=9    imp:n,p=1 imp:e=0 $ C shaping
14   9  -1.400  0  u=9    imp:n,p=1 imp:e=0 $ Delrin shaping
15  10  -1.800  0  u=9    imp:n,p=1 imp:e=0 $ Viton seal
c
c FCL = 1
c
16  12  -9.019  0  u=9    fcl:n=1 imp:n,p=1 imp:e=0 $ Ni foil
17  14  -2.646  0  u=9    fcl:n=1 imp:n,p=1 imp:e=0 $ Al foil
18  15  -4.303  0  u=9    fcl:n=1 imp:n,p=1 imp:e=0 $ Ti foil
19  16  -18.27  0  u=9    fcl:n=1 imp:n,p=1 imp:e=0 $ W foil
20  17  -5.815  0  u=9    fcl:n=1 imp:n,p=1 imp:e=0 $ Zr foil
21  18  -1.800  0  u=9    fcl:n=1 imp:n,p=1 imp:e=0 $ Mg foil
22  13  -6.913  0  u=9    fcl:n=1 imp:n,p=1 imp:e=0 $ In foil
c
c FCL = 0
c
23  21  -7.800  0  u=9    imp:n,p=1 imp:e=0 $ Drawer material
24  22  -7.870  0  u=9    imp:n,p=1 imp:e=0 $ Outer shell
25  23  -7.870  0  u=9    imp:n,p=1 imp:e=0 $ Cover and mount
c
c FCL = 1
c
26  11  -19.18  0  u=9    fcl:n=1 imp:n,p=1 imp:e=0 $ First Au foil
27  11  -19.19  0  u=9    fcl:n=1 imp:n,p=1 imp:e=0 $ Second Au foil
c
c FCL = 0
c
28  8 -1.29e-9  0  u=9    imp:n,p,e=1       $ TLD-100 #1
29  8 -1.29e-9  0  u=9    imp:n,p,e=1       $ TLD-100 #2
30  8 -1.29e-9  0  u=9    imp:n,p,e=1       $ TLD-100 #3
```

```
31  8 -1.29e-9  0  u=9    imp:n,p,e=1       $ TLD-100 #4
32  20  -3.180  0  u=9    imp:n,p,e=1       $ TLD-400 #1
33  20  -3.180  0  u=9    imp:n,p,e=1       $ TLD-400 #2
34  20  -3.180  0  u=9    imp:n,p,e=1       $ TLD-400 #3
35  20  -3.180  0  u=9    imp:n,p,e=1       $ TLD-400 #4
36   0          0  u=9    imp:n,p,e=1       $ Inferred Background
c
c ############################################################################
c UM universe fill cell
40   0        -1 -99  fill=9 imp:n,p,e=1
c
c Air outside fill box
41  8    -1.29e-9  -1  99
             #210 #211 #212 #213 #250 #251 #252 #253
                                imp:n,p=1 imp:e=0
c
c ATHENA Airbox and DIM 90-348
c
250 27  -2.7       99 -250 251          imp:n,p=1 imp:e=0  $ Airbox
251 27  -2.7       99 -252 253 257      imp:n,p=1 imp:e=0  $ Airbox Bracket
252 27  -2.7       99 -254              imp:n,p=1 imp:e=0  $ Bracket
253 27  -2.7       99 -1 -255 256       imp:n,p=1 imp:e=0  $ DIM
c
c TARPOS on 90-239
210 27  -2.7       -1 -220 221       imp:n,p=1 imp:e=0 $ TARPOS
211 27  -2.7       -222 223          imp:n,p=1 imp:e=0 $ TARPOS
212 27  -2.7       -224 225          imp:n,p=1 imp:e=0 $ TARPOS Snout
213 27  -2.7       -226:-227:-228    imp:n,p=1 imp:e=0 $ TARPOS Snout

c ****************************************************************************
c  Surface Cards
c ****************************************************************************
c NIF surfaces
1  SO    463.316
2  SO    478.416
3  SO    479.616
4  SO    489.84
5  SO    500
7  SO    510
8  SO    550
c
c UM fill cell (Universe 9)
99 RCC 8.998 0 0  22.135 0 0  16.708
c
c ATHENA TARPOS and Airbox
250 RPP 31.134 86.6 -7.15 7.15 -7.16 7.15
251 RPP 31.134 86.6 -4.61 4.61 -4.61 4.61
252 RCC 87.6 0 0 183 0 0 15.9
253 RCC 87.6 0 0 183 0 0 13.3
254 RCC 86.6 0 0 1 0 0 16.7
255 RCC 270.6 0 0 270.4 0 0 17
256 RCC 270.6 0 0 270.4 0 0 14.46
257 PY 0
c DIM 90-124 ENP
```

```
200 6 RCC 346.6 0 0 108.4 0 0 20
201 6 RCC 346.6 0 0 108.4 0 0 19
202 6 TRC 60 0 0 286.6 0 0 16.7 20
203 6 TRC 60 0 0 286.6 0 0 15.7 19
204 6 RCC 58 0 0 2 0 0 16.7
205 6 RPP 1 27 -3.2 3.2 -14.15 14.15
206 6 RPP 1.5 26 -2.7 2.7 -13.65 13.65
207 6 TRC 1.5 0 0 18.5 0 0 13.65 5
208 SPH -0.8 0 -0.8 5
210 6 RPP 27 45 -6 6 -12.7 12.7
211 6 RPP 27 43 -5 5 -11 11
212 6 RPP 45 58 -6 6 -6 6
213 6 RPP 45 58 -5 5 -5 5
c DIM 90-239 TARPOS
220 7 RCC 346.6 0 0 108.4 0 0 17
221 7 RCC 346.6 0 0 108.4 0 0 14.46
222 7 TRC 130 0 0 216 0 0 16.7 20
223 7 TRC 130 0 0 216 0 0 15.7 19
224 7 TRC 30 0 0 100 0 0 4 16.7
225 7 TRC 30 0 0 100 0 0 3 15.7
226 7 RCC 29 0 0 1 0 0 4
227 7 RCC 16 0 0 13 0 0 1.5
228 7 TRC 1.5 0 0 14.5 0 0 0.1 1
c
c Universe (Used if we get full model of NIF)
156  1 RPP  0 22.133 -16.709 16.709 -16.709 16.709
9961 1 PX  -0.001
9962 1 PX   22.134
9963 1 PY  -16.71
9964 1 PY  16.71
9965 1 PZ  -16.71
9966 1 PZ  16.71

c ****************************************************************************
c  Data Cards
c ****************************************************************************
c Embedding the Abaqus input deck
embed9 meshgeo=abaqus
       mgeoin=athena_abaqus.inp
       length= 1.00000E+00          $ scale units to cm
       background= 36
       matcell= 1 10   2 11   3 12   4 13   5 14   6 15   7 16
                8 17   9 18  10 19  11 20  12 21  13 22  14 23
               15 24  16 25  17 26  18 27  19 28  20 29  21 30
               22 31  23 32  24 33  25 34  26 35
c  Physics
MODE n p e
NPS 1e7
c
print -85 -86 -128 -130 -140 -161 -162
rand gen=2 stride= 1111152917
phys:n 100 0 0 J J J 0 -1 J J J 0 0
phys:p 100 0 0 0 0 J 0
phys:e 100 0 0 0 0 1 1 1 1 0 0 J J 0.917 1.0e-3
```

```
c Rotation for Athena
*tr1  9 0 0
*tr2  0 0 0  0 90 90  90 45 -45  90 135 45   $ rotate 45 about x
*tr3  0 0 0  0 90 90  90 135 45  90 225 135  $ rotate 135 about x
*tr4  0 0 0  0 90 90  90 225 135 90 315 225  $ rotate 225 about x
*tr5  0 0 0  0 90 90  90 315 225 90 45  315  $ rotate 315 about x
*tr6  0 0 0  136 90 226 90 0 90 46 90 136    $ ENP
*tr7  0 0 0 -109 90 -19 90 0 90 -199 90 -109 $ TARPOS
c
c ****************************************************************************
c  Materials
c ****************************************************************************
C Zr shaping
m3
     40090 -5.1450e-01
     40091 -1.1220e-01
     40092 -1.7150e-01
     40094 -1.7380e-01
     40096 -2.8000e-02
C W shaping
m4
     74182 -2.6500e-01
     74183 -1.4310e-01
     74184 -3.0640e-01
     74186 -2.8430e-01
C Al shaping
m6
     13027 -1
C Carbon shaping
m7
     6012 -9.8930e-01
     6013 -1.0700e-02
C Air/Vacuum
m8
     7014 -9.9610e-01
     7015 -3.8982e-03
C Delrin
m9
     1001 0.4999
     1002 0.0001
     6012 0.24725
     6013 0.00275
     8016 0.2494
     8017 0.0001
     8018 0.0005
C Viton
m10
     1001 -0.009417
     6012 -0.277469
     6013 -0.003086
     9019 -0.710028
c
c Activation Foils
c
```

```
C Au
m11
     79197 -1
C Ni
m12
     28058 -6.8077e-01
     28060 -2.6223e-01
     28061 -1.1399e-02
     28062 -3.6346e-02
     28064 -9.2550e-03
C In
m13
     49113 -4.2900e-02
     49115 -9.5710e-01
C Al
m14
     13027 -1
C Ti
m15
     22046 0.0825
     22047 0.0744
     22048 0.7372
     22049 0.0541
     22050 0.0518
C W
m16
     74182 -2.6500e-01
     74183 -1.4310e-01
     74184 -3.0640e-01
     74186 -2.8430e-01
C Zr
m17
     40090 -5.1450e-01
     40091 -1.1220e-01
     40092 -1.7150e-01
     40094 -1.7380e-01
     40096 -2.8000e-02
C Mg
m18
     12024  0.79
     12025  0.10
     12026  0.11
c CaF2:Mn
m20
     9019  6.380E-01
     20040  3.092E-01
     20042  2.064E-03
     20043  4.307E-04
     20044  6.654E-03
     20046  1.276E-05
     20048  5.965E-04
     25055  4.300E-02
C name: 316 SS
c density = 8 g/cc
```

```
m21     6012  -8.0000E-04  14028  -9.1874E-03
        14029  -4.8182E-04  14030  -3.3084E-04
        15031  -4.5000E-04  16032  -2.8415E-04
        16033  -2.3136E-06  16034   -1.3506E-05
        16036  -3.3651E-08  24050  -7.1035E-03
        24052  -1.4229E-01  24053  -1.6443E-02
        24054  -4.1619E-03  25055  -2.0000E-02
        26054  -3.6923E-02  26056  -6.0051E-01
        26057  -1.4124E-02  26058  -1.8981E-03
        28058  -8.0641E-02  28060  -3.2127E-02
        28061  -1.4202E-03  28062  -4.5961E-03
        28064  -1.2155E-03  42092  -3.5540E-03
        42094  -2.2635E-03  42095  -3.9371E-03
        42096  -4.1685E-03  42097  -2.4115E-03
        42098  -6.1561E-03  42100  -2.5071E-03
c
c name: 304 SS
c Density 8.0 g/cc
m22   6012 -0.0004   14028 -0.00461 14029 -0.00024
      14030 -0.00016
      15031 -0.00023 16032 -0.00014 16033 -1.1E-6
      16034 -6.4E-6 16036 -1.5E-8
      24050 -0.00826 24052 -0.1592 24053 -0.01805
      24054 -0.00449 25055 -0.01
      26054 -0.04105 26056 -0.64384
      26057 -0.01488 26058 -0.00196  28058 -0.06297
      28060 -0.02426 28061 -0.00105  28062 -0.00336
      28064 -0.0086
c
c c name: 17-4PH SS
c Density   7.75 g/cc
c not in PNNL lib
c from https://core.ac.uk/download/pdf/188225908.pdf
m23   26054 -0.0409  26056 -0.64142
      26057 -0.01482 26058 -0.00196  24050 -0.0076
      24052 -0.14663 24053 -0.01663  24054 -0.00414
      28058 -0.03404 28060 -0.01311 28061 -0.00057
      28062 -0.00182 28064 -0.00046 29000 -0.05
      14028 -0.00922  14029 -0.00047  14030 -0.00031
      25055 -0.01
      41093 -0.00225 73181 -0.00225
      6012  -0.0007  15031 -0.0004
      16032 -0.000028 16033 -2.3E-7
      16034 -1.3E-6 16036 -3E-8
c Materials for TARPOS and ENP on 90-124
c
c 409 SS rho=7.8 g/cm3
m27  6012  -7.8085e-02  6013  -9.1516e-04   14028 -9.0305e-01
     14029 -4.7515e-02  14030 -3.2438e-02   15031 -4.4000e-02
     16032 -4.1675e-02  16033 -3.3933e-04   16034 -1.9810e-03
     16036 -4.9355e-06  22046 -5.8371e-02   22047 -5.3785e-02
     22048 -5.4424e-01  22049 -4.0772e-02   22050 -3.9834e-02
     24050 -4.6453e-01  24052 -9.3157e-00   24053 -1.0767e-00
     24054 -2.7306e-01  25055 -9.8300e-01   26054 -4.8552e-00
```

```
     26056 -7.9035e+1   26057 -1.8579
     26058 -2.5159e-01
c
c NIF chamber
c
c    As-Built Al-5083 for Chamber
m101 6012  -4.9172E-04  7014  -1.8992E-05
     7015  -6.9765E-08  8016  -4.4624E-04
     12024 -3.4682E-02  12025  -4.5740E-03
     12026 -5.2248E-03  13027 -9.4652E-01
     14028 -9.2970E-04  14029 -4.7075E-05
     14030 -3.1249E-05  22046 -8.2624E-06
     22047 -7.5395E-06  22048 -7.6221E-05
     22049 -5.6804E-06  22050 -5.5771E-06
     23050 -8.4754E-08
     23051 -4.3092E-05  24050 -2.6669E-05
     24052 -5.1429E-04  24053 -5.8310E-05
     24054 -1.4516E-05  25055 -2.9764E-03
     26054 -1.0778E-04  26056 -1.6905E-03
     26057 -3.9060E-05  26058 -5.1589E-06
     28058 -1.7841E-04  28060 -6.8207E-05
     28061 -2.9530E-06  28062 -9.3817E-06
     28064 -2.6933E-04  29063 -3.3476E-04
     29065 -1.4921E-04  30066 -1.5664E-04
     30064 -5.6017E-04  30067 -2.3167E-05
     30068 -1.0738E-04  30070 -3.6547E-06
     31069 -5.7142E-05  31070 -3.8939E-05
     40090 -9.6392E-06  40091 -2.1255E-06
     40090 -3.2846E-06  40090 -3.4011E-06
     40090 -5.5961E-07
c
c    As-Built Gunite with 1 vol% A-615 steel rebar
m102 1001  -2.5091E-04  1002  -3.7642E-08
     3006  -1.0994E-06  3007  -1.3521E-05
     5010  -2.8718E-04  5011  -1.1559E-03
     6012  -4.2352E-05  7014  -1.1578E-05
     7015  -4.2532E-08  8016  -5.5987E-01
     9019  -2.7112E-05  11023 -5.6754E-03
     12024 -6.3061E-03  12025 -8.3165E-04
     12026 -9.4999E-04  13027 -4.3344E-02
     14028 -2.0919E-01  14029 -1.0592E-02
     14030 -7.0313E-03  15031 -3.8947E-04
     16032 -1.0850E-03  16033 -8.8341E-06
     16034 -5.1572E-05  16036 -1.2849E-07
     19039 -2.7490E-03  19040 -3.5373E-07
     19041 -2.0856E-04
     20040 -1.0239E-01  20041 -7.1747E-04
     20042 -1.5324E-04  20043 -2.4221E-03
     20046 -4.8580E-06  20048 -2.3699E-04
     22046 -1.2950E-04
     22047 -1.1817E-04  22048 -1.1946E-03
     22049 -8.9029E-05  22050 -8.7410E-05
     23050 -1.3618E-07  23051 -6.9239E-05
     24050 -1.9066E-05
```

```
     24052 -3.6767E-04  24053 -4.1686E-05
     24054 -1.0378E-05  25055 -3.0447E-04
     26054 -2.3809E-03  26056 -3.7342E-02
     26057 -8.6282E-04  26058 -1.1396E-04
     27059 -1.6865E-05  28058 -9.1495E-05
     28060 -3.4979E-05  28061 -1.5144E-06
     28062 -4.8113E-06  28064 -1.2196E-06
     29063 -7.1485E-05  29065 -3.1862E-05
     30064 -7.2433E-06  30066 -4.2126E-06
     30067 -6.2305E-07  30068 -2.8878E-06
     30070 -9.8289E-08  40090 -1.3828E-05
     40091 -3.0492E-06  40092 -4.7121E-06
     40094 -4.8792E-06  40096 -8.0282E-07
     42092 -9.8903E-06  42094 -6.1648E-06
     42095 -1.0610E-05  42096 -1.1117E-05
     42097 -6.3647E-06  42098 -1.6082E-05
     42100 -6.4180E-06  56138 -2.3182E-04
     74182 -9.6064E-06  74183 -5.2160E-06
     74184 -1.1214E-05  74186 -1.0447E-05
c
c    I-Beam and Flashing (SS-409 & Al-6061 mix)
m108 6012 -3.1819E-04   12024 -5.3005E-03
     12025 -6.9903E-04  12026 -7.9850E-04
     13027 -5.4786E-01  14028 -3.8774E-02
     14029 -1.9633E-03  14030 -1.3032E-03
     15031 -1.7898E-04  16032 -1.1301E-04
     16033 -9.2019E-07  16034 -5.3720E-06
     16036 -1.3384E-08
     22046 -3.1410E-04  22047 -2.8397E-04
     22048 -2.8262E-03  22049 -2.0814E-04
     22050 -2.0041E-04  24050 -2.0423E-03
     24052 -3.9368E-02  24053 -4.3967E-03
     24054 -1.1083E-03  25055 -4.8272E-03
     26054 -1.9960E-02  26056 -3.1328E-01
     26057 -7.2434E-03  26058 -9.5614E-04
     28058 -1.3523E-03  28060 -5.1707E-04
     28061 -2.2671E-05  28062 -7.2190E-05
     28064 -1.8495E-05  29063 -1.5674E-03
     29065 -6.9861E-04  30064 -6.8097E-04
     30066 -3.9603E-04  30067 -5.8575E-05
     30068 -2.7149E-04  30070 -9.2404E-06
c
c    Al-6061 for FW and Port Covers-den 0.28178
m126 12024 -9.3565E-03  12025 -1.2340E-03
     12026 -1.4095E-03  13027 -9.6710E-01
     14028 -3.6892E-03  14029 -1.8680E-04
     14030 -1.2400E-04  22046 -1.2000E-04
     22047 -1.0950E-04  22048 -1.1070E-03
     22049 -8.2500E-05  22050 -8.1000E-05
     24050 -1.7380E-05  24052 -3.3516E-04
     24053 -3.8000E-05  24054 -9.4600E-06
     25055 -1.5000E-03  26054 -4.0950E-04
     26056 -6.4225E-03  26057 -1.4840E-04
     26058 -1.9600E-05  29063 -2.7668E-03
```

```
     29065 -1.2332E-03  30064 -1.2020E-03
     30066 -6.9907E-04  30067 -1.0339E-04
     30068 -4.7922E-04  30070 -1.6311E-05
c
c    Pure SS-409 for FW-0.17826 g/cc
m131 6012  -0.0008   14028 -0.09223
     14029 -0.00467  14030 -0.0031
     15031 -0.00045  16032 -2.8415E-04
     16033 -2.3136E-06  16034 -1.3506E-05
     16036 -3.3651E-08
     22046 -6.188e-4 22047 -5.58e-4
     22048 -5.529e-3 22049 -4.058e-4
     22050 -3.885e-4 24050 -5.11e-3
     24052 -0.0985   24053 -0.011
     24054 -2.773e-3 25055 -0.01
     26054 -0.0496   26056 -0.7785
     26057 -0.018    26058 -2.376e-3
     28058 -0.0034   28060 -0.0013
     28061 -5.7e-5
     28062 -1.815e-4 28064 -4.65e-5
c
c   Al-6061 for FW and Port Covers-density 0.072047
m136 12024 -9.3565E-03  12025 -1.2340E-03
     12026 -1.4095E-03  13027 -9.6710E-01
     14028 -3.6892E-03  14029 -1.8680E-04
     14030 -1.2400E-04  22046 -1.2000E-04
     22047 -1.0950E-04  22048 -1.1070E-03
     22049 -8.2500E-05  22050 -8.1000E-05
     24050 -1.7380E-05  24052 -3.3516E-04
     24053 -3.8000E-05  24054 -9.4600E-06
     25055 -1.5000E-03  26054 -4.0950E-04
     26056 -6.4225E-03  26057 -1.4840E-04
     26058 -1.9600E-05  29063 -2.7668E-03
     29065 -1.2332E-03  30064 -1.2020E-03
     30066 -6.9907E-04  30067 -1.0339E-04
     30068 -4.7922E-04  30070 -1.6311E-05
c
c ******************************************************************************
c  Tallies
c ******************************************************************************
c
c The 129 STAYSL structure is used to bin tallies by energy
c
FC4 Neutron flux in each foil
F4:n 26 16 22 17 18 19 20 21 27
c
FC14 Foil pack neutron flux
F14:n (26 16 22 17 18 19 20 21 27)
T14 -1 0.3 0.4 0.5 0.6 0.7 0.8 0.9 1 2.4
       5.6 13.3 31.6 75 117 421 1E3 1E4 1E5 1E6 1E7 1E8 T
c
c  TLD Dose environment
c
FC194 Neutron Flux in TLDs
```

```
F194:n (28 29 30 31 32 33 34 35)
c
FC204 Gamma flux in TLDs
F204:p (28 29 30 31 32 33 34 35)
T204 -1 0.3 0.4 0.5 0.6 0.7 0.8 0.9 1 2.4
       5.6 13.3 31.6 75 117 421 1E3 1E4 1E5 1E6 1E7 1E8 T
c
FC6 TLD-100s Rads
F6:e (28 29 30 31)
FM6 1.6E-8 $ 1.6E-13 (J/MeV)*1000 (g/kg) * 100 Rad/(J/kg)
E6 0.001 0.01 0.1 0.3 0.5 1 3 6 10 T
T6 -1 0.3 0.4 0.5 0.6 0.7 0.8 0.9 1 2.4
        5.6 13.3 31.6 75 117 421 1E3 1E4 1E5 1E6 1E7 1E8 T
FC16 TLD-400s Rads
F16:e (32 33 34 35)
E16 0.001 0.01 0.1 0.3 0.5 1 3 6 10 T
FM16 1.6E-8 $ 1.6E-13 (J/MeV)*1000 (g/kg) * 100 Rad/(J/kg)
T16 -1 0.3 0.4 0.5 0.6 0.7 0.8 0.9 1 2.4
       5.6 13.3 31.6 75 117 421 1E3 1E4 1E5 1E6 1E7 1E8 T
E0    1.00E-10 1.00E-09 1.00E-08 2.30E-08 5.00E-08 7.60E-08 1.15E-07
      1.70E-07 2.55E-07 3.80E-07 5.50E-07 8.40E-07 1.28E-06 1.90E-06
      2.80E-06 4.25E-06 6.30E-06 9.20E-06 1.35E-05 2.10E-05 3.00E-05
      4.50E-05 6.90E-05 1.00E-04 1.35E-04 1.70E-04 2.20E-04 2.80E-04
      3.60E-04 4.50E-04 5.75E-04 7.60E-04 9.60E-04 1.28E-03 1.60E-03
      2.00E-03 2.70E-03 3.40E-03 4.50E-03 5.50E-03 7.20E-03 9.20E-03
      1.20E-02 1.50E-02 1.90E-02 2.55E-02 3.20E-02 4.00E-02 5.25E-02
      6.60E-02 8.80E-02 1.10E-01 1.35E-01 1.60E-01 1.90E-01 2.20E-01
      2.55E-01 2.90E-01 3.20E-01 3.60E-01 4.00E-01 4.50E-01 5.00E-01
      5.50E-01 6.00E-01 6.60E-01 7.20E-01 7.80E-01 8.40E-01 9.20E-01
      1.00E+00 1.20E+00 1.40E+00 1.60E+00 1.80E+00 2.00E+00 2.30E+00
      2.60E+00 2.90E+00 3.30E+00 3.70E+00 4.10E+00 4.50E+00 5.00E+00
      5.50E+00 6.00E+00 6.70E+00 7.40E+00 8.20E+00 9.00E+00 1.00E+01
      1.10E+01 1.20E+01 1.25E+01 1.26E+01 1.27E+01 1.28E+01 1.29E+01
      1.30E+01 1.31E+01 1.32E+01 1.33E+01 1.34E+01 1.35E+01 1.36E+01
      1.37E+01 1.38E+01 1.39E+01 1.40E+01 1.41E+01 1.42E+01 1.43E+01
      1.44E+01 1.45E+01 1.46E+01 1.47E+01 1.48E+01 1.49E+01 1.50E+01
      1.51E+01 1.52E+01 1.53E+01 1.54E+01 1.55E+01 1.56E+01 1.57E+01
      1.58E+01 1.59E+01 1.60E+01 1.65E+01
c ****************************************************************************
c  Source
c ****************************************************************************
SDEF PAR=n ERG=d2 POS=0.0 0.0 0.0 VEC=0 0 1
#   SI2           SP2      $ Source Spectrum at 8.8 keV
     12 0
     13.293734   0.002595846
     13.300679   0.003143204
     13.307623   0.002889355
     13.314679   0.002759715
     13.321623   0.002483202
     13.32868    0.003331836
     13.335624   0.003136216
     13.342681   0.003876888
     13.349737   0.004195655
     13.356681   0.005649322
```

13.363737 0.005300441
13.370794 0.006930848
13.37785 0.007653055
13.384906 0.00851353
13.391963 0.009769057
13.399019 0.010848302
13.406075 0.012312101
13.413131 0.013816193
13.420188 0.016330301
13.427244 0.017058896
13.434413 0.020332808
13.441469 0.021960488
13.448525 0.024317447
13.455693 0.02767652
13.462749 0.030190186
13.469918 0.033245179
13.476974 0.037478468
13.484143 0.040225076
13.491199 0.045002486
13.498367 0.048312375
13.505536 0.053851827
13.512704 0.057794339
13.519872 0.062981459
13.52704 0.068019167
13.534096 0.072999321
13.541265 0.079126902
13.548433 0.084435887
13.555602 0.090912806
13.562882 0.09726935
13.57005 0.103931106
13.577219 0.111946124
13.584499 0.118574191
13.591667 0.126535885
13.598836 0.135553155
13.606116 0.144238874
13.613284 0.153834737
13.620564 0.163638024
13.627733 0.174292174
13.635013 0.1849865
13.642294 0.196753888
13.649574 0.208705504
13.656742 0.220375206
13.664022 0.234296088
13.671302 0.246205409
13.678583 0.260060475
13.685863 0.273628735
13.693143 0.286661812
13.700424 0.301668064
13.707704 0.315797348
13.715097 0.3309202
13.722377 0.345761666
13.729657 0.361859544
13.73705 0.375991736
13.74433 0.39370984

```
13.75161    0.408915836
13.759002   0.426673092
13.766395   0.444122663
13.773676   0.461266708
13.781067   0.479402036
13.788459   0.497768413
13.795852   0.516483686
13.803133   0.535692132
13.810525   0.553330984
13.817917   0.574804199
13.825309   0.591414318
13.832702   0.612693771
13.840094   0.629757256
13.847599   0.647931278
13.854991   0.667136746
13.862383   0.686153621
13.869887   0.702200377
13.87728    0.718374858
13.884672   0.736399535
13.892176   0.751940461
13.899569   0.769925528
13.907073   0.783763805
13.914577   0.801664257
13.92197    0.814040877
13.929474   0.831758654
13.936978   0.846252302
13.944482   0.861173281
13.951875   0.876988988
13.95938    0.891525385
13.966883   0.905805581
13.974388   0.918552129
13.982005   0.932538345
13.989508   0.942551909
13.997013   0.956277605
14.004517   0.96244804
14.012022   0.973337133
14.019638   0.978880392
14.027142   0.985519206
14.034759   0.98989348
14.042263   0.992173132
14.04988    0.996759419
14.057496   0.997497018
14.065  1
14.072616   0.996662734
14.080232   0.996470346
14.087849   0.993580199
14.095465   0.990116876
14.103081   0.986994992
14.110698   0.980789396
14.118314   0.97693289
14.12593    0.969654208
14.133547   0.963141516
14.141163   0.955640158
14.148892   0.94741036
```

```
14.156508   0.938571636
14.164237   0.930606511
14.171853   0.919773513
14.179469   0.90987253
14.187197   0.898443951
14.194926   0.887038367
14.202542   0.873846335
14.210271   0.860616688
14.217999   0.846330475
14.225727   0.831016542
14.233455   0.81601533
14.241184   0.799979335
14.248912   0.783495796
14.25664    0.767566069
14.264369   0.75204166
14.272097   0.735017162
14.279826   0.717840638
14.287666   0.701943946
14.295395   0.684070446
14.303122   0.666239467
14.310963   0.647928236
14.318803   0.629289106
14.326531   0.610350437
14.334372   0.591796708
14.3421 0.572979287
14.349941   0.554141195
14.357781   0.535963543
14.365621   0.517752954
14.373461   0.4997812
14.381302   0.48231606
14.389143   0.465155529
14.396983   0.447876531
14.404823   0.431848287
14.412663   0.415109298
14.420503   0.399173684
14.428456   0.383147141
14.436296   0.367503511
14.444249   0.351596026
14.452089   0.336258053
14.459929   0.320678066
14.467882   0.30564627
14.475834   0.290574556
14.483786   0.276366443
14.491626   0.262220589
14.499579   0.249067777
14.507532   0.235978288
14.515483   0.223374951
14.523436   0.211437616
14.531389   0.199795447
14.539341   0.188815822
14.547293   0.178120231
14.555358   0.167967573
14.56331    0.158189867
14.571262   0.148721641
```

```
      14.579326   0.139713503
      14.587279   0.131114934
      14.595343   0.122845385
      14.603296   0.115100811
      14.61136    0.107690306
      14.619424   0.100738963
      14.627377   0.094133932
      14.635441   0.087902156
      14.643506   0.081992162
      14.65157    0.076393198
      14.659634   0.071127009
      14.667699   0.066164418
      14.675763   0.06145838
      14.683827   0.057066199
      14.692004   0.052886633
      14.700068   0.048967563
      14.708132   0.045290071
      14.716308   0.041805197
      14.724373   0.038540419
      14.732549   0.035480531
      14.740614   0.032626086
      14.74879    0.029955985
      14.756966   0.027492629
      14.765031   0.0251978
      14.773207   0.023092789
      14.781383   0.021151086
      14.78956    0.019392379
      14.797736   0.017770848
      14.805913   0.016316756
      14.814089   0.014966334
      14.822378   0.013754329
      14.830554   0.012646631
      14.83873    0.011642544
      14.846906   0.010734519
      14.855195   0.009914765
      14.863483   0.009159488
      14.87166    0.008461644
      14.879836   0.007811633
      14.888124   0.007239409
c ADVANTG
sb2    0.00000e+00 2.78870e-05 3.54303e-05 3.25689e-05 3.11076e-05 2.79907e-05
       3.75566e-05 3.53515e-05 4.37004e-05 4.72936e-05 6.36794e-05 5.97468e-05
       7.81248e-05 8.62655e-05 9.59648e-05 1.10117e-04 1.22282e-04 1.38782e-04
       1.55737e-04 1.84076e-04 1.92288e-04 2.29192e-04 2.47539e-04 2.74107e-04
       3.11971e-04 3.40305e-04 3.74741e-04 4.22459e-04 4.53418e-04 5.07270e-04
       5.44579e-04 6.07020e-04 6.51460e-04 7.09929e-04 7.66714e-04 8.22851e-04
       8.91921e-04 9.51764e-04 1.02477e-03 1.09642e-03 1.17152e-03 1.26186e-03
       1.33657e-03 1.42632e-03 1.52796e-03 1.62587e-03 1.73403e-03 1.84453e-03
       1.96463e-03 2.08517e-03 2.21782e-03 2.35254e-03 2.48408e-03 2.64099e-03
       2.77524e-03 2.93141e-03 3.08435e-03 3.23126e-03 3.40041e-03 3.55968e-03
       3.73014e-03 3.89744e-03 4.07889e-03 4.23819e-03 4.43791e-03 4.60931e-03
       4.80947e-03 5.00617e-03 5.19941e-03 5.40384e-03 5.61086e-03 5.82182e-03
       6.03834e-03 6.23717e-03 6.47921e-03 6.66644e-03 6.90631e-03 7.10677e-03
       7.95845e-03 8.19435e-03 8.42793e-03 8.62503e-03 8.82370e-03 9.04510e-03
```

```
      9.23598e-03 9.45689e-03 9.62686e-03 9.84673e-03 9.99875e-03 1.02164e-02
      1.03944e-02 1.05777e-02 1.07719e-02 1.09505e-02 1.11259e-02 1.12825e-02
      1.14542e-02 1.15772e-02 1.17458e-02 1.18216e-02 1.19554e-02 1.20235e-02
      1.21050e-02 1.21587e-02 1.21867e-02 1.22431e-02 1.22521e-02 1.22829e-02
      1.22419e-02 1.22395e-02 1.22040e-02 1.21615e-02 1.21231e-02 1.20469e-02
      1.19995e-02 1.19101e-02 1.18301e-02 1.17380e-02 1.16369e-02 1.15283e-02
      1.14305e-02 1.12975e-02 1.11758e-02 1.10355e-02 1.11788e-02 1.12924e-02
      1.11214e-02 1.09368e-02 1.07389e-02 1.05451e-02 1.03378e-02 1.01248e-02
      9.91897e-03 9.71835e-03 9.49835e-03 9.27638e-03 9.07096e-03 8.83998e-03
      8.60956e-03 8.37293e-03 8.13207e-03 7.88733e-03 7.64757e-03 7.40439e-03
      7.16096e-03 6.92605e-03 6.69073e-03 6.45848e-03 6.23279e-03 6.01103e-03
      5.78774e-03 5.58061e-03 5.36430e-03 5.15837e-03 4.95127e-03 4.74911e-03
      4.54354e-03 4.34534e-03 4.14400e-03 3.94975e-03 3.75499e-03 3.57138e-03
      3.38858e-03 3.21861e-03 3.04946e-03 2.88659e-03 2.73233e-03 2.58188e-03
      2.44000e-03 2.30178e-03 2.17058e-03 2.04423e-03 1.92187e-03 1.80546e-03
      1.69435e-03 1.58748e-03 1.48740e-03 1.39164e-03 1.30181e-03 1.21646e-03
      1.13593e-03 1.05955e-03 9.87200e-04 9.19147e-04 8.55018e-04 7.94203e-04
      7.37445e-04 6.83434e-04 6.32789e-04 5.85266e-04 5.40233e-04 4.98043e-04
      4.58501e-04 4.21615e-04 3.87110e-04 3.55277e-04 3.25622e-04 2.98419e-04
      2.73327e-04 2.50600e-04 2.29646e-04 2.10855e-04 1.93404e-04 1.77742e-04
      1.63428e-04 1.50452e-04 1.38718e-04 1.28125e-04 1.18365e-04 1.09347e-04
      1.00947e-04 9.35521e-05
wwp:n 5.0 j 100 j -1 0 2.741987751e-06
```

# Appendix E. Unstructured Mesh Density Adjusting Script

```
# -*- coding: utf-8 -*-
"""
Created on Sat Aug 21 20:23:23 2021

@author: Micah Jeroutek
"""
import numpy as np
import re
import os, sys
fdir = os.path.dirname(__file__)
sys.path.append(fdir)

#%%============================================================================
"""============================================================================"""
'''                              CONTROLLER                                  '''
"""============================================================================"""
# Enter name of the log file for the mesh pre-deformation
f1 = 'vols_pre.txt'

# Enter name of the log file for the deformed mesh
f2 = 'vols_post.txt'

# Enter name of the Abaqus input deck for the deformed mesh
# NOTE: Abaqus input deck must be in the standard CUBIT-exported format
input_deck = 'cube_deformed_cubit.inp'

# Enter name of the new input deck to be made once (made using journal)
jou_input_deck = 'test_export2.inp'

# Enter name of the new input deck to be made once (written from scratch)
new_input_deck = 'density_adjusted_crater.inp'

# Enter the number of density bins that may be used to stratify mesh
den_bins = 10

# Enter material density to be used in MCNP data cards
mat_dens = 1.52

# Enter type of elements being used
TET = True



#==============================================================================
#%%
'''
Figuring out factors by which to change density from log files
'''

# Reading each line of the CUBIT log files with elemental volume data
# ----------------------------------------------------------------------
log_file = open(fdir+f'\{f1}', 'rt')  # initialize reading
# whole_file1  = log_file.read()        # create str of entire input deck
```

```
all_lines1   = []                     # list for each individual line in the file

with open(fdir+f'\{f1}', 'rt') as log_file:
    for each_line in log_file:
        all_lines1.append(each_line)

log_file = open(fdir+f'\{f2}', 'rt')  # initialize reading
# whole_file2  = log_file.read()        # create str of entire input deck
all_lines2   = []                     # list for each individual line in the file

with open(fdir+f'\{f2}', 'rt') as log_file:
    for each_line in log_file:
        all_lines2.append(each_line)

# Extracting volumes of each element in both meshes from log files
# ----------------------------------------------------------------
volumes1 = []
for i in range(len(all_lines1)):
    if re.findall(r'Element␣Volume', all_lines1[i]) == ['Element␣Volume']:
        value = float(all_lines1[i][20:30])
        if value < 0:
            value *= -1
        volumes1.append(value)

volumes2 = []
for i in range(len(all_lines2)):
    if re.findall(r'Element␣Volume', all_lines2[i]) == ['Element␣Volume']:
        value = float(all_lines2[i][20:30])
        if value < 0:
            value *= -1
        volumes2.append(value)

# Taking ratio of element volumes to later separate by density
# ------------------------------------------------------------
ratios = np.array(volumes2) / np.array(volumes1)
density_factors = 1 / ratios

# Binning densities to reduce computing time
# ------------------------------------------
bins = np.array([])
bins = np.append(bins, np.linspace(0.1, 0.89, int(den_bins/5)))
bins = np.append(bins, np.linspace(0.9, 0.99, int(den_bins/5)))
bins = np.append(bins, np.linspace(1, 1.09, int(den_bins/5)))
bins = np.append(bins, np.linspace(1.1, 10, int(den_bins/5)))
bins = np.append(bins, np.linspace(11, 100, int(den_bins/10)))
bins = np.append(bins, np.linspace(101, 1000, int(den_bins/10)))
bins = np.append(bins, 1e9)

binned_den = np.digitize(density_factors, bins)
avg_dens = np.array([])
new_dens_factors = np.zeros(len(binned_den))

for b in range(len(bins)):  # finding average density factors for each bin
    avg_dens_per_bin = []
```

```
    for i in range(len(binned_den)):
        if binned_den[i] == b:
            avg_dens_per_bin.append(density_factors[i])
    average_dens = np.mean(avg_dens_per_bin)
    avg_dens = np.append(avg_dens, average_dens)

for i in range(len(binned_den)):
    if i != len(binned_den)-1:
        new_dens_factors[i] = avg_dens[int(binned_den[i])]
    elif i == len(binned_den)-1:
        new_dens_factors[i] = density_factors[i]

new_dens_factors *= mat_dens    # multiplying by actual material density


#%%
'''
Editting input deck for deformed mesh to account for variable density
'''

# Reading each line of the CUBIT-exported Abaqus input deck
# ----------------------------------------------------------
abaqus_input = open(fdir+f'\{input_deck}', 'rt')  # initialize reading
# whole_file3  = abaqus_input.read()       # create str of entire input deck
all_lines3   = []     # list for each individual line in the file
node_start   = []     # list for the start of each part's node section
elem_start   = []     # list for the start of each part's element section
comments     = []     # list for all comment lines in the file

# filling in list with each line in the file individually
# -------------------------------------------------------
with open(fdir+f'\{input_deck}', 'rt') as abaqus_input:
    for each_line in abaqus_input:
        all_lines3.append(each_line)

# parsing through file to index nodes, elements, and comments
# -----------------------------------------------------------
for i in range(len(all_lines3)):
    if all_lines3[i] == '*NODE, NSET=ALLNODES\n':
        node_start.append(i)
    elif re.findall(r'ELEMENT, TYPE=', all_lines3[i]) == ['ELEMENT, TYPE=']:
        elem_start.append(i)
    elif all_lines3[i] == '**\n':
        comments.append(i)


# finding where each node and element section ends
# ------------------------------------------------
node_end = []  # list for the end of each part's node section
elem_end = []  # list for the end of each part's element section

for i in range(len(node_start)):
    # used to find first comment line after node and element sections
    node_end_finder = []
```

```
    elem_end_finder = []

    for j in range(len(comments)):
        # making sure comment lines appear after each section
        if (comments[j] > node_start[i]):
            node_end_finder.append(comments[j] - node_start[i])
        if (comments[j] > elem_start[i]):
            elem_end_finder.append(comments[j] - elem_start[i])

    # appending the end of each section to a list
    node_end.append(min(node_end_finder) + node_start[i])
    elem_end.append(min(elem_end_finder) + elem_start[i])

# finding where each node and element section ends
# -----------------------------------------------
node_end = []  # list for the end of each part's node section
elem_end = []  # list for the end of each part's element section

for i in range(len(node_start)):
    # used to find first comment line after node and element sections
    node_end_finder = []
    elem_end_finder = []

    for j in range(len(comments)):
        # making sure comment lines appear after each section
        if (comments[j] > node_start[i]):
            node_end_finder.append(comments[j] - node_start[i])
        if (comments[j] > elem_start[i]):
            elem_end_finder.append(comments[j] - elem_start[i])

    # appending the end of each section to a list
    node_end.append(min(node_end_finder) + node_start[i])
    elem_end.append(min(elem_end_finder) + elem_start[i])

# setting up numpy array to store node positions
# ----------------------------------------------
node_array = np.zeros([node_end[0] - node_start[0] - 1, 4])

for i in range(len(node_start)):
    for j in range(node_start[i]+1, node_end[i]):
        node_number = j - node_start[i]

        # determining position of current node in loop (Cartesian coordinates)
        position  = re.findall(r'\b\d+|-\d+\b', all_lines3[j])

        node_xpos = float(position[1] + '.' + position[2]) * 10 ** \
                    float(position[3])

        node_ypos = float(position[4] + '.' + position[5]) * 10 ** \
                    float(position[6])

        node_zpos = float(position[7] + '.' + position[8]) * 10 ** \
                    float(position[9])
```

```
        node_array[j - node_start[i] - 1,0] = node_number
        node_array[j - node_start[i] - 1,1] = node_xpos
        node_array[j - node_start[i] - 1,2] = node_ypos
        node_array[j - node_start[i] - 1,3] = node_zpos

# setting up numpy array to store nodal connectivities of elements
# -----------------------------------------------------------------
# If 2nd order TET elements are used in UM
if TET:
    elem_array = np.zeros([elem_end[0] - elem_start[0] - 1, 11])

    for i in range(len(elem_start)):
        for j in range(elem_start[i]+1, elem_end[i]):

            # determining all nodes per element
            nodes_in_elem = re.findall(r'\b\d+\b', all_lines3[j])
            elem_number = int(nodes_in_elem[0])
            node1  = float(nodes_in_elem[1])
            node2  = float(nodes_in_elem[2])
            node3  = float(nodes_in_elem[3])
            node4  = float(nodes_in_elem[4])
            node5  = float(nodes_in_elem[5])
            node6  = float(nodes_in_elem[6])
            node7  = float(nodes_in_elem[7])
            node8  = float(nodes_in_elem[8])
            node9  = float(nodes_in_elem[9])
            node10 = float(nodes_in_elem[10])

            elem_array[j - elem_start[i] - 1,0] = elem_number
            elem_array[j - elem_start[i] - 1,1] = node1
            elem_array[j - elem_start[i] - 1,2] = node2
            elem_array[j - elem_start[i] - 1,3] = node3
            elem_array[j - elem_start[i] - 1,4] = node4
            elem_array[j - elem_start[i] - 1,5] = node5
            elem_array[j - elem_start[i] - 1,6] = node6
            elem_array[j - elem_start[i] - 1,7] = node7
            elem_array[j - elem_start[i] - 1,8] = node8
            elem_array[j - elem_start[i] - 1,9] = node9
            elem_array[j - elem_start[i] - 1,10] = node10

# If HEX elements are used in UM
else:
    elem_array = np.zeros([elem_end[0] - elem_start[0] - 1, 9])

    for i in range(len(elem_start)):
        for j in range(elem_start[i]+1, elem_end[i]):

            # determining all nodes per element
            nodes_in_elem = re.findall(r'\b\d+\b', all_lines3[j])
            elem_number = int(nodes_in_elem[0])
            node1 = float(nodes_in_elem[1])
            node2 = float(nodes_in_elem[2])
            node3 = float(nodes_in_elem[3])
            node4 = float(nodes_in_elem[4])
```

```
            node5 = float(nodes_in_elem[5])
            node6 = float(nodes_in_elem[6])
            node7 = float(nodes_in_elem[7])
            node8 = float(nodes_in_elem[8])

            elem_array[j - elem_start[i] - 1,0] = elem_number
            elem_array[j - elem_start[i] - 1,1] = node1
            elem_array[j - elem_start[i] - 1,2] = node2
            elem_array[j - elem_start[i] - 1,3] = node3
            elem_array[j - elem_start[i] - 1,4] = node4
            elem_array[j - elem_start[i] - 1,5] = node5
            elem_array[j - elem_start[i] - 1,6] = node6
            elem_array[j - elem_start[i] - 1,7] = node7
            elem_array[j - elem_start[i] - 1,8] = node8


#%%
'''
Creating journal files for CUBIT to split volume into parts by density
'''

# Separating volume into multiple blocks through journal
# ------------------------------------------------------
journal_file = 'delete␣block␣all\n'
instance_txt = ''

for b in range(len(bins)):
    if b in binned_den:
        if TET:
            journal_file += f'block␣{b+1:.0f}␣add␣tet␣'
        else:
            journal_file += f'block␣{b+1:.0f}␣add␣hex␣'
        for i in range(len(binned_den)):
            if binned_den[i] == b:
                journal_file += f'{elem_array[i][0]:.0f}␣'
                # print(f'Element Number: {elem_array[i][0]+1:.0f}')
        journal_file += '\n'
        instance_txt += f'instance␣block␣{b+1}␣source_csys␣0␣target_csys␣0␣'


# Renumbering elements for journal file
# -------------------------------------
bins_used = []
for b in range(len(bins)):
    if b in binned_den:
        bins_used.append(b)

volumes = np.zeros(len(bins_used))
for i in range(0, len(bins_used)):
    volumes[i] = int(1)

journal_file += 'renumber␣node␣all␣in␣volume␣all␣start_id␣90000000\n'
journal_file += 'renumber␣element␣all␣in␣volume␣all␣start_id␣90000000\n'
```

```
for i in range(0, len(volumes)):
    elem_list2 = []
    for b in range(len(bins)):
        if b in binned_den:
            elem_list = []
            for j in range(len(binned_den)):
                if binned_den[j] == b:
                    elem_list.append(elem_array[i][0])
            elem_list2.append(elem_list)
    if i == 0:
        S = 1
    else:
        S += len(elem_list2[i-1])
    if i == 0:
        node = 1
    else:
        node = 40000*i

    journal_file += f'renumber␣block␣{bins_used[i]+1}␣start_id␣1␣node_start_id␣{node}␣elem_start_id␣{int(S)}\n'
journal_file += 'renumber␣node␣all␣in␣volume␣all␣start_id␣100000000\n'
journal_file += 'renumber␣node␣all␣in␣volume␣all␣start_id␣1\n'

# Adding export settings to journal file
# ---------------------------------------
journal_file += 'export␣abaqus␣"' + fdir + f'\{jou_input_deck}' + \
                '"␣block␣all␣' + instance_txt + '␣overwrite'

write_input  = open(fdir+r'\split_vol.jou', 'w+')  # initialize writing
write_input2 = write_input.write(journal_file)


#%%
'''
Creating adjusted Abaqus input deck from scratch
'''
elem_count = 1   # used to renumber elements for set-material elsets

new_input = f'*HEADING\nVaried␣Density␣Model␣of␣{new_input_deck}\nversion:␣15.6\n**\n'

# NOTE: If two separate volumes have contiguous elements, nodes on the
#       superimposed faces must be assigned to BOTH volumes.
# 2nd order TET Elements (Type = C3D10) (C3D4 if 1st order)
# --------------------------------------
if TET:
    for b in range(len(bins)):
        connect_4_bins = []     # list storing nodal connectivities by bin
        if b in binned_den:
            # print()
            # print(f'Current Bin: {b}')
            new_input += '**********************************␣P␣A␣R␣T␣S␣***********' + \
                         f'**********************\n*PART,␣NAME=PART-{b+1}\n**\n'

            for i in range(len(binned_den)):
                if binned_den[i] == b:
```

```
                for j in range(1, 11):

                    node = int(elem_array[i][j])
                    connect_4_bins.append(node)

            connect_4_bins = list(set(connect_4_bins))

            new_input += '**********␣N␣O␣D␣E␣S␣*****' + \
                         '**********\n*NODE,␣NSET=ALLNODES\n'
            for i in range(len(connect_4_bins)):
                new_input += f'␣␣␣␣␣␣␣␣{node_array[connect_4_bins[i]-1,0]:6.0f},␣␣␣␣{node_array[connect_4_bins[i
                    ]-1,1]:2.6e},␣␣␣␣{node_array[connect_4_bins[i]-1,2]:2.6e},␣␣␣␣{node_array[connect_4_bins[i
                    ]-1,3]:2.6e}\n'

            new_input += '**\n**********␣E␣L␣E␣M␣E␣N␣T␣S␣****' + \
                         f'**********\n*ELEMENT,␣TYPE=C3D10,␣ELSET=BIN{b+1}\n'

            elem_count_start = elem_count   # used for elsets on each

            for i in range(len(binned_den)):
                if binned_den[i] == b:
                        new_input += f'␣␣␣␣␣␣␣{elem_count:6.0f},' + \
                                     f'␣␣␣␣␣␣{elem_array[i,1]:6.0f},' + \
                                     f'␣␣␣␣␣␣{elem_array[i,2]:6.0f},' + \
                                     f'␣␣␣␣␣␣{elem_array[i,3]:6.0f},' + \
                                     f'␣␣␣␣␣␣{elem_array[i,4]:6.0f},' + \
                                     f'␣␣␣␣␣␣{elem_array[i,5]:6.0f},' + \
                                     f'␣␣␣␣␣␣{elem_array[i,6]:6.0f},' + \
                                     f'␣␣␣␣␣␣{elem_array[i,7]:6.0f},' + \
                                     f'␣␣␣␣␣␣{elem_array[i,8]:6.0f},' + \
                                     f'␣␣␣␣␣␣{elem_array[i,9]:6.0f},' + \
                                     f'␣␣␣␣␣␣{elem_array[i,10]:6.0f}\n'
                        elem_count += 1
            new_input += f'**\n**********␣P␣R␣O␣P␣E␣R␣T␣I␣E␣S␣**********\n'
            if b < 9:
                new_input += f'*Elset,␣elset=Set-material_00{b+1},␣generate' + \
                             f'\n␣␣{int(elem_count_start)},␣{int(elem_count)-1},␣␣␣1\n'
                new_input += f'*Elset,␣elset=Set-statistic_00{b+1},␣generate' + \
                             f'\n␣␣{int(elem_count_start)},␣{int(elem_count)-1},␣␣␣1\n'

            else:
                new_input += f'*Elset,␣elset=Set-material_0{b+1},␣generate' + \
                             f'\n␣␣{int(elem_count_start)},␣{int(elem_count)-1},␣␣␣1\n'
                new_input += f'*Elset,␣elset=Set-statistic_0{b+1},␣generate' + \
                             f'\n␣␣{int(elem_count_start)},␣{int(elem_count)-1},␣␣␣1\n'

            new_input += '**\n*END␣PART\n**\n**\n'

        else:
            continue

# HEX Elements (Type = C3D8R)
# ---------------------------
else:
```

```
    for b in range(len(bins)):
        if b in binned_den:
            new_input += '**********************************␣P␣A␣R␣T␣S␣***********' + \
                         f'**********************\n*PART,␣NAME=PART-{b+1}\n**\n'
            connect_4_bins = []     # list storing nodal connectivities by bin
            for i in range(len(binned_den)):
                if binned_den[i] == b:
                    for j in range(1, 9):

                        node = int(elem_array[i][j] - 1)
                        connect_4_bins.append(node)

            connect_4_bins = list(set(connect_4_bins))

            new_input += '**********************************␣N␣O␣D␣E␣S␣*****' + \
                         '*****************************\n*NODE,␣NSET=ALLNODES\n'
            for i in range(len(connect_4_bins)):
                new_input += f'␣␣␣␣␣␣␣{node_array[connect_4_bins[i]-1,0]:6.0f},␣␣␣␣{node_array[connect_4_bins[i
                     ]-1,1]:2.6e},␣␣␣␣{node_array[connect_4_bins[i]-1,2]:2.6e},␣␣␣␣{node_array[connect_4_bins[i
                     ]-1,3]:2.6e}\n'

            new_input += '**\n**********************************␣E␣L␣E␣M␣E␣N␣T␣S␣****' + \
                         f'************************\n*ELEMENT,␣TYPE=C3D8R,␣ELSET=BIN{b+1}\n'

            for i in range(len(binned_den)):
                if binned_den[i] == b:
                        new_input += f'␣␣␣␣␣␣␣{elem_array[i,0]:6.0f},' + \
                                     f'␣␣␣␣␣␣{elem_array[i,1]:6.0f},' + \
                                     f'␣␣␣␣␣␣{elem_array[i,2]:6.0f},' + \
                                     f'␣␣␣␣␣␣{elem_array[i,3]:6.0f},' + \
                                     f'␣␣␣␣␣␣{elem_array[i,4]:6.0f},' + \
                                     f'␣␣␣␣␣␣{elem_array[i,5]:6.0f},' + \
                                     f'␣␣␣␣␣␣{elem_array[i,6]:6.0f},' + \
                                     f'␣␣␣␣␣␣{elem_array[i,7]:6.0f},' + \
                                     f'␣␣␣␣␣␣{elem_array[i,8]:6.0f}\n'
            new_input += f'**\n**********************************␣P␣R␣O␣P␣E␣R␣T␣I␣E␣S␣**********************\n*
                 SOLID␣SECTION,␣ELSET=BIN{b+1},␣MATERIAL=Default-Steel\n**\n*END␣PART\n**\n**\n'
        else:
            continue

new_input += '**\n**\n**\n**********************************␣E␣N␣D␣␣␣P␣A␣R␣T␣S␣
     **********************************\n**\n**\n**********************************␣A␣S␣S␣E␣M␣B␣L␣Y␣
     ************************************\n**\n*ASSEMBLY,␣NAME=ASSEMBLY1\n**\n'

for b in range(len(bins)):
    if b in binned_den:
        new_input += f'*INSTANCE,␣NAME=PART-{b+1}_1,␣PART=PART-{b+1}\n'
        new_input += '0.000000e+00,0.000000e+00,0.000000e+00\n'
        new_input += '0.000000e+00,0.000000e+00,0.000000e+00,0.000000e+00,0.000000e+00,1.000000e+00,0.000000e+00\
             n'
        new_input += '*END␣INSTANCE\n'

new_input += '**\n*END␣ASSEMBLY\n**\n**\n**\n'
```

```
for b in range(len(bins)):
    if b in binned_den:
        if b < 9:
            new_input +=f'*Material, name=Material_00{b+1}\n'
        else:
            new_input +=f'*Material, name=Material_0{b+1}\n'


new_input += '**\n'

for b in range(len(bins)):
    if b in binned_den:
        new_input += f'** New Density for MATERIAL {b+1} = {avg_dens[b]:1.3f} g/cc\n'

#%%
'''
Writing new Abaqus input deck for deformed mesh to new file
(NOTE: File named using controller at top of code)
'''
write_input = open(fdir+f'\{new_input_deck}', 'w+')  # initialize writing

write_input2 = write_input.write(new_input)
```

# Appendix F. Deformed Plate Homogeneous TET MCNP Input Deck

```
cubit(arter/Research/Files for MCNP Runs/plate_assembly_TET.inp): 01/19/2022: 11
c
c  Created from file    : plate_assembly_TET.inp
c  Created on           :  1-19-2022 @ 12:18:56
c
c
c PSEUDO CELLS
01       2     -2.6989       0  u=1    imp:p=1  $ Detector casing
02       7     -9.1400       0  u=1    imp:p=1  $ Copper plate 1
03       7     -9.1400       0  u=1    imp:p=1  $ Copper plate 2
04       7     -9.1400       0  u=1    imp:p=1  $ Copper plate 3
05       7     -9.1400       0  u=1    imp:p=1  $ Copper plate 4
06       7     -9.1400       0  u=1    imp:p=1  $ Copper plate 5
07       7     -9.1400       0  u=1    imp:p=1  $ Copper plate 6
08       7     -9.1400       0  u=1    imp:p=1  $ Copper plate 7
09       2     -2.6989       0  u=1    imp:p=1  $ Detector front face
10       4     -5.8000       0  u=1    imp:p=1  $ CZT crystal
11       3     -1.0840       0  u=1    imp:p=1  $ Source stand
12       5     -1.2990       0  u=1    imp:p=1  $ Source epoxy well
13       6     -1.1900       0  u=1    imp:p=1  $ Source plastic shell
14       2     -2.6989       0  u=1    imp:p=1  $ Aluminum Base Plate
15       2     -2.6989       0  u=1    imp:p=1  $ Crossbeam
16       2     -2.6989       0  u=1    imp:p=1  $ Upright 1
17       2     -2.6989       0  u=1    imp:p=1  $ Upright 2
18       3     -1.0840       0  u=1    imp:p=1  $ Detector Saddle
19       1     -0.001205     0  u=1    imp:p=1  $ Inferred Background
c
c LEGACY CELLS
20       0          -99  fill=1 imp:p=1  $ Mesh universe fill cell
21       0           99         imp:p=0  $ FATALITY

c
c SURFACES
99  sph   1.27000E+02   6.17499E+01   6.28650E+01   2.87630E+02

c
c  DATA CARDS
mode p
nps 5e7
sdef erg=0.662 pos=volumer   $ volumetric Cs-137 source
c
embed1 meshgeo=abaqus
       mgeoin=plate_assembly_TET.inp
       meeout=plate_assembly_TET.eeout
       length= 1.00000E-01
       background=      19
       matcell=  1  1  2  2  3  3  4  4  5  5  6  6  7  7  8  8  9  9 10 10
                11 11 12 12 13 13 14 14 15 15 16 16 17 17 18 18
c
c  MATERIAL CARDS
```

```
c Air (density = 0.001205 g/cc)
m1     6000  -0.000124
       7000  -0.755268
       8000  -0.231781
      18000  -0.012827
c Aluminum (density = 2.6989 g/cc)
m2    13000  -1.000000
c Nylon 6 (density = 1.084 g/cc)
m3     1000  11.0
       6000   6.0
           7000   1.0
           8000   1.0
c CZT detector crystal (density = 5.8 g/cc)
m4    30000   0.05
      48000   0.45
      52000   0.50
c Epoxy Well in Source (density = 1.299 g/cc)
m5     1000   0.576
       6000   0.288
           8000   0.036
          17000   0.050
          55000   0.050
c Cast Acrylic Button Source (density = 1.19 g/cc)
m6     1000   8.0
       6000   5.0
           8000   2.0
c 110 Copper (original density = 8.93 g/cc)
m7     8000   0.0004
      29000   0.9996
c
c  TALLY CARDS
f8:p 9 10         $ pulse height tally in CZT detector
e8 0 0.661 0.663
```

# Appendix G. Deformed Plate Variable Density TET MCNP Input Deck

```
cubit(arter/Research/Files for MCNP Runs/plate_assembly_TET.inp): 01/19/2022: 11
c
c  Created from file    : plate_assembly_TET.inp
c  Created on           :  1-19-2022 @ 12:18:56
c
c
c PSEUDO CELLS
01       2     -2.6989       0  u=1    imp:p=1  $ Detector casing
02       7     -7.8511       0  u=1    imp:p=1  $ Copper plate 1 (rho= 7.8511 g/cc)
03       7     -7.9900       0  u=1    imp:p=1  $ Copper plate 2 (rho= 7.9900 g/cc)
04       7     -8.6771       0  u=1    imp:p=1  $ Copper plate 3 (rho= 8.6771 g/cc)
05       7     -8.8857       0  u=1    imp:p=1  $ Copper plate 4 (rho= 8.8857 g/cc)
06       7     -9.1501       0  u=1    imp:p=1  $ Copper plate 5 (rho= 9.1501 g/cc)
07       7     -9.7741       0  u=1    imp:p=1  $ Copper plate 6 (rho= 9.7741 g/cc)
08       7     -10.5525      0  u=1    imp:p=1  $ Copper plate 7 (rho=10.5525 g/cc)
09       2     -2.6989       0  u=1    imp:p=1  $ Detector front face
10       4     -5.8000       0  u=1    imp:p=1  $ CZT crystal
11       3     -1.0840       0  u=1    imp:p=1  $ Source stand
12       5     -1.2990       0  u=1    imp:p=1  $ Source epoxy well
13       6     -1.1900       0  u=1    imp:p=1  $ Source plastic shell
14       2     -2.6989       0  u=1    imp:p=1  $ Aluminum Base Plate
15       2     -2.6989       0  u=1    imp:p=1  $ Crossbeam
16       2     -2.6989       0  u=1    imp:p=1  $ Upright 1
17       2     -2.6989       0  u=1    imp:p=1  $ Upright 2
18       3     -1.0840       0  u=1    imp:p=1  $ Detector Saddle
19       1     -0.001205     0  u=1    imp:p=1  $ Inferred Background
c
c LEGACY CELLS
20       0          -99  fill=1 imp:p=1  $ Mesh universe fill cell
21       0           99         imp:p=0  $ FATALITY

c
c SURFACES
99  sph   1.27000E+02   6.17499E+01   6.28650E+01   2.87630E+02

c
c  DATA CARDS
mode p
nps 1e7
sdef erg=0.662 pos=volumer   $ volumetric Cs-137 source
c
embed1 meshgeo=abaqus
       mgeoin=plate_assembly_TET.inp
       meeout=plate_assembly_TET.eeout
       length= 1.00000E-01
       background=      19
       matcell=  1  1  2  2  3  3  4  4  5  5  6  6  7  7  8  8  9  9 10 10
                11 11 12 12 13 13 14 14 15 15 16 16 17 17 18 18
c
c  MATERIAL CARDS
```

```
c Air (density = 0.001205 g/cc)
m1     6000  -0.000124
       7000  -0.755268
       8000  -0.231781
      18000  -0.012827
c Aluminum (density = 2.6989 g/cc)
m2    13000  -1.000000
c Nylon 6 (density = 1.084 g/cc)
m3     1000  11.0
       6000   6.0
           7000   1.0
           8000   1.0
c CZT detector crystal (density = 5.8 g/cc)
m4    30000   0.05
      48000   0.45
      52000   0.50
c Epoxy Well in Source (density = 1.299 g/cc)
m5     1000   0.576
       6000   0.288
           8000   0.036
          17000   0.050
          55000   0.050
c Cast Acrylic Button Source (density = 1.19 g/cc)
m6     1000   8.0
       6000   5.0
           8000   2.0
c 110 Copper (original density = 8.93 g/cc)
m7     8000   0.0004
      29000   0.9996
c
c  TALLY CARDS
f8:p 10         $ pulse height tally in CZT detector
e8 0 0.661 0.663
```

# Appendix H. Deformed Plate Homogeneous HEX MCNP Input Deck

```
cubit(arter/Research/Files for MCNP Runs/plate_assembly_hex.inp): 01/19/2022: 11
c
c  Created from file    : plate_assembly_hex.inp
c  Created on           :  1-19-2022 @ 11:32:21
c
c
c PSEUDO CELLS
01       2     -2.6989       0  u=1    imp:p=1  $ Detector casing
02       7     -9.1400       0  u=1    imp:p=1  $ Copper plate 1
03       7     -9.1400       0  u=1    imp:p=1  $ Copper plate 2
04       7     -9.1400       0  u=1    imp:p=1  $ Copper plate 3
05       7     -9.1400       0  u=1    imp:p=1  $ Copper plate 4
06       7     -9.1400       0  u=1    imp:p=1  $ Copper plate 5
07       7     -9.1400       0  u=1    imp:p=1  $ Copper plate 6
08       7     -9.1400       0  u=1    imp:p=1  $ Copper plate 7
09       2     -2.6989       0  u=1    imp:p=1  $ Detector front face
10       4     -5.8000       0  u=1    imp:p=1  $ CZT crystal
11       3     -1.0840       0  u=1    imp:p=1  $ Source stand
12       5     -1.2990       0  u=1    imp:p=1  $ Source epoxy well
13       6     -1.1900       0  u=1    imp:p=1  $ Source plastic shell
14       2     -2.6989       0  u=1    imp:p=1  $ Aluminum Base Plate
15       2     -2.6989       0  u=1    imp:p=1  $ Crossbeam
16       2     -2.6989       0  u=1    imp:p=1  $ Upright 1
17       2     -2.6989       0  u=1    imp:p=1  $ Upright 2
18       3     -1.0840       0  u=1    imp:p=1  $ Detector Saddle
20       1     -0.001205     0  u=1    imp:p=1  $ Inferred Background
c
c LEGACY CELLS
21       0          -99  fill=1 imp:p=1  $ Mesh universe fill cell
22       0           99         imp:p=0  $ FATALITY

c
c SURFACES
99  sph   1.27000E+02   6.17499E+01   6.28650E+01   2.87630E+02

c
c  DATA CARDS
mode p
nps 1e8
sdef erg=0.662 pos=volumer   $ volumetric Cs-137 source
c
embed1 meshgeo=abaqus
       mgeoin=plate_hex_1.inp
       length= 1.00000E-01
       background=      20
       matcell=  1  1  2  2  3  3  4  4  5  5  6  6  7  7  8  8  9  9 10 10
                11 11 12 12 13 13 14 14 15 15 16 16 17 17 18 18
c
c  MATERIAL CARDS
c Air (density = 0.001205 g/cc)
```

```
m1     6000 -0.000124
       7000 -0.755268
       8000 -0.231781
      18000 -0.012827
c Aluminum (density = 2.6989 g/cc)
m2    13000 -1.000000
c Nylon 6 (density = 1.084 g/cc)
m3     1000 11.0
       6000  6.0
           7000  1.0
           8000  1.0
c CZT detector crystal (density = 5.8 g/cc)
m4    30000  0.05
      48000  0.45
      52000  0.50
c Epoxy Well in Source (density = 1.299 g/cc)
m5     1000  0.576
       6000  0.288
           8000  0.036
          17000  0.050
          55000  0.050
c Cast Acrylic Button Source (density = 1.19 g/cc)
m6     1000  8.0
       6000  5.0
           8000  2.0
c 110 Copper (original density = 8.93 g/cc)
m7     8000  0.0004
      29000  0.9996
c
c  TALLY CARDS
f8:p 9 10         $ pulse height tally in CZT detector
e8 0 0.661 0.663
```

# Appendix I. Deformed Plate Variable Density HEX MCNP Input Deck

```
cubit(arter/Research/Files for MCNP Runs/plate_assembly_hex.inp): 01/19/2022: 11
c
c  Created from file    : plate_assembly_hex.inp
c  Created on           :  1-19-2022 @ 11:32:21
c
c
c PSEUDO CELLS
01       2     -2.6989       0  u=1    imp:p=1  $ Detector casing
02       7     -7.8511       0  u=1    imp:p=1  $ Copper plate 1 (rho= 7.8511 g/cc)
03       7     -7.9900       0  u=1    imp:p=1  $ Copper plate 2 (rho= 7.9900 g/cc)
04       7     -8.6771       0  u=1    imp:p=1  $ Copper plate 3 (rho= 8.6771 g/cc)
05       7     -8.8857       0  u=1    imp:p=1  $ Copper plate 4 (rho= 8.8857 g/cc)
06       7     -9.1501       0  u=1    imp:p=1  $ Copper plate 5 (rho= 9.1501 g/cc)
07       7     -9.7741       0  u=1    imp:p=1  $ Copper plate 6 (rho= 9.7741 g/cc)
08       7     -10.5525      0  u=1    imp:p=1  $ Copper plate 7 (rho=10.5525 g/cc)
09       2     -2.6989       0  u=1    imp:p=1  $ Detector front face
10       4     -5.8000       0  u=1    imp:p=1  $ CZT crystal
11       3     -1.0840       0  u=1    imp:p=1  $ Source stand
12       5     -1.2990       0  u=1    imp:p=1  $ Source epoxy well
13       6     -1.1900       0  u=1    imp:p=1  $ Source plastic shell
14       2     -2.6989       0  u=1    imp:p=1  $ Aluminum Base Plate
15       2     -2.6989       0  u=1    imp:p=1  $ Crossbeam
16       2     -2.6989       0  u=1    imp:p=1  $ Upright 1
17       2     -2.6989       0  u=1    imp:p=1  $ Upright 2
18       3     -1.0840       0  u=1    imp:p=1  $ Detector Saddle
20       1     -0.001205     0  u=1    imp:p=1  $ Inferred Background
c
c LEGACY CELLS
21       0          -99  fill=1 imp:p=1  $ Mesh universe fill cell
22       0           99         imp:p=0  $ FATALITY

c
c SURFACES
99  sph   1.27000E+02   6.17499E+01   6.28650E+01   2.87630E+02

c
c  DATA CARDS
mode p
nps 1e8
sdef erg=0.662 pos=volumer   $ volumetric Cs-137 source
c
embed1 meshgeo=abaqus
       mgeoin=plate_hex_1.inp
       length= 1.00000E-01
       background=      20
       matcell=  1  1  2  2  3  3  4  4  5  5  6  6  7  7  8  8  9  9 10 10
                11 11 12 12 13 13 14 14 15 15 16 16 17 17 18 18
c
c  MATERIAL CARDS
c Air (density = 0.001205 g/cc)
```

```
m1     6000 -0.000124
       7000 -0.755268
       8000 -0.231781
      18000 -0.012827
c Aluminum (density = 2.6989 g/cc)
m2    13000 -1.000000
c Nylon 6 (density = 1.084 g/cc)
m3     1000 11.0
       6000  6.0
           7000  1.0
           8000  1.0
c CZT detector crystal (density = 5.8 g/cc)
m4    30000  0.05
      48000  0.45
      52000  0.50
c Epoxy Well in Source (density = 1.299 g/cc)
m5     1000  0.576
       6000  0.288
           8000  0.036
          17000  0.050
          55000  0.050
c Cast Acrylic Button Source (density = 1.19 g/cc)
m6     1000  8.0
       6000  5.0
           8000  2.0
c 110 Copper (original density = 8.93 g/cc)
m7     8000  0.0004
      29000  0.9996
c
c  TALLY CARDS
f8:p 9 10         $ pulse height tally in CZT detector
e8 0 0.661 0.663
```

# Bibliography


1. C.J. Werner, et al., "MCNP6.2 Release Notes", Los Alamos National Laboratory, report LA-UR-18-20808 (2018).

2. T. Goorley, et al., "Initial MCNP6 Release Overview - MCNP6 version 1.0", Los Alamos National Laboratory, report LA-UR-13-22934 (2013).

3. H. Pham. *Software Reliability*. John Wiley & Sons, Inc, 1999.

4. S. Mangul et al. Systematic benchmarking of omics computational tools. *Nature Communications*, 10(1), 2019.

5. D. Beyer, S. Löwe, and P. Wendler. Reliable benchmarking: requirements and solutions. *International Journal on Software Tools for Technology Transfer*, 21(1):1–29, 2017.

6. C. Allison, "Meshing in FEA: Structured vs Unstructured meshes", OnScale, 2021. [Online]. Available: https://onscale.com/blog/meshing-in-fea-structured-vs-unstructured-meshes. [Accessed: 19-Jan-2021].

7. R. L. Martz, "The MCNP6 Book On Unstructured Mesh Geometry: User's Guide for MCNP 6.2," Los Alamos National Laboratory, report LA-UR-17-22442 (2017).

8. Cubit Development Team. *CUBIT Mesh Generation Environment Volume 1: Users Manual*.

9. Dassault Systèmes Simulia, Inc. Providence, RI, USA. 2020. Abaqus CAE 2020. [Online] Available: https://www.3ds.com/products-services/simulia/products/abaqus/abaquscae/.

10. Sandia National Laboratory. Albuquerque, NM, USA. 2021. CUBIT, ver. 15.6. [Online] Available: https://cubit.sandia.gov/.

11. J. Armstrong et al., "MCNP Unstructured Mesh Overview, Improvement, and Verification & Validation Testing," 2021 MCNP User Symposium, Virtual, July 12-16, 2021, Los Alamos National Laboratory (2021).

12. R. D. Mosteller, "Validation Suites for MCNP," Proceedings of the American Nuclear Society Radiation Protection and Shielding Division 12th Biennial Topical Meeting, Santa Fe, New Mexico, Los Alamos National Laboratory, report LA-UR-02-0878 (2002).

13. R. L. Martz and J. A. Kulesza, "Verification and Validation of Unstructured Mesh Tracking in the MCNP Code Version 6.2," Los Alamos National Laboratory, report LA-UR-17-22660 (2017).

14. D. B. Pelowitz, A. J. Fallgren, and G. E. McMath, "MCNP6 User's Manual: Code Version 6.1.1 Beta," Los Alamos National Laboratory, report LA-CP-14-00745 (2014).

15. J. Armstrong, private communication, 2021.

16. R.L. Martz and K.M. Marshall, "A Notable Comparison of Computational Geometries in MCNP6 Calculations", Los Alamos National Laboratory, report LA-UR-12-24621 (2012).

17. R. L. Martz, "MCNP6 Unstructured Mesh Capability," Los Alamos National Laboratory, report LA-UR-11-02767 (2011).

18. J. B. Spencer and J. L. Alwin, "Big Ten MCNP6 Unstructured Mesh Benchmark," Los Alamos National Laboratory, report LA-UR-19-25731 (2019).

19. Silver Fir Software, "Attila4MC", 2021. [Online]. Available: https://silverfirsoftware.com/products/attila4mc/. [Accessed: 11-Jun-2021].

20. J. B. Spencer and J. L. Alwin, "Critical Experiment Benchmark Results using UM and Mesh Quality Recommendations," Los Alamos National Laboratory, report LA-UR-19-26393 (2019).

21. J. A. Kulesza and R. L. Martz, "Evaluation of Pulsed Sphere Time-of-Flight and Neutron Attenuation Experimental Benchmarks Using MCNP6's Unstructured Mesh Capability," Los Alamos National Laboratory, report LA-UR-15-27014 (2015).

22. H. Leiendecker, A. Warhover, J. Armstrong, and J. Ferguson, "MCNP Unstructured Mesh Code Verification for OKTAVIAN Benchmark," 2021 ANS Virtual Annual Meeting, Los Alamos National Laboratory (2021).

23. J. A. Kulesza and R. L. Martz, "Evaluation of the Kobayashi Analytical Benchmark Using MCNP6's Unstructured Mesh Capability," Los Alamos National Laboratory, report LA-UR-15-270893 (2015).

24. K. Zieb et al., "Preliminary Investigation of MCNP6 Unstructured Mesh Geometry For Radiation Flux Calculations Involving Space Environment," Joint International Conference on Mathematics and Computation (M&C), Supercomputing in Nuclear Applications (SNA) and the Monte Carlo (MC) Method, Nashville TN, 2015, ANS.

25. J. Eichenlaub, "Investigation of Electron Energy Deposition Edit Accuracy for Mesh Geometries," 2021 MCNP User Symposium, Virtual, July 12-16, 2021, Los Alamos National Laboratory (2021).

26. C. A. Anderson, K. C. Kelley, J. T. Goorley, "Mesh Human Phantoms with MCNP", Simulia Customer Conference, Providence RI, May 15-17, Los Alamos National Laboratory, report LA-UR-12-00139 (2012).

27. H. Lin et al., "Development of a whole-body tetrahedral mesh human phantom for radiation dose calculations using new MCNP 6.1 geometrical features," Joint International Conference on Mathematics and Computation (M&C), Supercomputing in Nuclear Applications (SNA) and the Monte Carlo (MC) Method, Nashville TN, 2015, ANS.

28. R. Pampin et al. Estimation of radiation conditions in the ITER electron cyclotron upper launcher with state-of-the-art simulation techniques. *Fusion Engineering and Design*, 157, 2020.

29. "Altair Hypermesh: High-fidelity Finite Element Modeling", 2021. [Online]. Available: https://www.altair.com/hypermesh/. [Accessed: 17-Feb-2021].

30. Yican Wu, Jing Song, Huaqing Zheng, Guangyao Sun, Lijuan Hao, Pengcheng Long, and Liqin Hu. CAD-based Monte Carlo program for integrated simulation of nuclear system SuperMC. *SNA MC 2013 - Joint International Conference on Supercomputing in Nuclear Applications Monte Carlo*, 2014.

31. H. Chohan, M. Fabbri, R. Pampin, A. Portone, G. D'Amico, and Á. Cubí. Application of MCNP unstructured mesh in the design process of the ITER EC-UL M3 mirror. *Fusion Engineering and Design*, 166, 2021.

32. D. Holland, private communication, 2021.

33. G. Faraji, H. S. Kim, and H. T. Kashi. *Severe Plastic Deformation: Methods, Processing, and Properties*. Elsevier, 2018.

34. W. Riley, L. Sturges, and D. Morris. *Mechanics of Materials*. John Wiley & Sons, Inc., 6th edition, 2007.

35. S. S. Bhavikatti. *Finite Element Analysis*. New Age International (P), Ltd., 2005.

36. E. Barbero. *Finite Element Analysis of Composite Materials Using Abaqus*. CRC Press, 2013.

37. Dassault Systèmes Simulia, Inc., "ABAQUS USER MANUALS, Version 6.9," Providence, RI (2009).

38. N. Quartemont, J. Bevins, R. Slaybough, and L. Bernstein. Analysis of an energy tuning assembly for simulating nuclear weapon environments at the national ignition facility. *Journal of Radiation Effects*, 38, 2020.

39. N. Quartemont et al. ATHENA: A unique radiation environment platform at the National Ignition Facility. *Nuclear Instruments and Methods in Physics Research Section A: Accelerators, Spectrometers, Detectors and Associated Equipment*, 1016:165777, 2021.

40. L. Greenwood and C. Johnson, "User Guide for the STAYSL PNNL Suite of Software Tools," Pacific Northwest National Laboratory, report PNNL-22253 (2013).

41. N. Quartemont, private communication, 2021.

42. M. Hollander, D. Wolfe, and E. Chicken. *Nonparametric Statistical Methods*. John Wiley and Sons Ltd, 3rd edition, 2014.

43. Lawrence Livermore National Laboratory. Livermore, CA, USA. 2021. VisIT. [Online] Available: https://wci.llnl.gov/simulation/computer-codes/visit.

44. "Alro Metals Smart Grid", 2021. [Online]. Available: https://www.myalro.com/SmartGrid.aspx?PT=Steel&Clear=true. [Accessed: 27-Nov-2021].

45. "MatWeb: Material Property Data," 2021. [Online]. Available: https://http://www.matweb.com/index.aspx. [Accessed: 27-Nov-2021].

46. NIST Physical Measurement Laboratory, "X-Ray Mass Attenuation Coefficients," 2021. [Online]. Available: https://www.nist.gov/pml/x-ray-mass-attenuation-coefficients. [Accessed: 27-Nov-2021].

47. N. Tsoulfanidis and S. Landsberger. *Measurement and Detection of Radiation*. CRC Press, 4th edition, 2015.

48. Alfred Buch. *Pure Metals Properties: A Scientific-Technical Handbook*. Freund Publishing House, 1999.

49. R.J. McConn Jr. et al, "Compendium of Material Composition Data for Radiation Transport Modeling", Pacific Northwest National Laboratory, report PNNL-15870 Rev. 1 (2011).

50. E. Brown, private communication, 2022.

51. M. Jeroutek and D. Holland, "Enhanced Notepad++ text editing tools for MCNP input decks," 2021 MCNP User Symposium, Virtual, July 12-16, 2021, Los Alamos National Laboratory (2021).

# Acronyms

**AFIT** Air Force Institute of Technology. 23, 28, 29, 38, 39, 41, 47, 54

**CSG** constructive solid geometry. iv, x, xi, xii, xiii, 1, 2, 3, 5, 6, 7, 8, 9, 11, 12, 13, 14, 15, 16, 17, 18, 19, 20, 21, 22, 27, 29, 32, 33, 34, 55, 56, 57, 65, 66, 70, 71, 72, 73, 74, 75, 76, 77, 78, 79, 80, 81, 82, 83, 84, 1

**CZT** cadmium zinc telluride. 41, 63

**D-T** deuterium-tritium. 14, 29, 30

**ECUL** Electron Cyclotron Upper Launcher. 21

**EEOUT** Elemental Edit Output. 7, 8, 18

**ETA** Energy Tuning Assembly. 29, 30

**FDM** finite difference method. 25

**FEA** finite element analysis. 1, 5, 23, 25, 26, 34, 51, 63

**FEM** finite element method. 23, 25

**HEX** hexahedral. 4, 12, 16, 51, 53, 58, 59, 60, 61, 65, 67

**HPC** high performance computing. 29, 54, 65

**IMT** Immediate Mode Tracking. 9, 10, 11

**ITER** International Thermonuclear Experimental Reactor. 20, 21, 22

**K-S test** Kolmogorov-Smirnov Test. 33, 55, 56, 57, 58

**LACEF** Los Alamos Critical Experiment Facility. 12

**LANL** Los Alamos National Laboratory. 1, 10, 19, 20, 66

**LAT** Look-Ahead Tracking. 9, 10, 11

**LLNL** Lawrence Livermore National Laboratory. 14

**MCNP** Monte Carlo N-Particle Transport Code. iv, v, x, xiv, 1, 2, 3, 4, 5, 6, 7, 8, 9, 10, 11, 12, 14, 15, 16, 17, 18, 19, 20, 21, 22, 23, 26, 27, 28, 29, 32, 34, 36, 37, 43, 44, 45, 53, 54, 58, 59, 62, 63, 64, 65, 66, 67, 1

**MTS** Material Test System. 47, 48

**NIF** National Ignition Facility. 29, 30, 32, 65

**ODB** output database file. 26, 34

**PENT** pentahedral. 4

**PNNL** Pacific Northwest National Laboratory. 31, 53

**REGL** Revised Extended Grid Library. 9, 10, 11

**RPI** Rensselaer Polytechnic Institute. 18, 20

**SS 316** stainless steel 316. 38, 39

**TET** tetrahedral. 4, 10, 12, 14, 16, 18, 20, 21, 32, 51, 53, 58, 59, 60, 61, 65, 67

**TLD** thermoluminescent dosimeter. 30, 31, 33, 66

**UM** unstructured mesh. iv, v, xiv, 1, 2, 3, 4, 5, 6, 7, 8, 9, 10, 11, 12, 13, 14, 15, 16, 17, 18, 19, 20, 21, 22, 23, 27, 28, 29, 32, 33, 34, 35, 36, 37, 43, 44, 50, 53, 56, 58, 59, 60, 61, 63, 64, 65, 66, 67, 1

# REPORT DOCUMENTATION PAGE

*Form Approved*
*OMB No. 0704–0188*



| 1. REPORT DATE *(DD–MM–YYYY)* | 2. REPORT TYPE | 3. DATES COVERED *(From — To)* |
|---|---|---|
| 24–03–2022 | Master's Thesis | Sept 2020 — Mar 2022 |

**4. TITLE AND SUBTITLE**

Verification and Validation of Unstructured Meshing Capabilities in MCNP6

**5a. CONTRACT NUMBER**

**5b. GRANT NUMBER**

89233119SNA000103

**5c. PROGRAM ELEMENT NUMBER**

**6. AUTHOR(S)**

Micah C. Jeroutek

**5d. PROJECT NUMBER**

22ENP223

**5e. TASK NUMBER**

**5f. WORK UNIT NUMBER**

**7. PERFORMING ORGANIZATION NAME(S) AND ADDRESS(ES)**

Air Force Institute of Technology
Graduate School of Engineering and Management (AFIT/EN)
2950 Hobson Way
WPAFB OH 45433-7765

**8. PERFORMING ORGANIZATION REPORT NUMBER**

AFIT-ENP-MS-22-M-097

**9. SPONSORING / MONITORING AGENCY NAME(S) AND ADDRESS(ES)**

NNSA
1000 Independence Ave, S.W.
Washington D.C., 20585
Email: susan.norwood@nnsa.gov

**10. SPONSOR/MONITOR'S ACRONYM(S)**

NNSA

**11. SPONSOR/MONITOR'S REPORT NUMBER(S)**

**12. DISTRIBUTION / AVAILABILITY STATEMENT**

DISTRIBUTION STATEMENT A:
APPROVED FOR PUBLIC RELEASE; DISTRIBUTION UNLIMITED.

**13. SUPPLEMENTARY NOTES**

**14. ABSTRACT**

Discrepancies were found between the legacy CSGs and the new UMs with the latter's introduction in MCNP6. As such, V&V of UMs in MCNP must be conducted to assist in their further development and increase user confidence in them. Currently, the MCNP test suite is lacking in UM benchmarks, and of the few that are present, their range in problem type is limited. To address these issues, two preliminary test cases covering new applications of UMs were developed for future inclusion in the test suite. The first was for the Athena-I experiment which involved the study of electronic devices' responses to nuclear threat representative neutron environments, and the second involved modeling photon shielding capabilities for a deformed copper plate. Both had complex geometries to highlight the strengths of UM models which yielded results in agreement with their respective CSG counterparts and experimental data.

**15. SUBJECT TERMS**

Verification, Validation, Benchmarks, Monte Carlo Methods, MCNP, Radiation Transport, Unstructured Mesh

| 16. SECURITY CLASSIFICATION OF: | | | 17. LIMITATION OF ABSTRACT | 18. NUMBER OF PAGES | 19a. NAME OF RESPONSIBLE PERSON |
|---|---|---|---|---|---|
| a. REPORT | b. ABSTRACT | c. THIS PAGE | | | Dr. Darren E. Holland, AFIT/ENP |
| U | U | U | UU | 159 | 19b. TELEPHONE NUMBER *(include area code)* (937) 255-3636, ext 4697; darren.holland@afit.edu |